Dark Matter and Neutron Stars

by

Narayani Tyagi

A thesis submitted to the
Department of Physics, Engineering Physics, & Astronomy
in conformity with the requirements for
the degree of Doctor of Philosophy

Queen's University
Kingston, Ontario, Canada
September 2025

Abstract

Neutron stars and fast radio bursts (FRBs) serve as powerful, complementary probes of dark matter models that lie beyond the reach of laboratory experiments. This thesis investigates neutron stars and their role in dark matter search strategies.

In the first part, the thesis demonstrates a new method to look for inelastic dark matter. We show that inelastic dark matter captured by neutron stars can remain in long-lived orbits and annihilate outside the stellar volume. By modeling this exterior annihilation process in the Galactic center, we derive γ-ray and ν flux predictions that translate into limits on the inelastic dark matter-nucleon cross section of $\sigma_{\chi n} \lesssim 3\times10^{-46}$ cm^2 for dark matter masses ranging between $m_\chi \sim 10^2 - 10^5$ GeV, with next-generation observatories expected to improve sensitivity by an order of magnitude.

Shifting focus from the Galactic Center to our own backyard, we refine the solar neighborhood's free electron density map by combining pulsar parallax measurements with Gaussian process interpolation. This empirically calibrated $n_e(r)$ sharpens dispersion-measure-based neutron star distance estimates and identifies the most promising nearby neutron star targets for infrared searches of dark matter induced heating signatures.

Finally, we expand our approach to cosmological transients. It has been appreciated for some time that asymmetric dark matter can cause neutron stars to implode

and form black holes. These implosions have been linked to fast radio bursts. For the first time, this thesis obtains predictions for fast radio burst dispersion measure distributions arising from neutron star implosions triggered by accumulated asymmetric dark matter cores or primordial black hole capture in spiral, elliptical and dwarf galaxy hosts.

Together, these investigations show that through high-energy annihilation signals, thermal heating, and fast radio burst signatures of dark matter induced collapse, neutron stars serve as a useful means for determining or bounding dark matter's interactions.

Acknowledgments

Above all, I am endlessly grateful to my advisor and mentor, Joseph Bramante, for his steadfast guidance, invaluable feedback, and continuous support throughout this journey. I would also like to thank Aaron Vincent, Guillaume Giroux, Felicia Magpantay, and Violetta Sagun for their time and thoughtful engagement with this work as my defense committee. I owe my deepest gratitude to the members of the QHEAT cohort whose insightful discussions and thoughtful suggestions profoundly shaped my doctoral journey, with a special thanks to Yilda Boukhtouchen, J. Leo Kim, Qinrui Liu, and Chris Cappiello, whose expertise and good humor transformed our brainstorming sessions into productive and joyful collaborations.

I'm truly indebted to my family and friends, whose unwavering support sustained me - my mother, Lata, who always encouraged me with her inquisitiveness; my sister, Vasundhra, who provided wisdom and much-needed comic relief; my husband, Deepak, my rock, without whom none of this would have been possible; and my cat, Blutooth, who kept me company during countless late nights and early mornings of writing. Finally, I dedicate this work to my father, Manoj, whose presence, even in his absence, has been a guiding light. His memory inspired me to cross the finish line. Dad, this one's for you.

Statement of Originality

The contents of this thesis, including all writing, research design, analysis, and results, were undertaken by Narayani Tyagi, with the exception of Chapters 3 and 4, which are reproductions of manuscripts written in collaboration with coauthors.

Chapter 3 is a reproduction of "Neutrino and gamma-ray signatures of inelastic dark matter annihilating outside neutron stars" written with Javier Acevedo, Joseph Bramante, and Qinrui Liu, published in the Journal of Cosmology and Astroparticle Physics. Narayani Tyagi conducted primary analysis and writing for the sections on galactic center modeling, inelastic dark matter thermalization, and models for inelastic dark matter. Results for neutrino telescopes and gamma-ray observatories were led by coauthor Qinrui Liu. All authors participated in the overall writing, design, and revisions of the manuscript.

Chapter 4 is a reproduction of "Seeking the nearest neutron stars using a new local electron density map" written with Joseph Bramante, Katherine Mack, Nirmal Raj, and Lijing Shao, submitted for publication to the Journal of Cosmology and Astroparticle Physics. All analysis and writing were primarily undertaken by Narayani Tyagi, with additional research design, writing, and revisions provided by the above-listed coauthors.

Contents

List of Tables

List of Figures

Chapter 1

Introduction

Our Universe is permeated by an elusive form of matter that neither emits nor absorbs light [1], yet its gravitational imprint is unmistakable. However, despite decades of intensive research, the nature of this *dark* matter remains one of the most significant unresolved mysteries in modern physics and astronomy. Comprising approximately 85% of the Universe's total matter density, dark matter does not interact electromagnetically and thus evades direct observation through traditional astronomical means [1, 2]. Nevertheless, its existence is strongly inferred through its gravitational effects across a wide range of astrophysical scales, ranging from the rotation curves of spiral galaxies to large-scale structure formation and the anisotropies observed in the cosmic microwave background [3]. Efforts to detect dark matter through terrestrial experiments have pushed sensitivities to remarkable new frontiers. However, such detectors remain inherently limited to certain classes of dark matter candidates, specifically those with cross-sections and masses conducive to measurable nuclear recoil signatures [4]. Notably elusive are candidates such as inelastic dark matter, particularly heavy dark matter species, and primordial black holes (PBHs), each of which can evade conventional direct detection methods. Hence, complementary strategies

are essential to probe these elusive yet theoretically compelling dark matter scenarios.

Compact astrophysical objects, most notably neutron stars, present unique and powerful environments to address this challenge. Neutron stars, with their astonishingly high densities, intense gravitational fields, and potential for long-term integration of signals, offer an ideal, natural laboratory to investigate otherwise undetectable dark matter interactions. By examining the observational consequences of dark matter capture, annihilation, and potential collapse within and around neutron stars, we endeavour to open pathways to novel detection strategies that leverage multiple different astrophysical phenomena and multimessenger astrophysics-encompassing, but not limited to electromagnetic radiation, neutrinos, and gravitational waves [5–8].

This thesis is structured around investigating these possibilities, systematically exploring theoretical frameworks, phenomenological signatures, and astrophysical observables associated with dark matter-neutron star interactions. We specifically focus on how neutron stars can illuminate the nature of inelastic dark matter annihilation processes, how local neutron star searches can benefit from refined astrophysical modeling, and how fast radio bursts (FRBs) could potentially arise from dark matter-induced neutron star implosions.

1.1 Thesis Roadmap

This thesis explores the theoretical, phenomenological, and astrophysical aspects of searches for dark matter using neutron stars (NSs) and their interactions with various models of dark matter. Chapter 1 introduces the overarching themes and objectives of the thesis. Chapter 2 provides essential background material, reviewing observational evidence for dark matter, various particle-physics candidates, standard dark

matter halo density profiles, and fundamentals of compact object physics relevant to dark matter detection. It also discusses electron density models used for the Milky Way and introduces key concepts in FRB phenomenology. Chapter 3 investigates neutrino and gamma-ray signals arising from inelastic dark matter annihilation inside and, notably, outside neutron stars. Here we present analytical and numerical predictions, introducing a novel scenario where captured dark matter particles annihilate significantly outside the neutron star due to a prolonged thermalization phase; the majority of this work was originally published in Ref. [9]. In Chapter 4, we address the observational prospects for detecting dark matter induced heating of nearby neutron stars. Given that such heating might yield detectable infrared signatures with next-generation telescopes (*e.g.* ELT, TMT), we focus on improving our local electron-density modeling, which is critical for accurately identifying the closest neutron star targets. Using parallax measurements of pulsars and Gaussian-process interpolation, we present an updated kiloparsec-scale electron-density map, originally detailed in Ref. [10], yielding revised neutron-star distance estimates and highlighting key local observational targets. Chapter 5 examines how neutron-star implosions induced by dark matter accumulation would manifest in the dispersion measures of extragalactic FRBs, a scenario first proposed in Refs. [11–13]. We model and predict the galactocentric distributions and dispersion measure characteristics of FRBs arising in three representative extragalactic host galaxy environments: spiral, elliptical, and dwarf galaxies. We contrast scenarios in which FRBs trace standard neutron star populations against those resulting from asymmetric dark matter-induced or primordial black hole-induced neutron star collapses. Finally, Chapter 6 summarizes the key findings presented throughout this thesis, emphasizing our results on external inelastic

dark matter annihilation around neutron stars, refined electron-density mapping for local neutron-star searches, and distinctive FRB signatures from dark matter-induced neutron-star implosions. The chapter concludes by outlining promising avenues for future work, including extending explicit dark matter model constraints and modeling gravitational-wave emission from dark core collapse.

1.2 Notation, Conventions and Disclaimers

Unless, otherwise mentioned, we adopt natural units ($\hbar = c = k_B = 1$) and a ΛCDM cosmology with $H_0 = 70$km/s/Mpc, $\Omega_m = 0.3$, $\Omega_\Lambda = 0.7$.

Disclaimer - Throughout this thesis, the abbreviation DM refers *only* to dispersion measure.

Chapter 2

Background

This chapter reviews the key theoretical and observational foundations necessary for understanding the analyses in subsequent chapters. We begin with an overview of dark matter phenomenology and galactic dark matter halo structures, then turn to the role of compact astrophysical objects as laboratories for dark matter interactions, and specifically detail inelastic dark matter models and their interactions, since this particular class of models will be important to understand for Chapter 3 of the thesis.

2.1 Basic Evidence for Dark Matter

The first compelling indication of unseen mass came from Fritz Zwicky's 1933 study of the Coma cluster, where galaxy velocity dispersions exceeded those expected from the luminous mass by nearly an order of magnitude [3, 14]. Few decades later, in the 1970s, Vera Rubin and collaborators mapped the rotation curve of M31 and found that the orbital speed of stars remained approximately constant well beyond the optical disk [1]. These "flat" rotation curves defied the Keplerian decline predicted if only visible matter were present, implying a dominant, extended mass component-a dark matter halo-surrounding spiral galaxies.

Gravitational lensing provides a second, independent probe. In the Bullet Cluster, a high-velocity collision of two galaxy clusters, X-ray–emitting gas (the baryons) is spatially separated from the total mass distribution inferred from weak lensing [15]. The lensing peaks, which trace collisionless matter, do not coincide with the hot gas, demonstrating that most of the cluster's mass is in a non-interacting form.

On cosmological scales, measurements of the cosmic microwave background (CMB) anisotropies by WMAP [16] and Planck [2] determine the total matter density $\Omega_m \approx 0.31$ and the baryon density $\Omega_b \approx 0.049$, leaving a non-baryonic component $\Omega_{\rm nb} \approx 0.26$. These measurements come from analyzing the heights and positions of the acoustic peaks in the CMB power spectrum, which depend sensitively on the amounts of baryons and dark matter at recombination, providing percent-level constraints on their abundances.

Big Bang nucleosynthesis (BBN) offers a complementary test: the primordial abundances of deuterium, helium and lithium, inferred from astrophysical observations, agree with theoretical predictions only if the baryon-to-photon ratio corresponds to $\Omega_b \ll \Omega_m$ [17]. Together, these pieces of evidence point towards a large fraction of matter in the early universe being non-baryonic matter.

2.2 Dark Matter Models

Dark-matter candidate models span an extraordinary mass range - allowing for over eighty orders of magnitude in the allowed fundamental unit of dark matter mass - from the mass of a star at the heavy end to about 10^{-30} times the mass of the proton at the ultra-light sector. Despite this large plausible mass range, particle physics has lately focused on the freeze-out dark matter window, which spans roughly from

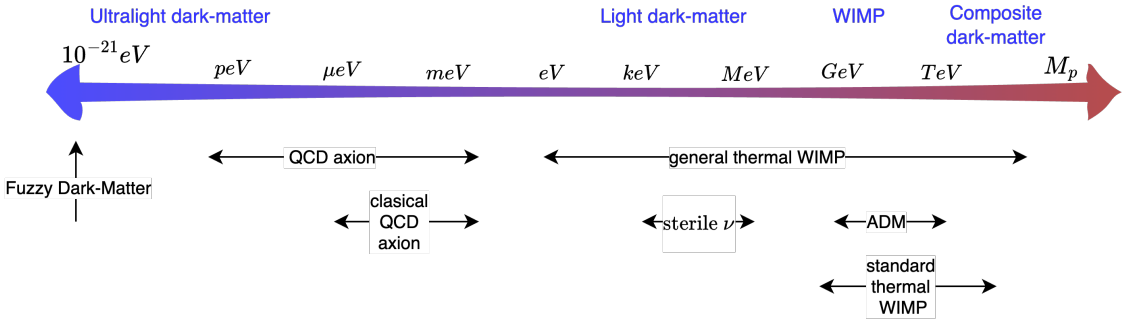

Figure 2.1: Schematic illustration of the vast range of possible dark matter particle masses, from ultralight ($\sim 10^{-20}$ eV) to very heavy (multi-TeV or beyond). The color bar indicates the transition from non-thermal (very light, *e.g.* bosonic field dark matter) to hot/warm (keV-scale) to cold dark matter (GeV–TeV scale) as the mass increases [18]

sub-GeV to multi-TeV masses [18].

However, the full range of dark matter possibilities spans a much larger set of possibilities. At the low end of the plausible mass range are the ultra-light axions (*e.g.* the QCD axion, $m_a \sim 10^{-6}$–10^{-4} eV) or more general axion-like particles (ALPs) whose masses and couplings are largely unconstrained. Moving up in mass, sterile neutrinos with keV-scale masses occupy the warm-dark matter regime, while sub-GeV to few-GeV particles (*e.g.* light WIMPs or dark-sector fermions) and canonical Weakly Interacting Massive Particles (WIMPs, $m_\chi \sim 1$–10^3 GeV) provide well-studied cold-relic scenarios. By unitarity arguments, thermal relics cannot exceed $\mathcal{O}(100)$ TeV without violating partial-wave unitarity [19, 20]. Finally, primordial black holes (PBHs) with masses $M \sim 10^{15}$–10^{23} g (10^{-18}–$10^{-10}\, M_\odot$) represent a macroscopic, purely gravitational dark matter candidate formed non-thermally in the early Universe [21]. Generally, only particles heavier than a few keV act as cold dark matter, since lighter species free-stream and erase small-scale structure. Below, we summarize some of the leading scenarios:

2.2.1 Weakly Interacting Massive Particles (WIMPs)

Thermal relic WIMPs arise naturally in models with electroweak-scale couplings and masses of order 10–10^3 GeV. In the early universe, WIMPs (χ) remain in chemical equilibrium via $\chi+\chi \leftrightarrow$ SM+SM until the expansion rate H exceeds their annihilation rate $\langle\sigma v\rangle n_\chi$, "freezing out" a relic abundance $\Omega_\chi h^2 \simeq 0.1\,(\langle\sigma v\rangle/3\times10^{-26}\,\mathrm{cm^3/s})^{-1}$ [18, 22]. Direct-detection experiments target nuclear recoils from $\chi N \to \chi N$, pushing cross-section limits below $10^{-46}\,\mathrm{cm}^2$ for $m_\chi \sim 100\,\mathrm{GeV}$, though parameter space remains for lighter WIMPs and non-standard interactions. [23]

2.2.2 Axions and Axion-Like Particles(ALPs)

Originally proposed to solve the strong CP problem, the QCD axion is a pseudo-Nambu–Goldstone boson with masses $m_a \sim 10^{-6}$–$10^{-3}\,\mathrm{eV}$ and very weak photon coupling $g_{a\gamma} \sim 10^{-16}$–$10^{-13}\,\mathrm{GeV}^{-1}$ [24]. Unlike thermal relics, axions are produced through non-thermal mechanisms such as vacuum misalignment and the decay of topological defects, naturally yielding a cold dark matter population without requiring freeze-out processes [25]. Haloscope and helioscope experiments (ADMX, CAST) [26, 27] probe $g_{a\gamma}$ down to QCD-axion predictions, while stellar cooling observations exclude larger couplings across much of the remaining parameter space.

2.2.3 Primordial Black Holes

Black holes formed in the early universe (PBHs) can span masses $10^{-16} - 10^3\,M_\odot$ and, if sufficiently abundant, constitute some or all of the dark matter [21, 28]. Microlensing surveys (EROS,OGLE) [29] and dynamical constraints (wide binaries, CMB anisotropies) exclude large mass windows, but sub-lunar masses ($10^{-13} - 10^{-10}\,M_\odot$)

remain viable. PBHs also serve as dark matter probes: their surrounding dark matter spikes can enhance annihilation signals in indirect searches [30]. We discuss such PBH interactions with compact objects in Section 2.6.3 below.

2.2.4 Asymmetric Dark Matter

Models relating the dark-matter asymmetry to the baryon asymmetry predict dark matter masses $m_\chi \sim$ few GeV and feeble annihilation at late times [31, 32]. The relic abundance is set by a primordial particle–antiparticle asymmetry, evading indirect-detection constraints. Asymmetric dark matter can accumulate in compact objects without annihilating, potentially forming black-hole cores inside neutron stars [33–35]. We will study the phenomenology of such models in Chapter 5 of this thesis.

2.2.5 Self-Interacting Dark Matter

It is well known that there is a kind of dark matter that can affect small-scale cosmic structure (galactic cores vs. cusps), known as self-interacting dark matter (SIDM) with cross sections $\sigma/m \sim 0.1$–$10\,\mathrm{cm}^2/\mathrm{g}$. Models and signatures of SIDM have been proposed in [15, 36–39], including models with mediators of mass $\sim 1\,\mathrm{MeV}$ that yield velocity-dependent interactions that are strong in dwarf galaxies but weaker in galactic clusters. SIDM affects halo shapes and substructure, and can modify capture and thermalization in neutron stars.

2.2.6 Composite Dark Matter

It has long been appreciated that dark matter may be a composite state that is much larger in size or occupancy number than bound states like nuclei or atoms in the

Standard Model [4, 40–54]. Prior work has largely considered composites with either a small number of constituents or "saturated" composites-large-N bound states whose binding energy E_B is comparable to the constituent mass m_d, yielding a mass-per-constituent $\overline{m}_d \ll m_d$ and high internal densities [47, 53–55].

More recently, loosely-bound composite dark matter models-where $E_B \ll m_d$ and nuclear scattering of the composite can produce many low-energy nuclear recoils have been proposed and explored in [56].

2.3 Dark Matter Interactions and Detection

The experimental search for dark matter is fundamentally dictated by particle interaction strengths. This is why there has often been an emphasis on dark matter models whose interactions required for cosmogenesis imply detectability at ongoing or planned particle experiments. For so-called thermal-relic WIMPs, the observed relic density $\Omega_\chi h^2 \simeq 0.12$ implies a freeze-out annihilation cross section, commonly referred to as the *canonical* WIMP cross section, usually stated as

$$\langle \sigma_{FO} \rangle \approx 3 \times 10^{-26} \mathrm{cm}^3 \mathrm{s}^{-1}. \tag{2.1}$$

This is a well-established result derived from the Boltzmann equation for thermal freeze-out [22]. Underground direct-detection experiments like XENON, LZ, and PandaX, have pushed the limits on spin-independent WIMP–nucleon scattering down to $\sigma_{\chi N} \lesssim 2.6 \times 10^{-47}\,\mathrm{cm}^2$ at $m_\chi \sim 30\,\mathrm{GeV}$ [23, 57–59], which rules out several WIMP and WIMP-like dark matter candidates, while still leaving some WIMP candidates unexplored [60, 61]. Below a few GeV, kinematic thresholds weaken these bounds, but novel low-threshold techniques such as SENSEI, SuperCDMS, and Migdal-effect

searches extend sensitivity into the sub-GeV range, probing $\sigma_{\chi N} \sim 10^{-39}$–$10^{-41}\,\mathrm{cm}^2$ for $m_\chi \sim 0.5$–1 GeV [62, 63].

Axionic candidates exhibit significantly weaker couplings, necessitating alternative detection strategies. The QCD axion–photon coupling $g_{a\gamma\gamma} \sim 10^{-16}$–$10^{-12}\,\mathrm{GeV}^{-1}$ is probed by resonant haloscopes (ADMX) and helioscopes (CAST, IAXO) in the μeV mass window [26]. Liquid Xenon detectors further constrain solar axions and ALPs via electron couplings $g_{ae} \lesssim 2 \times 10^{-12}$ for $m_a \lesssim 1\,\mathrm{eV}$, leveraging axion-electron interactions in target materials [64].

Primordial black holes (PBHs), if they constitute dark matter, interact purely via gravity; and can thus be sought solely through gravitational effects [65]. Key constraints on PBH dark matter come from gravitational lensing surveys, cosmic microwave background (CMB) observations, and dynamical effects. For example, dedicated microlensing surveys (OGLE, EROS, MACHO, etc.) have searched for lensing events caused by compact objects in the Milky Way halo. These surveys have ruled out PBHs making up all of the dark matter over a wide range of masses (from roughly $10^{-10} M_\odot$ up to $> 10 M_\odot$), because such PBHs would have produced detectable microlensing of background stars and that was not observed at the expected rate [29, 66]. Very light PBHs (below 10^{15} g) would have evaporated via Hawking radiation by today, and intermediate-mass PBHs (10^{15}–10^{17} g) are constrained by extragalactic γ-ray backgrounds from any Hawking evaporation. The asteroid-mass window (10^{20}–10^{22} g) remains viable for significant dark matter fractions but faces tightening bounds from pulsar timing arrays and X-ray monitoring for lensing [67].

Together, these mass scales and cross-section targets necessitate a rich phenomenological program - from underground WIMP detectors to astrophysical and gravitational probes - each searching for different subsets of dark matter's potential properties.

2.4 Inelastic Dark Matter

In this thesis, so-called inelastic dark matter will be important for Chapter 3, and so we will provide an extended discussion of its properties. In its original incarnation [68], inelastic dark matter models involve interactions where the primary dark matter particle χ_1 scatters off Standard Model particles by transitioning to a heavier state χ_2 with mass splitting $\delta = m_{\chi_2} - m_{\chi_1}$ [69–71]. This process requires a minimum initial kinetic energy $E_{\rm kin} \geq \delta$ to occur. This energy threshold leads to two universal kinematic consequences that are largely model independent.

1. As only dark matter particles with sufficiently high velocities in the Galactic halo can overcome the mass splitting δ, this reduces the kinematically accessible phase space for scattering, suppressing the expected event rate in detectors compared to elastic dark matter.

2. Moreover, the energy threshold imposes a minimum nuclear recoil energy $E_{\rm R}^{\rm min}$ that must be deposited in the detector. This creates challenges for traditional direct detection experiments that have optimized sensitivity to elastic dark matter-nuclei collisions by focusing on the limit $E_{\rm R}^{\rm min} \to 0$, and pushing the observed recoil energy window as low as backgrounds and detector sensitivities allow. This poses a problem for inelastic dark matter with a sizable mass splitting, as a low maximum recoil energy reduces the detector's sensitivity.

This means that at best, a lower maximum recoil energy will be sub-optimal for detecting inelastic dark matter, and at worst, if the dark matter's minimum inelastic recoil energy lies above the window of recoil energies that the detector is sensitive to, the experiment will be insensitive to inelastic dark matter.

Experiment	Window	Inelastic Reach
LUX	1–30 keV	insensitive to $\delta \geq 180\,\text{keV}$
PICO	$E_R \leq 1\,\text{MeV}$	strongest for 160–300 keV
CRESST	1–40 keV	sensitive up to $\delta \sim 350\,\text{keV}$

Table 2.1: Current experimental sensitivities for inelastic dark matter detection. Key implications here are that kinematic thresholds, rather than detector technology, set the inelastic dark matter reach [70].

2.4.1 Inelastic Kinematics

To set the stage for inelastic dark matter searches, we review the kinematics of a transition $\chi_1 + N \to \chi_2 + N$ with mass splitting $\delta \equiv m_{\chi_2} - m_{\chi_1} > 0$ [72–75]. In the non-relativistic limit, an incoming dark matter particle of speed v (in the lab frame) has kinetic energy

$$E_0 \;=\; \tfrac{1}{2}\, m_{\chi_1} v^2 \;, \tag{2.2}$$

and the nuclear recoil energy E_R satisfies [70]

$$E_R \;=\; \frac{\mu}{m_N}\Big[(\mu v^2 \cos^2\theta_{\text{lab}} - \delta) \pm \sqrt{\mu v^2 \cos^2\theta_{\text{lab}}}\,\sqrt{\mu v^2 \cos^2\theta_{\text{lab}} - 2\delta}\Big] \;, \tag{2.3}$$

where μ is the reduced mass and θ_{lab} is the scattering angle. Unlike elastic scattering, this relation imposes both lower and upper bounds on E_R.

Crucially, if the dark matter speed falls below the threshold $v_{min} \simeq \sqrt{2\delta/\mu}$, no real

solutions exist and scattering is entirely forbidden, sharply truncating the accessible phase space in direct-detection experiments. Moreover, as the mass splitting δ increases, the required minimum velocity likewise grows, excluding an ever larger fraction of the galactic dark matter from contributing any recoil signal and producing pronounced cutoffs in the observed recoil spectrum. For a comprehensive derivation and discussion of these bounds in the context of direct detection at high recoil energies, see the detailed treatment in Ref. [70].

There are several well-motivated models that can contain inelastic splittings of a reasonable size for current and future direct detection searches: supersymmetric neutralinos, magnetic inelastic dark matter, and dark photon mediated dark model. However, in the rest of this section, we present the workings of the dark photon mediated dark matter model in detail as this builds the foundation for future chapters.

2.4.2 Dark Photon Mediated Inelastic Dark Matter

In models where dark matter interacts via a dark photon, the splitting between the two dark matter states arises due to the spontaneous symmetry breaking of the $U(1)_D$ gauge symmetry by the scalar boson that couples to the dark matter.

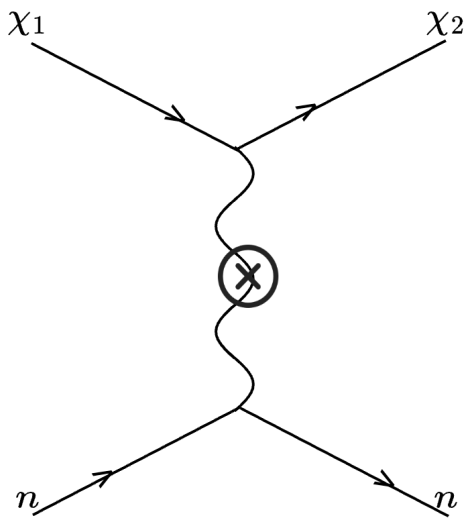

Figure 2.2: Inelastic dark matter interaction mediated by a dark photon

The Lagrangian $\mathcal{L}$ [70] describes the full interaction as

$$\begin{aligned}\mathcal{L} = \mathcal{L}_{SM} + |D_\mu \phi|^2 + V(\phi) - \frac{1}{4} V_{\mu\nu}^2 + \epsilon V_\mu \partial_\nu F^{\mu\nu} \\ + \bar{\chi}\left(i D_\mu \gamma_\mu - m_\chi\right)\chi + \left(\lambda_D \phi \chi^T C^{-1} \chi + h.c.\right).\end{aligned} \tag{2.4}$$

Here, V_μ denotes the gauge boson of the dark $U(1)_D$ symmetry, which mixes kinetically with the Standard Model photon $F_{\mu\nu}$ through the parameter ϵ (typically $\epsilon \lesssim 10^{-4} - 10^{-2}$). The covariant derivative $D_\mu = \partial_\mu + i e_D V_\mu$ encodes the coupling of the dark matter fermion χ to the dark photon, while the Yukawa term (the last term in the Eq. 2.4) generates a Majorana mass splitting for χ once the dark scalar ϕ acquires its vacuum expectation value.

The resulting mass eigenstates $\chi_{1,2}$ therefore differ by $\delta m \sim \lambda_D \langle \phi \rangle$, giving rise to

inelastic scattering processes in which the lighter χ_1 *upscatters* into χ_2 when interacting with ordinary matter, thus intimately tying the kinematic threshold δm to the symmetry breaking scale in the dark sector.

2.4.3 Dark Photon Mediated Relic-Density

In the limit where Standard Model particles and the dark photon are much lighter than the dark matter ($m_V \ll m_{\chi_1}$), annihilation of non-relativistic χ_1 into dark photons proceeds with

$$\langle \sigma_{\rm ann} v \rangle \simeq \frac{\pi \, \alpha_D^2}{2 \, m_{\chi_1}^2} \, .$$

Demanding that this freeze-out yields the observed relic abundance $\Omega_\chi h^2 \simeq 0.12$ fixes the dark-sector coupling to [22]

$$\alpha_D \approx 3.7 \times 10^{-2} \left(\frac{m_{\chi_1}}{\rm TeV} \right).$$

2.4.4 Dark Photon Mediated Scattering

In these models, elastic and inelastic nuclear scatterings proceed via exchange of the dark photon V, which mixes with the Standard Model photon and Z boson after $\mathrm{U}(1)_D$ and electroweak symmetry breaking. In the regime where the momentum transfer $q^2 \ll m_V^2$, the spin-independent cross section on a nucleus of charge Z is given by [70]

$$\sigma_{N\chi}^D = \frac{16\pi \, \alpha_{\rm em} \, \alpha_D \, \epsilon^2 \, \mu_N^2}{m_V^4} \, Z^2 \, , \tag{2.5}$$

where $\alpha_{\rm em}$ is the electromagnetic gauge coupling constant, ϵ is the kinetic-mixing parameter, μ_N is the dark-matter–nucleus reduced mass, and $m_V \approx \sqrt{4\pi\alpha_D}\, v_\Phi$ is the dark photon mass. This expression underlies our capture rate and direct-detection

projections in Chapter 3. For dark photons heavier than the momentum exchange, the *loop-induced* elastic cross-section depends on the mass of the dark photon. loop-induced elastic scattering of dark photon-mediated dark matter can be approximated as [70],

$$\sigma^{\rm D}_{\rm n,loop} \sim \frac{\alpha_{\rm D}^2 \alpha_{\rm em}^2 \epsilon^4 m_n^4 f_q^2}{\pi m_V^6},$$

where we take the hadronic matrix elements $f_q \sim 0.1$.

2.5 Halo Density Profiles

Dark-matter halos on very different scales are commonly modeled by spherically symmetric density profiles that transition from a high-density inner region to a steep outer decline. Popular examples include the Navarro–Frenk–White profile [76], which features a cuspy inner slope born from cold-dark-matter simulations, and the Burkert profile [77], which instead exhibits a constant-density core more consistent with observations of dwarf and low-surface-brightness galaxies. We shall briefly summarize these for the cases of some different galaxies: dwarfs, spirals, and ellipticals.

The *Burkert profile* [77] for cored halos is

$$\rho_{\rm B}(r) = \frac{\rho_0}{\left(1 + r/r_0\right)\left(1 + (r/r_0)^2\right)}, \tag{2.6}$$

where r_0 is the size of the central core and ρ_0 is the central density. To model low-mass dwarf galaxies, we follow Ref. [78], and adopt two representative Leo T fits denoted D2 and D3, each characterized by a core radius r_0 and an enclosed mass within 300 pc M_{300}, where

$$M(r_{\rm enc}) = 4\pi \int_0^{r_{\rm enc}} r^2 \rho_{\rm B}(r)\, dr \tag{2.7}$$

at $r_{\rm enc} = 300\,\mathrm{pc}$ fixes ρ_0. Then the resulting parameters are

Model	r_0 (pc)	ρ_0 ($M_\odot\,\mathrm{pc}^{-3}$)	$M_{300}(10^6\,M_\odot)$
D2	400	7.1×10^6	8.0
D3	142	2.9×10^7	15.5

Table 2.2: Burkert-profile parameters for the cored Leo T models D2 and D3 from Ref. [78]. Here r_0 is the core radius, ρ_0 the central density, and M_{300} the enclosed dark-matter mass within 300 pc.

The *Navarro–Frenk–White (NFW) profile* [76] for cuspy halos is,

$$\rho_{\rm NFW}(r) \;=\; \frac{\rho_s}{(r/r_s)\,(1+r/r_s)^2}\,, \tag{2.8}$$

parameterized by the scale density ρ_s and scale radius r_s. For a Milky Way equivalent spiral type galaxy, we follow Sofue's [79] fit for the Milky Way's surface mass density, which is a combination of an exponential stellar disk and an NFW halo. Their best-fit halo parameters that we adopt are

$$r_s = 10.94 \pm 1.05\ \mathrm{kpc},\ \rho_s = 0.787 \pm 0.037\ \mathrm{GeV/cm}^3,\ \rho_\odot = 0.359 \pm 0.017\ \mathrm{GeV/cm}^3.$$

Here $\rho_\odot$ is the local dark-matter density at the Sun's location.

For a generic elliptical halo, we instead take $M_{\rm vir} = 3.8\times10^{12}\,h_{70}^{-1}M_\odot$ and concentration $c = 9.5$ [79], which implies $r_{\rm vir} \approx 206\,h_{70}^{-1}$ kpc and $r_s = r_{\rm vir}/c$. The profile in physical units is

$$\rho_{\rm NFW}(r) = \frac{M_{\rm vir}}{4\pi\, r_s^3\, g(c)}\,\frac{1}{(r/r_s)\,(1+r/r_s)^2}, \quad g(c) = \ln(1+c) - \frac{c}{1+c}.$$

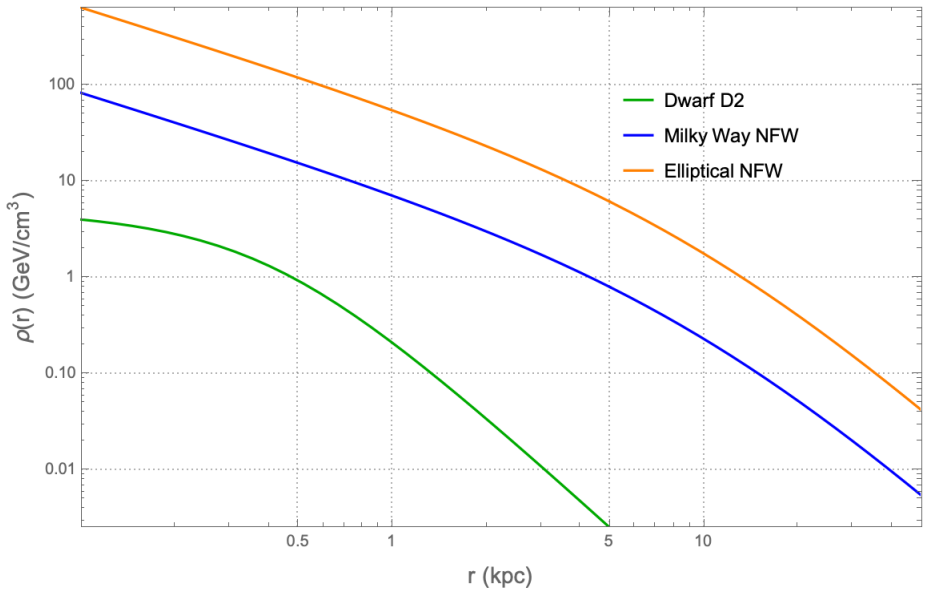

Figure 2.3: Comparison of three dark matter halos in GeV/cm^3 vs. radius in kpc: Burkert "D2" for Dwarf(green), Milky Way NFW (blue; $r_s = 10.94\,\mathrm{kpc}$, $\rho_s = 0.787\,\mathrm{GeV/cm^3}$), and an "elliptical" NFW (orange; $M_{\rm vir} = 3.8 \times 10^{12}\,h_{70}^{-1}\,M_\odot$, $c = 9.5$).

2.6 Compact Object Physics

Neutron stars (NSs), white dwarfs (WDs), and primordial black holes (PBHs) offer some advantages in dark matter searches: chiefly, their utility lies in accelerating dark matter to relativistic or near-relativistic velocities, and in the case of white dwarfs and neutron stars, providing a very dense medium for dark matter to interact with.

2.6.1 Neutron Stars

Neutron stars (NSs) are the densest stable stellar remnants, with typical masses $M_{\rm NS} \approx 1.4\,M_\odot$ and radii $R_{\rm NS} \sim 10 - 12$ km. Their high surface escape velocity

$$v_{\rm esc} \;=\; \sqrt{\frac{2G\,M_{\rm NS}}{R_{\rm NS}}} \;\approx\; 0.6\,c\,,$$

means that for a broad range of dark matter masses, dark matter particles which scatter even once off a nucleon can become gravitationally bound [80–82].

As isolated NSs age ($\gtrsim 10^6$ yr), their core temperatures cool to $T_c \sim 10^5 - 10^6$ K, providing a cold background against which any dark matter-induced heating stands out [83].

Dark Matter Capture in NSs A fraction of the dark matter particles that transit a neutron star lose energy through scattering. For different mass regimes, this might mean a single scatter resulting in dark matter capture, or multiple scatters for dark matter capture. In the rest frame of the NS a dark matter-nucleon scattering event depletes the dark matter kinetic energy by [82]:

$$\Delta E_s = \frac{m_n m_\chi^2 \gamma^2 v_{esc}^2}{m_n^2 + m_\chi^2 + 2\gamma m_\chi m_n} \left(1 - cos\, \theta_c\right). \tag{2.9}$$

The maximum capture rate obtained by assuming that all dark matter that passes through the effective area of the NS is captured (sometimes also referred to as the geometric capture rate) is given by

$$\begin{aligned} \dot{m}_\chi &= \pi b_{\max}^2 \rho_\chi v_\chi \,, \\ b_{\max} &= \left(\frac{2GMR}{v_\chi^2}\right)^{1/2} \left(1 - \frac{2GM}{R}\right)^{-1/2} \end{aligned} \tag{2.10}$$

where v_χ is the dark matter velocity in the halo, ρ_χ is the dark matter density, M is the mass of the neutron star, and γ is implicitly defined as the relativistic gamma factor of the infalling dark matter relative to an external observer.

The above equation accounts for a single compact object (NS in this case) capturing the dark matter. However, a better observational probability lies in the strength of many. Then, the total dark matter capture rate by a population of NSs can be given as

$$\mathcal{C}_{NS_{Total}} = 4\pi \int_{r_1}^{r_2} r^2 \eta_{NS} \mathcal{C}_{NS(max)}\, dr, \tag{2.11}$$

where r is the radial distance from the galactic center, η_{NS} is the NS number density, and $\mathcal{C}_{NS}$ is the capture rate by a single NS.

If the dark matter happens to be symmetric, the evolution of the number of bound dark matter particles N_X is given by

$$\frac{dN_X}{dt} = C_X - \frac{\langle \sigma v \rangle N_X^2}{V}\ , \tag{2.12}$$

where C_X is the capture rate, $\langle \sigma v \rangle$ is the annihilation cross-section, and V is the volume where annihilation occurs. After capture, dark matter thermalizes in the core on short timescales and may annihilate or collapse, leading to potential observable signatures such as excess surface heating or even catastrophic implosion.

Neutron Star Distribution Neutron stars predominantly form in the core collapse of massive stars ($M \gtrsim 8M_\odot$)–the progenitors of type Ib, Ic and II supernovae– and, more rarely, via the accretion-induced collapse of white dwarfs that have reached the Chandrasekhar mass (type Ia supernovae). Adopting a present-day core-collapse rate in the Milky Way of $\beta_{\rm NS} \sim \mathcal{O}$(few/century) [84], and assuming this rate has been roughly constant over the Galaxy's ~ 10 Gyr lifetime, implies $N_{\rm NS} \sim 10^8$–10^9 neutron stars produced to date. Such numbers mean neutron stars represent a non-negligible fraction of the Galactic stellar population.

To model the present-day distribution of Galactic neutron stars (NSs), we follow the Monte Carlo study of Sartore et al. [85], who considered five progenitor–velocity combinations (models 1A–1E). The evolved NS surface density in the disk is well described by a fourth-order polynomial fit in Galactocentric radius R:

$$\log_{10}\Sigma(R) \;=\; a_0 + a_1 R + a_2 R^2 + a_3 R^3 + a_4 R^4\,, \tag{2.13}$$

where the coefficients a_i for each model are listed in Table A.1 of [85]. Figure 2.4 compares $\Sigma(R)$ for models 1A–1E, illustrating the range of disk concentrations. These were obtained from dynamical simulations of neutron stars born with a variety of initial kick velocities, where different kick velocity models correspond to models 1A–1E.

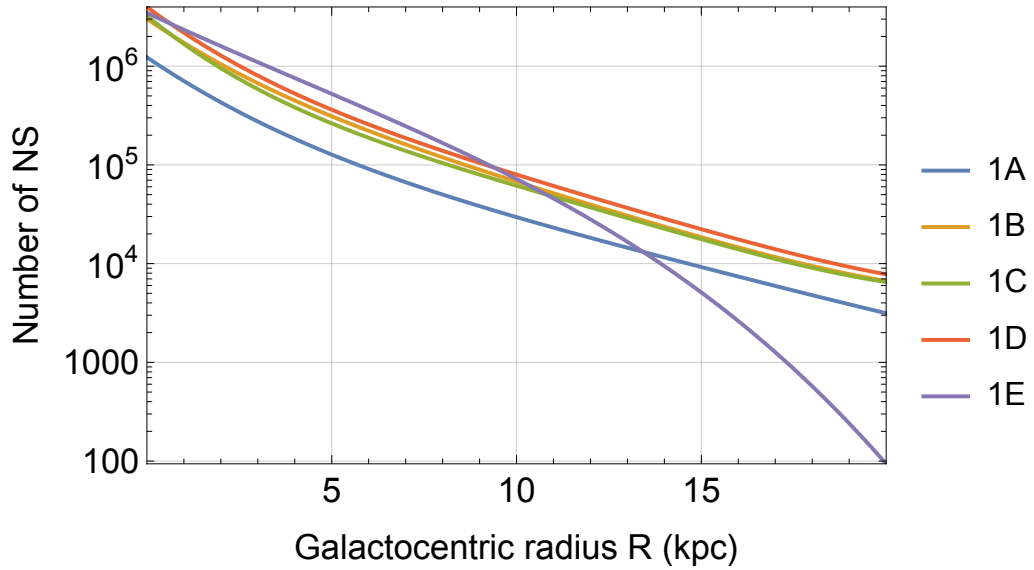

Figure 2.4: NS distribution expressed as radial surface number density $\Sigma(R)$(Eq.(2.13)).All relevant coefficients are given in Table A.1 of Ref. [85]

In the plane of the Milky Way galaxy (the x-y plane), Sartore et al. [85] modeled the present-day vertical distribution of neutron stars as a function of height z from

this plane using a logistic-type fit

$$f(z) \;=\; \frac{1}{b_0\, b_1^{|z|} \;+\; b_2}\,, \tag{2.14}$$

where the parameters b_0, b_1, and b_2 (listed in Table A.2 of Ref. [85]) set the midplane normalization, the exponential fall-off per kpc, and any residual floor density. The half-density height $z_{1/2}$ is defined by $f(z_{1/2}) = 1/2$, and the vertical scale height h_z is related by $b_1 = \exp(1/h_z)$. In Figure 2.5 , we display $f(z)$ for models 1A–1E from the Sartore study.

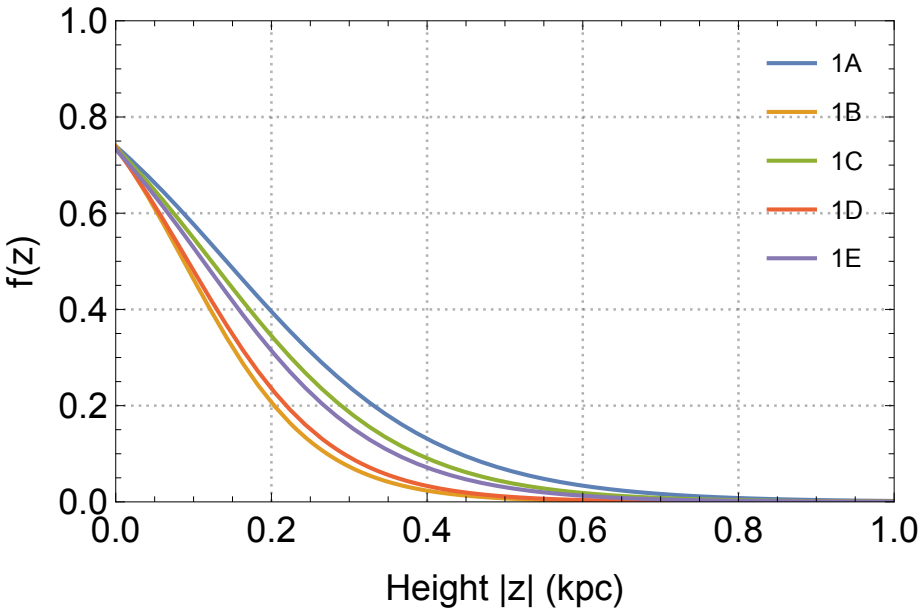

Figure 2.5: Distribution of heights *f(z)*(Eq.(2.14)) for models 1A-1E. All relevant parameters are from Table A.2 of Ref. [85].

Sartore et al. also fit the cumulative velocity distribution of the dynamically simulated NSs using

$$G(v) \;=\; \frac{(v/v_0)^m}{1 + (v/v_0)^n}\,, \tag{2.15}$$

where (v_0, m, n) are shown in Table A.3 of [85]. To show the effect of different assumed kick velocities, in Figure 2.6 we overlay $G(v)$ for models 1A–1E, illustrating how the choice of kick-velocity prescription shapes the high-velocity tail and the distribution of halo-bound NSs.

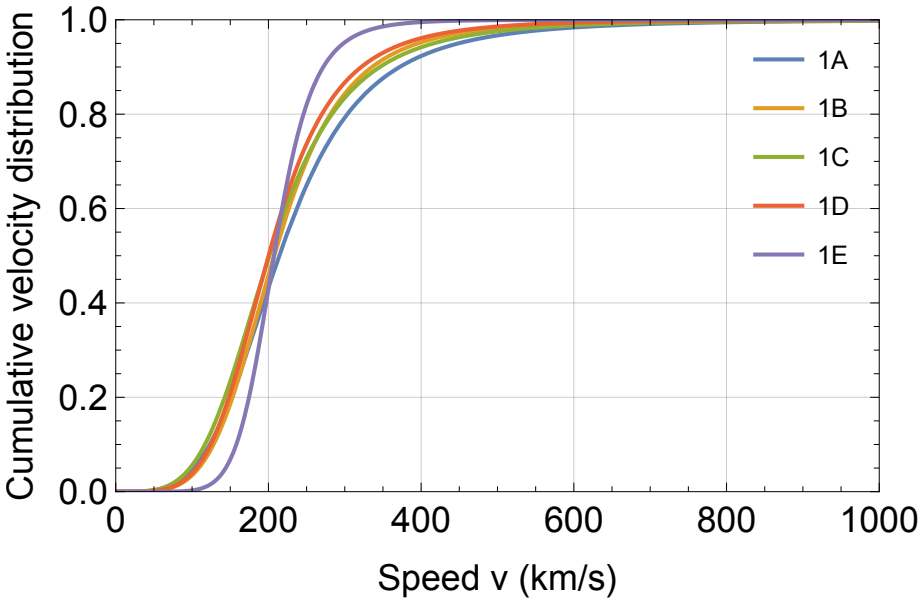

Figure 2.6: Cumulative speed distribution described by Eq.(2.15), showing the fraction of NSs with speeds $\leq v$. The corresponding kick velocity distribution parameters are given in Table A.3 of Ref. [85]).

2.6.2 White Dwarfs

While we won't address white dwarf-dark matter dynamics in this thesis, we nevertheless provide some brief background material here for comparison to the case of neutron stars. White dwarfs (WDs) are electron-degenerate stellar remnants with typical masses $M_{\rm WD} \approx 0.6\, M_\odot$ and radii $R_{\rm WD} \sim 10^4$ km. Their surface escape velocity,

$$v_{\rm esc} \;=\; \sqrt{\frac{2G\, M_{\rm WD}}{R_{\rm WD}}} \;\sim\; 10^{-3}\, c\,, \tag{2.16}$$

while lower than that of NSs, is still sufficient to capture dark matter particles that scatter off nuclei in the WD interior [86].

The capture rate for a WD immersed in a local dark matter density ρ_χ with dark matter velocity dispersion v_χ can be approximated by

$$\dot{m}_\chi \simeq \pi R_{\rm WD}^2 \, \rho_\chi \, \frac{v_{\rm esc}^2}{v_\chi^2} \, \sigma_{\chi N} \, , \tag{2.17}$$

where m_χ is the dark matter mass, and this equation is the same as for the NS max capture rate, but without the necessity of including relativistic correction factors. Over $\sim$ 10 Gyr, even small capture rates can lead to equilibrium between capture and annihilation, potentially producing an observable heating signature against the standard WD cooling sequence, if WDs are ever observed in a sufficiently dense background of dark matter [86].

2.6.3 Primordial Black Holes

Primordial black holes (PBHs) offer a compelling non-particle candidate for dark matter, and their unique interactions with neutron stars motivate several of the searches we develop in later chapters. In the early Universe, overdense regions collapsing under radiation-dominated expansion could have produced PBHs with masses spanning roughly $10^{-16} - 10^5 M_\odot$, entirely uninhibited by stellar evolution [21]. If PBHs make up a fraction $f_{\rm PBH} = \Omega_{\rm PBH}/\Omega_{\rm DM}$ of the cosmological dark matter, then those traversing NSs will experience gravitational capture through dynamical friction, accretion of nuclear matter, or emission of gravitational waves. Once bound, a PBH sinks to

the stellar core on a timescale

$$t_{\rm sink} \sim 10^3 - 10^6 {\rm yr} \left(\frac{M_{\rm PBH}}{10^{-12} M_\odot} \right)^{-1}, \tag{2.18}$$

and grows by Bondi accretion at a rate

$$\dot{M}_{\rm PBH} \propto \frac{M_{\rm PBH}^2 \rho_{\rm NS}}{c_s^3}, \tag{2.19}$$

where $M_{\rm PBH}$ is the PBH mass, $\rho_{\rm NS}$ is the NS central density, and c_s is the speed of sound. Since destruction time scales inversely with the PBH mass, a PBH weighing only a ten-quadrillionth of the Sun, once captured, will consume its host NS in under ten billion years, which is comparable to the ages of the oldest observed pulsars. One of the observational consequence of such destruction is the potential deficit of pulsars (also called the "missing pulsar problem" [11]) in regions of high dark matter density, such as the Galactic Center, although it has been pointed out that the rate for PBHs to convert NSs into black holes would be too low at the center of the Milky Way to account for the missing pulsar problem [33]. Various observational campaigns set complementary limits on the PBH dark matter fraction f_{PBH} across different mass windows, as shown in Table 2.3.

PBH Mass ($M_\odot$)	Upper limit on f_{PBH}	Observational constraint
10^{-16}–10^{-14}	< 0.01–0.1	NS survival in the galactic bulge [87]
10^{-14}–10^{-10}	$< 10^{-5}$–10^{-3}	Fermi-LAT data [88]
10^{-10}–10^{-6}	$\lesssim 0.1$	Presence of old NS in globular clusters [34]

Table 2.3: Constraints on the PBH dark-matter fraction $f_{\rm PBH}$ in key mass ranges from NS survival, Fermi-LAT γ-ray limits, and globular-cluster NS counts.

Here, the most stringent constraints are around $M_{\rm PBH} \sim 10^{-13} M_\odot$ with $f_{\rm PBH} <$

10^{-5}, that arise due to the non-detection of γ-ray flashes that would accompany a PBH consuming its host NS in the pulsar-rich galactic center, as confirmed by the Fermi-LAT data [88]. Moreover, searches for similar signals in globular clusters have likewise yielded null results, further tightening the bounds in this mass window.

2.7 Dispersion measure & electron column density

The fundamental observable that encodes the integrated column of free electrons along the line of sight for a pulsar, as well as an FRB, is its dispersion measure (DM)

$$\mathrm{DM} = \int_0^L n_e(\ell)\, d\ell \ , \tag{2.20}$$

where L is the distance along the line of sight, and n_e is the electron number density [89]. As a result of plasma dispersion, lower frequency components of a radio pulse lag behind higher frequency components by an amount

$$\Delta t \propto \mathrm{DM} \left(\frac{1}{f_1^2} - \frac{1}{f_2^2} \right) \ . \tag{2.21}$$

By measuring these arrival time delays across multiple frequency channels and combining them with independent distance estimates, one can infer the three-dimensional distribution of galactic electrons. This approach is utilized to produce empirical electron density maps for the Milky Way, but since small non-electron contributions($e.g.$ from intervening plasma turbulence) can bias the inferred DM, it has been recently advocated [90] that the astronomers report directly the measured quantity $\mathcal{D} \equiv \Delta t (f_1^{-2} - f_2^{-2})^{-1}$ instead of the model-dependent DM inferred from Eq. (4.2).

Over the past decades, several models have been developed to create and refine

these maps, the most notable of which we will now briefly describe. The NE2001 model [89] represents a major advance over the earlier Taylor-Cordes 1993 (TC93) [91] prescription for the Milky Way's distribution of free electrons.

The basic structure of the NE2001 model consists of three astrophysical components, namely the thick disk, the thin disk, and four logarithmic spiral arms, each characterized by its scale height, scale radii, and midplane density. To this baseline, the model adds a compact galactic center component that accounts for the maximized electron density in the galactic center, a parameterized local interstellar medium that includes the Local Bubble and Loop I, and a population of discrete overdensities and underdensities, or clumps and voids that capture small-scale variations. In practice, NE2001 computes the electron density at any point by evaluating each of these contributions in turn and then summing them with appropriate weighting factors. These weights work to ensure that, for example, the spiral arm densities dominate their longitude ranges, the galactic center term peaks within a few hundred parsecs of the galactic center, and isolated clumps (or voids) locally enhance (or suppress) the free electron density n_e.

The YMW16 electron-density model introduced in 2016 by Yao, Manchester, and Wang [92], extends NE2001's galactic framework by incorporating both the Large and Small Magellanic Clouds and a uniform intergalactic component alongside the standard thick disk, thin disk, and spiral arm structures. In the Milky Way, YMW16 refines the spiral geometry to four principal arms plus a local spur, with each arm's angle, width, and radial extent anchored to observations of over 1800 H-II regions across the galaxy.

To calibrate these components, the authors compiled 189 independent pulsar distance estimates drawn from trigonometric parallaxes, H-I absorption kinematic measurements, and well-established associations with supernova remnants or globular clusters, and optimized the model parameters to minimize the discrepancies between observed and predicted dispersion measures.

Fig. 2.7 compares the free-electron density in the galactic midplane as predicted by the NE2001 and YMW16 models.

YMW16 retains many of the same large and small scale structures found in NE2001, namely the Local Bubble, peripheral enhancements surrounding the Local Bubble, the Gum Nebula, the Carina arm over-density, and the region of reduced electron density in the tangential periphery of Sagittarius, but it forgoes the ad hoc insertion of additional clumps and void that NE2001 uses to force agreement with certain pulsar distance outliers. Likewise, YMW16 omits a global treatment of interstellar scattering, a feature in NE2001 that proved difficult to generalize because scattering is often dominated by just a few localized electron density fluctuations along each line of sight. As a result, YMW16 offers a cleaner, large-scale map at the expense of some of NE2001's finely tuned corrections.

In practical terms, most pulsar distances in the Australian Telescope National Facility (ATNF) catalogue [94] default to YMW16's DM-distance relation, although parallaxes and independent associations with astrophysical objects like supernova remnants or the LMC/SMC remain the gold standard whenever available.

Most importantly, in regions such as the Local Bubble, where the electron density is highly non-uniform, a simple linear DM-distance conversion may break down [95, 96], reinforcing the need for independent distance measurements in these nearby,

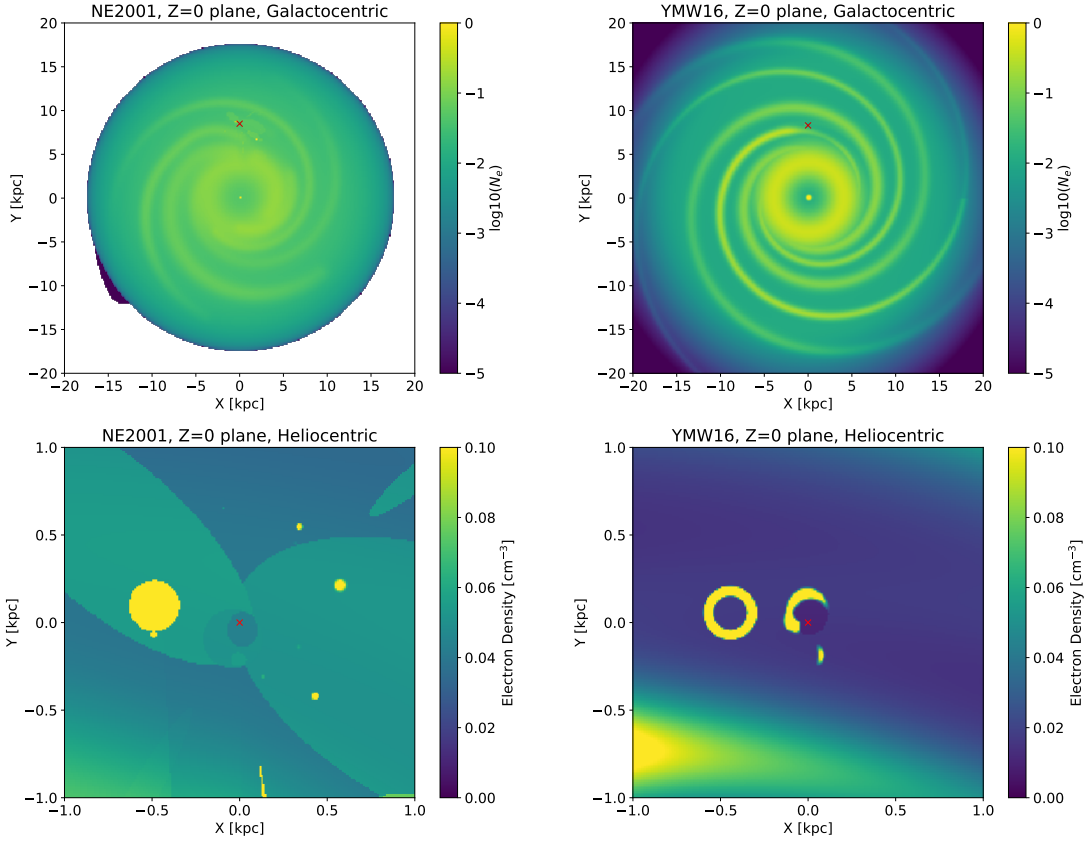

Figure 2.7: Electron density in the Galactic mid-plane ($z = 0$) for the NE2001 model (left panels) and the YMW16 model (right panels). In NE2001, the density is defined out to $|R| \leq 17\,\mathrm{kpc}$, whereas YMW16 extends to $|R| \leq 30\,\mathrm{kpc}$. The Solar position (red cross) is at $(x, y, z) = (0, 8.5, 0)$ kpc in NE2001 and $(0, 8.3, 0.006)$ kpc in YMW16. **Top row:** large-scale structure, where differences in spiral-arm geometry are evident. **Bottom row:** the local interstellar medium in a $\pm 1\,\mathrm{kpc}$ region around the Sun. NE2001 (bottom left) shows "Local Superbubble" and "low-density" cavities plus small circular clumps; YMW16 (bottom right) omits these clumps and instead only retains major features (Gum Nebula, Local Bubble, Loop I, Carina–Sagittarius arm). (Figure from [93]) .

inhomogeneous environments presented later in Chapter 4.

2.8 Fast Radio Burst Phenomenology

First discovered in 2007 [97], fast radio bursts (FRBs) are millisecond-length ∼GHz radio pulses known to occur at "cosmological" distances, with an estimated all-sky rate of $\sim 10^4$/day. Observation at ~ 2 Gpc distances implies large energy and radiated power, extraordinarily high brightness temperature, and coherent emission for these FRBs.

2.8.1 Repetition & Periodicity

Broadly speaking, FRBs can be classified as repeating or non-repeating. More than 60 FRBs have been reported to repeat [98]. Since identifying a repeating FRB simply requires the detection of one additional burst from its source, it is essentially impossible to prove that an FRB source does **not** repeat. However, as has been previously noted [98], repeating FRBs have different spectral characteristics than non-repeating FRBs, suggesting that the one-and-done population of FRBs may come from a different progenitor than the repeating FRBs.

2.8.2 Dispersion Measure and Distance

Radio waves propagating through plasma experience dispersion, with lower frequency waves delayed relative to higher frequency waves. This delay is quantified by the dispersion measure (DM), which represents the integrated column density of free electrons along the line of sight from the source to the observer, measured in units of pc cm^{-3}.

When an FRB is detected, its DM is determined by identifying the dispersion correction that maximizes either the signal-to-noise ratio or resolves the burst's finest

temporal structure [99, 100]. Since FRBs originate from cosmological distances, their DM can generally be expressed as

$$\mathrm{DM} = \int_0^{D_z} \frac{n_e(l)}{1+z(l)}\, dl, \tag{2.22}$$

where $n_e(l)$ is the local electron number density at a comoving distance l along the propagation path, and $z(l)$ is the redshift at that location. The comoving distance from the observer to the source D_z is given by

$$D_z = \frac{c}{H_0} \int_0^z \frac{dz'}{E(z')}, \tag{2.23}$$

where

$$E(z) = \sqrt{\Omega_m (1+z)^3 + \Omega_k (1+z)^2 + \Omega_{\mathrm{DE}} f(z)}, \tag{2.24}$$

$$f(z) = \exp\left[3 \int_0^z \frac{(1+w(z'))dz'}{1+z'}\right], \tag{2.25}$$

Here, H_0 is the Hubble constant, Ω_m, Ω_k and Ω_Λ denote the energy density fraction of matter, curvature, and dark energy, respectively, and $w(z)$ represents the dark energy equation of state parameter. For the standard ΛCDM cosmological model, $\Omega_k = 0$, $\Omega_{\mathrm{DE}} = \Omega_\Lambda$, $w = -1$, and consequently, $f(z) = 1$.

The observed DM of each burst can typically be decomposed into distinct components [101–103]:

$$\mathrm{DM} = \mathrm{DM_{MW}} + \mathrm{DM_{halo}} + \mathrm{DM_{IGM}} + \frac{\mathrm{DM_{host}} + \mathrm{DM_{src}}}{1+z}, \tag{2.26}$$

where $\mathrm{DM_{MW}}$, $\mathrm{DM_{halo}}$, $\mathrm{DM_{IGM}}$, $\mathrm{DM_{host}}$, and $\mathrm{DM_{src}}$ are the contributions from the Milky Way disk, its halo, the intergalactic medium (IGM), the host galaxy, and the

immediate environment of the source, respectively. Note that the observed contributions from the last two components are scaled down by a factor of $(1+z)$, due to cosmological redshift. The Milky Way contribution $\mathrm{DM_{MW}}$ can be obtained using the MW electron density models derived from the radio pulsar data [89, 92], albeit with a $> 50\%$ uncertainty. The extended Milky Way halo contributes to an additional $\mathrm{DM_{halo}} \sim (30-80)$ pc cm^{-3} beyond $\mathrm{DM_{MW}}$ [103]. The IGM component of Eq. 2.26 is a function of redshift as shown by Refs. [104]. The contribution of the IGM to the DMs of FRBs can be calculated using the Macquart relation [103]. At low redshifts ($z \leq 0.6$), we can use the following approximation:

$$\mathrm{DM_{IGM}} \cong 933\,\mathrm{pc\,cm^{-3}}[z + (0.5 - 0.75\Omega_m)z^2]^{-0.5} \times (\frac{f_e}{0.88})(\frac{\Omega_b h^2}{0.022})(\frac{h}{0.7})^{-1} \tag{2.27}$$

where n_0 is the mean number density of nucleons at $z = 0$, f_e is the fraction of baryons in an ionized state, and Ω_m is the matter density in units of the critical density at $z = 0$.

With this theoretical and observational foundation established, we now turn to applying these tools to concrete astrophysical searches in the following chapters.

Chapter 3

Signatures of Inelastic Dark Matter Around Neutron Stars

The detection of dark matter through its effects on compact astrophysical objects has been investigated in many prior works, see Ref. [83] for a review. These have established neutron stars as all-purpose next-generation detectors for any dark matter that interacts with nucleons, since these objects are extremely dense, reach very low temperatures as they age, and accelerate dark matter to semi-relativistic velocities, which altogether offers the possibility of detecting a kinetic heating signature that is robust across a wide range of models [82,105–115]. The usage of neutron stars as dark matter detectors has also drawn an increasing interest over the years in the context of asymmetric dark matter that accumulates inside celestial objects and eventually converts them to black holes [11, 13, 33, 80, 81, 108, 116–130].

A particularly motivated framework is inelastic dark matter, developed to reconcile weak-scale dark matter with direct detection limits. In such models, a Dirac fermion splits into two nearly degenerate Majorana states, χ_1 and χ_2, with a small mass difference δ. The leading interaction is off-diagonal, $\chi_1 N \to \chi_2 N$, requiring

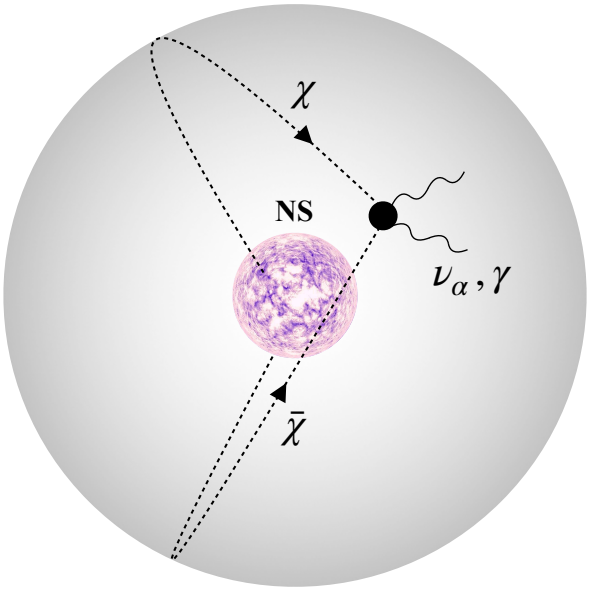

Figure 3.1: Schematic representation of our effect: captured dark matter that scatters through leading-order inelastic interactions is unable to rapidly thermalize with the neutron star if the inelastic transition becomes forbidden, forming a "halo" around the object. If the dark matter density at the neutron star position is sufficiently high, a sizable fraction of these particles will annihilate outside before they fully thermalize through loop-level elastic scatterings. This sources a directly observable γ-ray or neutrino signal.

kinetic energy large enough to excite the heavier state. Halo dark matter on Earth, moving at typical velocities $v \sim 10^{-3}c$, cannot upscatter for $\delta \gtrsim 100$ keV, strongly suppressing elastic scattering in direct detection experiments.

In contrast, neutron stars accelerate infalling dark matter to semi-relativistic velocities $v \sim 0.6c$, enabling upscattering even for mass splittings up to hundreds of MeV. Capture is therefore efficient, but once the inelastic channel closes at lower orbital energies, further cooling is extremely slow since only loop-suppressed elastic scattering remains. This leaves a long-lived population of particles in exterior orbits,

where annihilations can occur outside the star and source observable gamma-ray or neutrino signals.

Neutron stars are thus uniquely sensitive to inelastic dark matter models [82, 131, 132], characterized by endothermic interactions of the form

$$\chi_1 + n \to \chi_2 + n, , \tag{3.1}$$

where n is a nucleon and $\chi_{1,2}$ are dark matter states of different masses. The required threshold energy is set by the splitting δ [68, 70, 74, 133]. With dark matter accelerated by NS gravity, splittings up to $\sim$ 100 MeV are kinematically accessible, far beyond the $\sim$ 100 keV reach of terrestrial direct detection experiments [70]. In this way, neutron stars open discovery space for inelastic dark matter models that remain inaccessible by other means.

In a related but distinct context, it has recently been demonstrated that neutron stars and white dwarfs residing in the Galactic Center can give rise to signals of dark matter annihilating from within, for models with long-lived mediators that escape the object and decay to detectable γ-rays [134, 135]. Due to the high dark matter and stellar density in this region, this "celestial body focused" [134] annihilation is powerful enough to draw constraints on dark matter interactions across a wide mass range, based on existing γ-ray observations. Subsequently, the analysis of Ref. [134] was extended to the case where the mediators decay to high-energy neutrinos [136, 137], and models for displaced dark matter decays in neutron stars have been explored in [137, 138].

In this work, we introduce a new search for dark matter with leading-order inelastic interactions through its annihilation to high-energy photons and neutrinos *outside* neutron stars. After becoming gravitationally bound to the neutron star, dark matter particles will follow closed orbits through the object, progressively losing energy with each neutron star crossing. Thus, the dark matter eventually loses energy to the point that the inelastic transition becomes kinematically forbidden. For mass splittings approximately in the range $45 - 285$ MeV, this will occur while the orbits still extend beyond the neutron star. Provided that elastic interactions are absent or suppressed, and the background dark matter density is high enough, at any given time, there will be an appreciable fraction of dark matter particles annihilating while outside the neutron star volume. We analyze how inelastic dark matter annihilation proceeds in neutron stars in a largely model-independent way, and then provide both constraints and discovery prospects for inelastic dark matter using neutron stars in the Galactic Center as our target. Unlike prior works, this scenario does not require the assumption of long-lived mediators as an intermediate state in the annihilation process. More importantly, this new search may be an alternative to inelastic dark matter searches based on kinetic heating of neutron stars, which at present demand significant observation time with infrared telescopes, are contingent upon the existence of faint radio pulsars close to Earth, and may have substantial background heating sources, which are currently being investigated [139, 140].

The remainder of this chapter proceeds as follows: we begin in Section 3.1 with a discussion of our assumptions concerning the distribution of dark matter and neutron stars in the Galactic Center, our main target for this search, along with the structural properties of a neutron star. In Section 3.2, we briefly review the process of

dark matter capture in neutron stars. The partial thermalization of inelastic dark matter with neutron stars is analyzed in Section 3.3, including an estimate for the timescale of this process, a discussion of the capture-annihilation equilibrium regime, and the estimated fraction of dark matter that annihilates outside of the neutron star. In Section 3.4, we outline current and projected sensitivities for finding heavy inelastic dark matter annihilating to γ-rays and *neutrinos* outside neutron stars in the Galactic Center. Finally, in Section 3.5, we discuss the class of inelastic dark matter models for which this new search is most effective.

3.1 Galactic Center Modeling

To calculate our signal, we require the distribution of both dark matter and neutron stars in the Galactic Center. These inputs determine the overall dark matter annihilation rate proceeding in these objects. Additionally, we also require details about the structure of neutron stars in this region, such as their typical compactness and density profile. These properties ultimately determine the fraction of the total dark matter that will annihilate outside and contribute to the signal.

3.1.1 Dark Matter Density and Velocity

The dark matter halo profiles we consider are the Navarro-Frenk-White (NFW) [76, 141], along with the Einasto [142], and Burkert [77] profiles. These are respectively given by,

$$\rho_{\chi}^{\rm NFW}(R) = \frac{\rho_{\chi}^{0}}{\left(\frac{R}{R_s}\right)^{\gamma}\left(1+\left(\frac{R}{R_s}\right)\right)^{3-\gamma}} \ , \tag{3.2}$$

$$\rho_\chi^{\rm Ein}(R) = \rho_\chi^0 \, \exp\left[-\frac{2}{\alpha}\left(\left(\frac{R}{R_s}\right)^\alpha - 1\right)\right] , \tag{3.3}$$

$$\rho_\chi^{\rm Bur}(R) = \frac{\rho_\chi^0}{\left(1+\frac{R}{R_s}\right)\left[1+\left(\frac{R}{R_s}\right)^2\right]} , \tag{3.4}$$

where R is the Galactocentric distance and ρ_χ^0 is a normalization constant. The parameters were chosen as follows: for the NFW profile, we select a scale radius $R_s = 20$ kpc, and consider two different slopes $\gamma = 1$ and $\gamma = 1.5$ to approximately span the existing uncertainty on this parameter [143, 144]. For the latter slope value, we refer to this as a generalized NFW (gNFW) profile. For the Einasto profile, we fix the scale radius $R_s = 20$ kpc and an exponent $\alpha = 0.17$ [145]. Finally, for the Burkert profile, we choose a scale radius $R_s = 6$ kpc, as suggested by some studies [146]. In all cases, the normalization factor is determined by requiring the distribution to reproduce the observed dark matter density at the Sun's position, $\rho_\chi^\odot \simeq 0.42$ GeV cm^{-3} [147, 148].

The dark matter velocity dispersion towards the Galactic Center is not well understood and, in our region of interest, existing uncertainties span a range $v_d \sim 100 - 900$ km s^{-1} [79]. However, within this range, our computed dark matter capture rate only varies by about a factor ~ 2. As we show below, this quantity determines the signal strength and, since it is rather insensitive to this input, we assume a fixed velocity dispersion of $v_d \simeq 270$ km s^{-1} for simplicity.

3.1.2 Neutron Star Density

We consider three separate neutron star distribution models presented in Refs. [85, 149, 150]. Ref. [149] put forth a semi-analytic treatment of mass segregation effects

around supermassive black holes, and obtained power-law distributions for various stellar object types at the Galactic Center, in the range $10^{-2} - 1$ pc. On the other hand, Ref. [85] conducted a detailed Monte-Carlo simulation study on the Milky Way neutron star population, spanning different assumptions on the Galactic potential and star formation history. In such a work, ten different models were fitted as 4th order polynomials. We take the coefficients given in Table A.1 of this reference, with which the surface densities can be computed. The last one is the "Fiducial $\times 10$" model at 10 Gyr extracted from Ref. [150], which used a numerical Fokker-Planck approach combined with existing data on the stellar population in the Galactic Center.

3.1.3 Neutron Star Structure

The strength of the dark matter annihilation signal will also depend on the final size of the dark matter orbits once inelastic scattering becomes kinematically forbidden. To determine these final orbits, we require the neutron star's internal structure, which we obtain through the Tolman-Volkoff-Oppenheimer (TOV) equation of hydrostatic equilibrium, combined with an appropriate equation of state. Some of the numerical details of this procedure are discussed in Sec. 3.7.1. We use the Brussels-Montreal family of equations of state [151–153]; specifically its BsK-21 iteration, for which analytical representations were constructed in Ref. [153] and are applicable to all neutron star layers. This equation of state indicates agreement with radii and tidal deformability measurements from GW170817 [154, 155], mass and radius fits performed from both gravitational wave and low-energy nuclear data [156], and X-ray observations of pulsars [157, 158].

We will mostly consider a single benchmark neutron star with mass and radius

$$M_{\rm NS} \simeq 1.5 M_\odot \ ,$$
$$R_{\rm NS} \simeq 12.55 \text{ km} \ , \tag{3.5}$$

as determined by our choice of equation of state. The majority of neutron stars in the Galactic Center are predicted to have masses around this value by the most recent star formation history analysis of this region [159]. Furthermore, this value is also in agreement with earlier theoretical works [149, 160] and numerical simulations [161]. Most neutron stars in this region are expected to have formed in an early star formation episode around $\sim 5 - 10$ Gyrs ago [159, 162], and so we will consider their age to be order of multi-gigayear. To simplify our analysis, we will also neglect neutron star rotation in our calculations. For a gigayear-old neutron star evolving in isolation, simple estimates using magnetic dipole models already indicate typical periods of order $0.5 - 2$ s [163, 164], which exceeds the dynamical crossing time of captured dark matter. Although this neglects the possibility of pulsar recycling (see *e.g.* Ref. [165]), we note that the existence of a millisecond pulsar population in this region is currently subject to a high uncertainty. For instance, if a substantial population of these objects were present, it would imply a notable increase in low-mass X-ray binaries compared to observed numbers [166]. In any case, including the effects of rotation would increase the range of inelastic mass splittings accessible to our search. This is because rotation generally allows for more compact neutron star configurations, and therefore greater escape velocities, as the centrifugal force can support heavier masses for a given fixed radius.

3.2 Dark Matter Capture in Neutron Stars

The gravitational infall and capture of dark matter in neutron stars has been extensively studied in the past [70, 80, 116, 117, 167–169]. We limit ourselves to providing a brief overview of the process. A dark matter particle is captured when, while traveling through the neutron star, it loses energy equal to or greater than the halo kinetic energy it had far from the neutron star. For dark matter in the sub-PeV mass regime, neutron stars are particularly efficient at capture: because of their large escape velocity, a single scatter is sufficient for a dark matter particle to lose enough energy and become gravitationally bound. Above the PeV scale, the initial kinetic energy of the dark matter particles is sufficiently large that multiple scatters are required in a single transit for capture.

We will focus on the case where the relic dark matter is initially in its lightest state, and scatters with nucleons into a heavier state through a process of the form [68, 70, 74, 133]

$$\chi_1 + n \to \chi_2 + n \ , \tag{3.6}$$

with a cross-section $\sigma_{\chi n}^{\rm inel}$. Above, n is the scattered nucleon, and χ_1 (χ_2) denotes the lighter (heavier) dark matter state. In Sec. 3.5, we briefly discuss the class of models for which this scenario is applicable. The interstate mass splitting is defined as

$$\delta = m_{\chi_2} - m_{\chi_1} \ . \tag{3.7}$$

Once excited into the heavy state, the dark matter may either decay back into χ_1 after some time, or undergo exothermic scattering of the form $\chi_2 + n \to \chi_1 + n$, with

an energy loss and cross-section similar to the endothermic case [133]. For simplicity, from here forward we will refer to m_{χ_1} as m_χ.

The number of captured dark matter particles per unit time is calculated as [167]

$$C_\chi = \sum_N C_N \ , \tag{3.8}$$

where each contribution C_N is the capture rate for dark matter after N scatterings, given by

$$C_N = \pi R_{\rm NS}^2 \, p_N(\tau) \sqrt{\frac{6}{\pi}} \frac{n_\chi}{v_d} \left[(2v_d^2 + 3v_{\rm esc}^2) - (2v_d^2 + 3v_N^2) \exp\left(-\frac{3(v_N^2 - v_{\rm esc}^2)}{2v_d^2} \right) \right] \ . \tag{3.9}$$

Above, $n_\chi = \rho_\chi / m_\chi$ is the dark matter number density at the neutron star position, v_d is the dark matter halo velocity dispersion, $v_{\rm esc} = \sqrt{2GM_{\rm NS}/R_{\rm NS}}$ is the escape velocity at the neutron star surface measured by a local observer, and v_N is the dark matter velocity after it has undergone N scatters. Our assumptions concerning the dark matter density and velocity dispersion in the Galactic Center are discussed in Sec. 3.1.1. The dark matter velocity after N scatters is determined by the fractional energy loss in each subsequent scatter. Unless the mass splitting is close to the maximum value allowed by kinematics, the fraction of energy lost in an inelastic scattering will be approximately the same as the fraction lost in a pure elastic scattering. For instance, for mass splittings up to about 90% of the maximum value accessible to a neutron star, the energy lost in an elastic scattering differs from the inelastic case by less than 10%. Thus, to simplify our calculations, we follow the calculations of Ref. [167] and take $v_N \equiv v_{\rm esc}(1 - \beta_+/2)^{-N/2}$, where $\beta_+ = 4 m_\chi m_n / (m_\chi + m_n)^2$ as determined by elastic scattering kinematics, and $m_n \simeq 0.93$ GeV is the nucleon mass.

Finally, the factor $p_N(\tau)$ is the probability for capture after N scatters, given by

$$p_N(\tau) = \frac{2}{N!} \int_0^1 (\cos\theta)^{N+1} \tau^N \exp\left(-\tau \cos\theta\right) \, d\left(\cos\theta\right) \ , \tag{3.10}$$

where $\tau = 3\sigma_{\chi n}^{\rm inel} M_{\rm NS}/2\pi R_{\rm NS}^2 m_n$ is the optical depth. This is the ratio between the inelastic dark matter-nucleon cross-section and the cross-section at which dark matter scatters once on average over a distance $2R_{\rm NS}$.

It is also useful to estimate the so-called "saturation" cross-section for which almost all the incoming dark matter is captured by a neutron star (strictly speaking, all of the flux is captured only for an infinitely large cross-section). Above this value, the annihilation signal reaches its peak, defining the ultimate sensitivity of our search. For dark matter between GeV and PeV mass, a single scatter is sufficient for capture. Thus, requiring $\sigma_{\chi n}^{\rm inel} n_n R_{\rm NS} \sim 1$, with $n_n \sim 3M_{\rm NS}/4\pi m_n R_{\rm NS}^3$, provides a reasonable estimate of this cross-section. Above the PeV scale, the above estimate is modified by the fact that N scatters are needed for a dark matter particle to be captured. In this regime, this cross-section must linearly increase with mass, since the dark matter's halo kinetic energy also increases linearly with mass. For our benchmark neutron star, this cross-section is

$$\sigma_{\chi n}^{\rm sat} \simeq 3 \times 10^{-45} \ {\rm cm}^2 \times \max\left[1, \frac{m_\chi}{\rm PeV}\right] \ , \tag{3.11}$$

where the max function reflects the transition between the single- and the multi-scatter capture regime.

3.3 Inelastic Dark Matter Thermalization

Once a dark matter particle is captured, it will progressively lose energy from repeated scatters as it periodically crosses the neutron star. In the absence of any scattering suppression, energy loss proceeds until the dark matter particle settles inside, with a final energy roughly determined by the neutron star temperature. For inelastic dark matter, however, this process may stall before the particle reaches an orbit fully contained within the neutron star volume, if the kinematic threshold for inelastic scattering stops being met at some intermediate energy. Below, we analyze the range of mass splittings and timescales over which this occurs, as well as the distribution of partially thermalized dark matter.

3.3.1 Kinematic Threshold

In the regime $m_\chi \gg m_n$, Pauli blocking effects are negligible, and we may approximate the neutron targets to initially be at rest in a dark matter-nucleon collision. In this limit, the center-of-mass energy is simply

$$E_{\rm CM} = \left(m_\chi^2 + m_n^2 + \frac{2 m_\chi m_n}{\sqrt{1-v^2}} \right)^{1/2} , \tag{3.12}$$

where v is the dark matter velocity as measured by a local observer in the neutron star. Neglecting angular momentum, this velocity parameterized in terms of the Schwarzchild radial coordinate r (see Sec. 3.7.2) reads

$$v(r) = \left(1 - \frac{g_{tt}(r)}{g_{tt}(r_f)} \right)^{1/2} . \tag{3.13}$$

Above $g_{tt}(r)$ is the first diagonal component of the neutron star metric (see Sec. 3.7.1), and r_f is the turning point of the dark matter particle. For captured dark matter, r_f is finite since it is gravitationally bound to the object. On the other hand, for incoming dark matter particles from the halo, one may take $r_f \to \infty$ and $g_{tt}(r_f) \to 1$, which amounts to neglecting the initial halo kinetic energy. Since neutron stars have semi-relativistic escape velocities that are much larger than the halo velocity, this is a reasonable approximation. The relation between r_f and the total energy of the dark matter particle, including the gravitational binding contribution, is specified further below (see also Sec. 3.7.2). For the dark matter to endothermically scatter into the heavier state, we require the total center-of-mass energy of the collision to be

$$E_{\rm CM} \gtrsim m_n + m_\chi + \delta \ . \tag{3.14}$$

Eq. (3.14) determines the kinematic threshold for inelastic scattering to proceed.

3.3.2 Accessible Mass Splittings

With the kinematic condition defined, we estimate the mass splitting range for which the dark matter will only partially thermalize through inelastic interactions. To this end, we first analyze the various energy scales that are relevant for the thermalization process.

In what follows, we define the energy ε of a dark matter particle as the total energy including gravitational binding contribution, see Sec. 3.7.2. Note that ε is in fact $\leq m_\chi$ when the dark matter particle is captured by the neutron star, with the equality setting the boundary between bound and open orbits. In Sec. 3.7.2 , we show that, for a captured dark matter particle, the turning point r_f is related to this

quantity through the relation

$$g_{tt}(r_f) = \left(\frac{\varepsilon}{m_\chi}\right)^2 . \tag{3.15}$$

If the turning point is outside the neutron star volume, this relation simplifies to

$$r_f = \frac{2GM_{\rm NS}}{1-(\varepsilon/m_\chi)^2} . \tag{3.16}$$

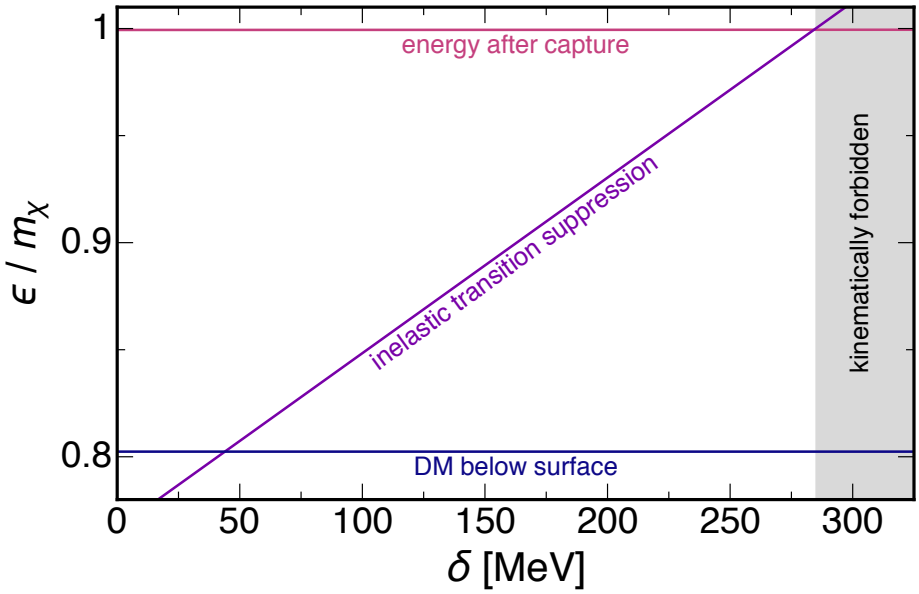

Figure 3.2: Dark matter energy immediately after capture, once the inelastic transition becomes kinematically inaccessible during thermalization, and once the orbits are fully contained within our benchmark neutron star. We also indicate in the shaded area the interstate splitting range where the capture rate is suppressed due to inelastic scattering being kinematically forbidden.

In total, there are three energy scales that must be considered:

1. Prior to capture, the dark matter has an energy $\varepsilon \simeq m_\chi + m_\chi v_d^2/2$ far from the neutron star. Upon capture after N inelastic scatters, the energy of the

particle drops to $\varepsilon = m_\chi$. In other words, just the kinetic energy the particle had far from the neutron star is lost. We then require at least $(N+1)$ inelastic scatterings to obtain an orbit with a finite turning point, $cf.$ Eq. (3.16). The average recoil energy for inelastic scattering in the regime where $\delta \lesssim m_n \ll m_\chi$ is [131]

$$\langle \Delta E_{\rm rec}^{\rm inel} \rangle \simeq \frac{m_n m_\chi^2 \gamma^2 v^2 \left(1 - (\gamma+1)(\delta/m_n)/\gamma^2 v^2\right)}{m_n^2 + m_\chi^2 + 2\gamma m_n m_\chi} \ , \tag{3.17}$$

where $\gamma^{-1} = \sqrt{1-v^2}$. Thus, we take the energy at the beginning of the thermalization process to be of order

$$\varepsilon_i \simeq m_\chi - \langle \Delta E_{\rm rec}^{\rm inel} \rangle - \delta \ , \tag{3.18}$$

where we evaluate $\langle \Delta E_{\rm rec}^{\rm inel} \rangle$ at its minimum value, which is near the neutron star surface.

2. The captured dark matter particles further lose energy through inelastic scatters until the kinematic threshold is no longer met. To obtain the energy at which this occurs, we first solve for v in Eq. (3.14) using the center-of-mass energy Eq. (3.12). For simplicity, we provide here the result in the limit $\delta \lesssim m_n \ll m_\chi$,

$$v_{\rm min} \simeq \sqrt{2}\left(\frac{\delta}{m_n}\right)^{1/2} - \frac{3}{2\sqrt{2}}\left(\frac{\delta}{m_n}\right)^{3/2} \ . \tag{3.19}$$

This expansion is accurate within $\lesssim 10\%$ through the mass splitting range accessible to a typical neutron star. Using Eqs. (3.13) and (3.15), we solve for

the energy, which yields

$$\varepsilon_m \simeq m_\chi \left(\frac{g_{tt}(0)}{1 - v_{\rm min}^2} \right)^{1/2} \ . \tag{3.20}$$

Above, we have explicitly taken $r = 0$ in Eq. (3.13), so that the center-of-mass energy is maximized. This estimate indicates the energy at which a dark matter particle, even passing through the center, where the highest velocity is attained, would not meet the threshold for inelastic scattering.

3. Once inelastic scattering becomes suppressed, if the dark matter is able to elastically scatter at the loop-level, further energy loss proceeds at a much slower rate until the dark matter is eventually fully contained within the neutron star. This occurs when $r_f = R_{\rm NS}$, or equivalently a final energy

$$\varepsilon_{\rm f} = m_\chi \left(1 - \frac{2GM_{\rm NS}}{R_{\rm NS}} \right)^{1/2} \ , \tag{3.21}$$

cf. Eq. (3.16). Numerically, $\varepsilon_f \simeq 0.8\, m_\chi$ for our benchmark neutron star, implying that only a small fraction of the energy relative to the rest mass is lost before the dark matter becomes fully trapped.

Figure 3.2 shows each of these energy scales for our benchmark neutron star, *cf.* Eq. (3.5). The "inelastic transition suppression" line denotes where Eq. (3.14) is violated when the dark matter particles are transiting through the center of the neutron star, where they attain the maximum velocity. The two remaining lines indicate the typical energy once a dark matter particle is captured, and the energy once it becomes fully contained within the neutron star. The intersection of these with the inelastic transition suppression line approximately determines the mass splitting

range for which we obtain a sizable fraction of inelastic dark matter annihilating outside the neutron star. On the one hand, mass splittings below $\delta_{\rm min} \simeq 45$ MeV result in the dark matter thermalizing through inelastic scatterings to the point that is contained inside the neutron star. On the other hand, for mass splittings above $\delta_{\rm max} \simeq 285$ MeV, the energy of the dark matter falling onto the neutron star is insufficient for inelastic scattering to initially proceed. This maximum mass splitting is highlighted by the shaded area.

For completeness, we briefly discuss how this mass splitting window varies with neutron star mass and radius, always assuming a BsK-21 equation of state. The lightest neutron stars in the Milky Way's inner parsec are expected to be of order $M_{\rm NS} \simeq 1.4 M_\odot$ [159]. On the other hand, the heaviest non-rotating neutron star predicted by our choice of equation of state has a mass of order $M_{\rm NS} \simeq 2.2 M_\odot$ [153]. Repeating the above analysis, we obtain mass splitting windows $(\delta_{\rm min}, \delta_{\rm max}) \simeq (40, 260)$ MeV and $(118, 672)$ MeV for the lightest and heaviest neutron star, respectively. Both $\delta_{\rm min}$ and $\delta_{\rm max}$ increase with the neutron star mass because a stronger gravitational field implies that more center-of-mass energy is available to excite the inelastic transition. Thus, $\delta_{\rm min}$ must increase for the dark matter to remain outside after being captured, while $\delta_{\rm max}$ also increases as it becomes possible to capture dark matter with larger interstate splittings. In practice though, we expect most neutron stars will have masses around our chosen benchmark, *cf.* Eq. (3.5), so we take $(\delta_{\rm min}, \delta_{\rm max}) \simeq (45, 285)$ MeV as our viable mass splitting range.

3.3.3 Thermalization Timescale

We now consider the timescale for the captured dark matter particles to thermalize from the energy ε_m at which inelastic scattering stops, to the final energy ε_f at which they are fully contained within the neutron star. This constitutes a lower bound on the total time required for a particle to fully thermalize starting from the initial energy ε_i it has immediately after capture. We compute this lower bound using existing thermalization calculations with elastic interactions [127]. A more exact computation including the initial inelastic thermalization phase would demand accounting for the progressive reduction of phase space available for inelastic scattering as the dark matter loses energy, along with a more detailed modeling of individual particle trajectories, which is outside the exploratory scope of this work. In practice, we require dark matter particles not to become trapped within the neutron star in a short timescale to allow for sizable annihilation outside. Further below, we use this lower bound on that timescale to conservatively estimate how suppressed the elastic cross-section must be relative to the inelastic one for this condition to be met.

Following the approach of Ref. [127], we estimate the energy loss rate of a captured dark matter particle as

$$\frac{d\varepsilon}{dt} = -\frac{\langle \Delta\varepsilon \rangle_{\rm NS}}{t_{\rm orb}(\varepsilon)} \ , \tag{3.22}$$

where $t_{\rm orb}(\varepsilon)$ is the orbital period as a function of energy (see Sec. 3.7.2), and we have introduced the energy loss averaged over the neutron star volume as

$$\langle \Delta\varepsilon \rangle_{\rm NS} \simeq \frac{2}{Z_{\rm NS}} \int_0^{Z_{\rm NS}} \sigma_{\chi n}^{\rm elas} \, \langle E_{\rm rec}^{\rm elas}(z) \rangle \, n_n(z) \, dz \ , \tag{3.23}$$

where $dz = \sqrt{-g_{rr}(r)}\, dr$ is the proper depth element of the neutron star, $Z_{\rm NS}$ is

the integrated proper radius (valid for a stationary metric), and $\sigma_{\chi n}^{\rm elas}$ is the elastic dark matter-nucleon cross-section, which we assume to be smaller than its inelastic counterpart. The factor $\langle E_{\rm rec}^{\rm elas}(z)\rangle$ is the average energy transfer for elastic scattering, which is a function of depth, as this determines the kinetic energy. This is given by [82]

$$\langle E_{\rm rec}^{\rm elas}\rangle = \frac{m_n m_\chi^2 \gamma(r)^2 v(r)^2}{m_n^2 + m_\chi^2 + 2\gamma(r) m_n m_\chi} \ , \tag{3.24}$$

where $v(r)$ is given by Eq. (3.13). The additional factor of 2 in Eq. (3.23) accounts for the dark matter particles transiting all neutron star layers twice.

We then integrate Eq. (3.22) from $\varepsilon = \varepsilon_m$ to $\varepsilon = \varepsilon_f$, which gives the approximate timescale for which dark matter is trapped within the neutron star exclusively through loop-suppressed elastic interactions

$$t_{\rm therm} \simeq -\int_{\varepsilon_m}^{\varepsilon_f} \frac{t_{\rm orb}(\varepsilon)}{\langle \Delta\varepsilon\rangle_{\rm NS}}\, d\varepsilon \ . \tag{3.25}$$

Below, we compare this timescale to the time it takes for the dark matter to annihilate while its orbit is extends beyond the neutron star volume. We remark that we have neglected here any coherent nuclear enhancement factors that occur in the crust of the neutron star. While these enhancement factors can be significant [127], the overall optical depth of the crust is usually a subdominant contribution to the total optical depth of the star.

3.3.4 Capture-Annihilation Equilibrium

The total number of dark matter particles bound to the neutron star will evolve according to

$$\frac{dN_\chi}{dt} = C_\chi - \frac{\langle \sigma_{\rm ann} v_{\rm rel} \rangle N_\chi^2}{V} \,, \tag{3.26}$$

where $\langle \sigma_{\rm ann} v_{\rm rel} \rangle$ is the thermally averaged dark matter annihilation cross-section $\sigma_{\rm ann}$ multiplied by the relative velocity $v_{\rm rel}$, and V is the proper volume where annihilation proceeds. For a recent discussion on partially thermalized dark matter annihilation with velocity- and momentum transfer-dependent operators, see Ref. [34]. For inelastic dark matter that has only been partially thermalized with a neutron star, both the relative velocity and the volume will be approximately determined by the characteristic size of the orbits once the inelastic transition becomes suppressed. The latter is obtained through the integration of $dV = 4\pi r^2 dr/\sqrt{-g_{rr}(r)}$ over the interval defined by the turning point of the dark matter particles once the inelastic transition becomes suppressed.

In our analysis, we expand the annihilation cross-section in terms of partial waves as

$$\langle \sigma_{\rm ann} v_{\rm rel} \rangle = \langle \sigma_{\rm ann} v_{\rm rel} \rangle_0 \sum_{l=0}^{\infty} a_l \, v_{\rm rel}^{2l}, \tag{3.27}$$

and analyze each contribution individually by setting $a_l = 1$ for some specific mode l and setting all remaining coefficients to zero. As our benchmark, we will take $\langle \sigma_{\rm ann} v_{\rm rel} \rangle_0 = 3 \times 10^{-26}$ cm^3 s^{-1}. We will focus on the most commonly considered s-wave ($l = 0$) and p-wave ($l = 1$) modes.

For the initial condition $N_\chi(t=0)=0$, the solution to Eq. (3.26) is

$$N_\chi(t) = N_{\rm eq}\tanh\left(\frac{t}{t_{\rm eq}}\right) \ , \tag{3.28}$$

where we have defined the capture-annihilation equilibrium timescale as

$$t_{\rm eq} = \left(\frac{V}{C_\chi\langle\sigma_{\rm ann}v_{\rm rel}\rangle}\right)^{1/2} \ . \tag{3.29}$$

Once $t \gtrsim t_{\rm eq}$, the number of dark matter particles reaches an equilibrium value approximately given by

$$N_{\rm eq} \simeq C_\chi\, t_{\rm eq} \ , \tag{3.30}$$

and dark matter annihilation must then proceed at a steady-state rate given by

$$\Gamma_{\rm ann} = \frac{C_\chi}{2} \ , \tag{3.31}$$

where the factor of 2 reflects that two dark matter particles are depleted per annihilation event.

Figure 3.3 shows the s-wave and p-wave equilibration timescale as a function of mass splitting for our benchmark neutron star. In the p-wave case, we take the relative velocity as approximately the dark matter velocity averaged over one orbital cycle. For the capture rate, we have taken $\rho_\chi \simeq 7.25\times10^3$ GeV cm^{-3}, corresponding to a standard NFW profile at $R=1$ pc from the Galactic Center, and an inelastic cross-section $\sigma_{\chi n}^{\rm inel} \simeq 10^{-45}$ cm^2, corresponding to approximately the lowest value for which a prospective gamma-ray signal might be observed by future gamma-ray telescopes. These values fix the capture rate to about the lowest value for which even neutron

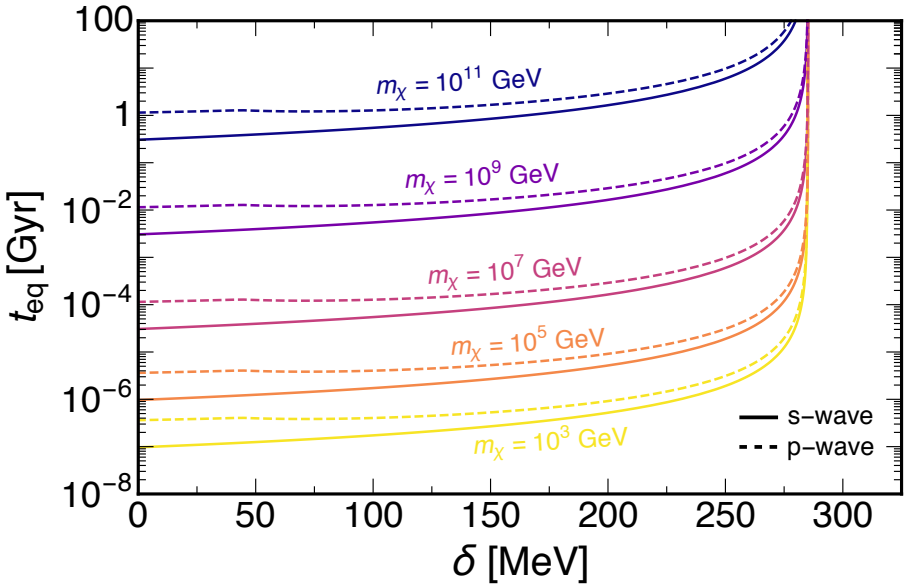

Figure 3.3: Capture-annihilation equilibrium timescale for our benchmark neutron star and various dark matter masses as indicated, for s-wave and p-wave channels. For this plot, we have taken a dark matter velocity dispersion $v_d = 270$ km s^{-1} and density $\rho_\chi \simeq 7.25 \times 10^3$ GeV cm^{-3}, the latter corresponding to an NFW profile at $R \simeq 1$ pc. The inelastic cross-section has been fixed to $\sigma_{\chi n}^{\rm inel} = 10^{-45}$ cm^2, approximately the lowest value for producing a potentially observable gamma-ray signal with upcoming telescopes under these assumptions.

stars near the edge of our region of interest would contribute to an observable signal. For these conservative assumptions, we see that capture-annihilation equilibrium is reached within typical neutron star ages for all the mass range analyzed, so long as δ is not too close to $\delta_{\rm max}$. When $\delta \to \delta_{\rm max}$, the turning point of the dark matter particle orbit diverges, which is equivalent to no particle being captured. As a result, the equilibration time diverges in this limit.

Finally, we address the effects of loop-level elastic scattering on the annihilation equilibrium. For a sizable amount of dark matter to annihilate outside the neutron star, the timescale for it to fully sink below the surface must be longer than the

timescale it takes to achieve capture-annihilation equilibrium. This hierarchy between timescales is ultimately determined by how suppressed the elastic cross-section is relative to its inelastic counterpart. We provide an estimate of the suppression required by comparing the time to thermalize $t_{\rm therm}$ to $t_{\rm eq}$, where we evaluate the latter at $R = 1$ pc for an NFW profile. This is extremely conservative, since most of the signal is produced by neutron stars much closer to the Galactic Center. Such neutron stars achieve capture-annihilation equilibrium on a timescale much shorter than those at $\sim$ pc distances. Moreover, as mentioned above, our thermalization timescale is in fact an underestimate, since we do not account for the initial inelastic thermalization stage. Under these conservative assumptions, equating $t_{\rm therm} = t_{\rm eq}$ and solving for the elastic cross-section, we obtain

$$\sigma_{\chi n}^{\rm elas} \lesssim 10^{-57}\ {\rm cm}^2\, F(\delta) \left(\frac{\rho_\chi}{\rho_\chi^{\rm NFW}(R = 1\ {\rm pc})}\right)^{1/2} \times \left(\frac{\sigma_{\chi n}^{\rm inel}}{10^{-45}\ {\rm cm}^2}\right)^{1/2} \max\left[\left(\frac{m_\chi}{\rm PeV}\right)^{1/2}, 1\right] \tag{3.32}$$

for our benchmark neutron star. To derive this, we have used the linear and inverse scaling of $t_{\rm therm}$ (*cf.* Eq. (3.25)) with dark matter mass and elastic cross-section, respectively. We have also used the approximate linear scaling of the capture rate with the ratio $\sigma_{\chi n}^{\rm inel}/\sigma_{\chi n}^{\rm sat}$, which enters $t_{\rm eq}$. The function $F(\delta)$ encapsulates the remaining dependence on the mass splitting and must be computed numerically. This function diverges for $\delta \to \delta_{\rm min,max}$. This is because when $\delta \to \delta_{\rm min}$, the dark matter is already almost completely thermalized through inelastic scattering. On the other hand, if $\delta \to \delta_{\rm max}$, the capture-annihilation equilibration time diverges because the turning point of the dark matter particles becomes infinite, making the volume where annihilation

proceeds infinitely large. However, for mass splittings $\sim 10\%$ above $\delta_{\rm min}$ and $\sim 90\%$ below $\delta_{\rm max}$, $F(\delta)$ ranges between 10^{-2} and 1. We reiterate that higher elastic cross-section values are allowed without impacting on the signal strength, as Eq. (3.29) was evaluated at $R = 1$ pc , and we have used a lower bound on the actual thermalization time. In particular, neutron stars closer to the Galactic Center, due to the higher dark matter density, have much shorter capture-annihilation equilibrium times and thus admit much less suppressed elastic cross-sections while still having a sizable amount of dark matter annihilating outside. In Sec. 3.5, we discuss what class of models generate elastic cross-sections that are suppressed relative to their inelastic counterparts.

3.3.5 Annihilation Rate Outside

With the timescales for thermalization and capture-annihilation equilibrium outlined, we now turn to estimating the fraction of dark matter that will annihilate outside the neutron star volume. As we discuss in Sec. 3.7.3, we approximate the number density of dark matter particles seen by a local observer as

$$n_\chi(r) = n_\chi^0 \left(1 - v(r)^2\right)^{1/2} \ , \tag{3.33}$$

where n_χ^0 is a normalization constant determined by the steady-state number of captured dark matter particles. The orbital velocity $v(r)$ is evaluated for a fixed particle's energy $\varepsilon = \varepsilon_m$ since we are focusing on the regime where $t_{\rm eq} \ll t_{\rm therm}$. In other words, once the inelastic transition can no longer be excited, the dark matter will annihilate long before the orbit changes significantly through suppressed elastic scatterings. The normalization factor is, in fact, irrelevant for determining the fraction of the

total annihilation rate occurring outside. Rather, for turning points $r_f \geq R_{\rm NS}$ we are interested in the ratio

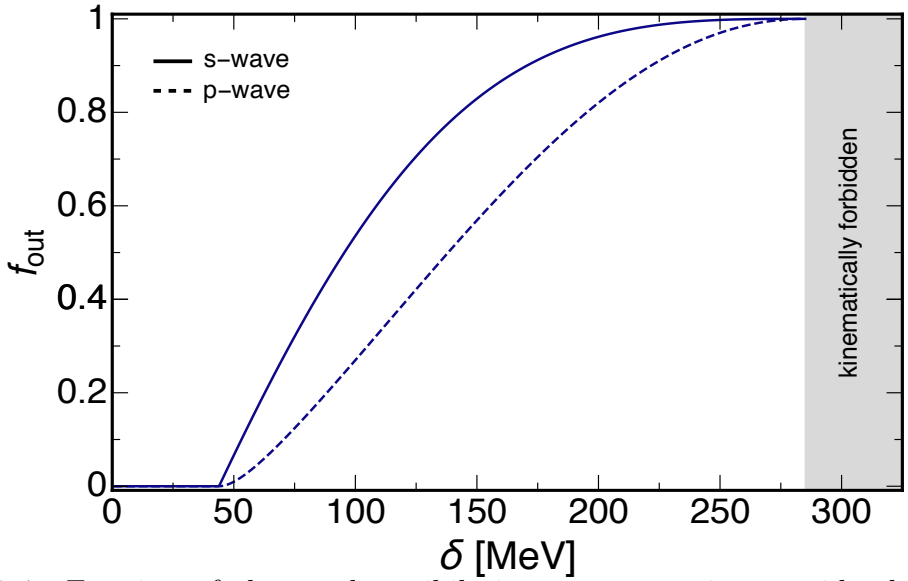

Figure 3.4: Fraction of the total annihilation rate occurring outside the neutron star volume as a function of interstate splitting, for s-wave and p-wave annihilation channels as indicated. The shaded region indicates the maximum mass splitting for which the inelastic transition can be excited when the dark matter initially approaches the neutron star at approximately the escape velocity.

$$f_{\rm out} = \frac{\int_{R_{\rm NS}}^{r_f} n_\chi^2(r) \langle \sigma_{\rm ann} v_{\rm rel} \rangle \, dV}{\int_0^{r_f} n_\chi^2(r) \langle \sigma_{\rm ann} v_{\rm rel} \rangle \, dV} \ , \tag{3.34}$$

where $f_{\rm out} \in [0, 1]$ is the estimated fraction of the annihilation rate that proceeds outside the neutron star volume. As before, we expand $\langle \sigma_{\rm ann} v_{\rm rel} \rangle$ into partial waves and individually analyze each mode.

Figure 3.4 shows the fraction of the annihilation rate outside our benchmark neutron star as a function of inelastic mass splitting. We show this fraction for both s-wave and p-wave channels. For mass splittings $\delta \gtrsim \delta_{\rm min}$, the fraction grows until it is maximal at $\delta \simeq \delta_{\rm max}$. For the velocity-dependent p-wave channel, the dark matter

annihilates more efficiently when closer to the neutron star surface, where a higher velocity is attained. This results in a smaller fraction annihilating outside compared to the s-wave mode for a given splitting. Note that although the fraction annihilating outside grows with mass splitting, the overall signal at large mass splittings will be weaker because the capture efficiency is suppressed for splittings sufficiently close to the maximum value.

3.4 Neutrino and Gamma-Ray Signals

If dark matter capture-annihilation equilibrium is attained, the annihilation rate around a neutron star is determined by the capture rate itself. From this, we can construct the signal by integrating the capture rate from the neutron star population within the Galactic Center. To compare results across various possible combinations of neutron star and dark matter density profiles, it is useful to introduce the capture rate density as

$$\rho_{C_\chi}(R) = \eta_{\rm NS}(R) \times C_\chi(R) \ , \tag{3.35}$$

where $\eta_{\rm NS}$ is the neutron star number density. Above, we have explicitly indicated that the capture rate C_χ for a neutron star is a function of Galactocentric distance R, as it is proportional to the dark matter density where the neutron star is positioned.

Figure 3.5 shows the capture rate density for each combination of neutron star and dark matter distribution we consider. Overall, the cuspier gNFW profile predicts the largest dark matter capture rate on neutron stars at the Galactic Center, for any assumed neutron star distribution model. Degeneracies between the chosen dark matter and neutron star distributions only show up at Galactocentric distances $\gtrsim$ 10 pc, where the dark matter density is so small that neutron stars in this range do

not significantly contribute to the total annihilation signal. As we show below, this means the strongest limits and projections are obtained for the gNFW profile. We also note that, for a fixed dark matter distribution, the variation between the different neutron star models is about a factor of 5 at small Galactocentric distances.

For any combination of neutron star and dark matter distribution, the capture rate density drops steeply away from the Galactic Center. Because of this, we find the dominant component of the signal comes from the innermost region of the Galactic Center. Therefore, for the purposes of computing fluxes of high-energy annihilation byproducts, we model the neutron star population as a single point source, with a total annihilation rate

$$\Gamma_{\rm ann}^{\rm tot} = \frac{1}{2} \int_{R_{\rm min}}^{R_{\rm max}} \rho_{C_\chi}(R)\, 4\pi R^2\, dR \ . \tag{3.36}$$

We adopt a lower integration limit $R_{\rm min} = 10^{-2}$ pc to avoid the large uncertainties in both dark matter and stellar velocities near the Galactic Center. The upper cutoff depends on the range of the neutron star distribution chosen. The maximum distance we integrate over is $R_{\rm max} = 50$ pc, and we do not extrapolate any neutron star distribution beyond this point. In any case, most of the contribution to the signal is produced by the neutron stars closer to $R_{\rm min}$, where the dark matter density is considerably higher.

Using this single point source approximation, the spectral flux of neutrinos or γ-rays at Earth is

$$\left.\frac{d\Phi_j}{dE_j}\right|_{\rm ch} = f_{\rm out} \times \frac{\Gamma_{\rm ann}^{\rm tot}}{4\pi D^2} \times \left.\frac{dN_j}{dE_j}\right|_{\rm ch} , \tag{3.37}$$

where $j = \nu_\alpha$ or γ denotes the final observed state of a channel ch, E_j is the energy,

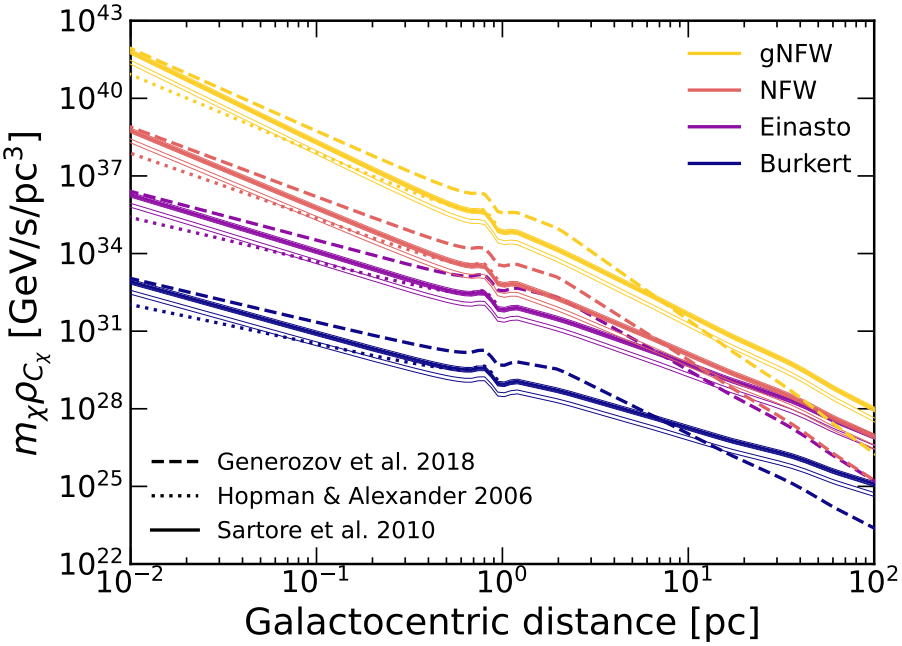

Figure 3.5: Capture rate density for the various combinations of neutron star distributions and dark matter density profiles as specified. Different solid lines for each dark matter profile correspond to the multiple fitting models discussed in Ref. [85]. The power-law distribution of Ref. [149] is terminated beyond ~ 1 pc.

and $D \simeq 8.5$ kpc is the approximate Earth-Galactic Center distance. The factor $dN_j/dE_j|_{\rm ch}$ denotes the neutrino/γ-ray spectrum per annihilation for a channel ch. For sufficiently energetic γ-rays, Eq. (3.37) is also multiplied by a survival probability that accounts for the attenuation through the interstellar medium (see below).

To span a range of spectral fluxes from soft to hard, we will consider three benchmark channels where dark matter annihilates exclusively to $b\bar{b}$, $\tau^+\tau^-$ and W^+W^-. We will also consider direct annihilation to neutrinos and γ-rays to illustrate the maximum reach of our search using neutrino and γ-ray telescopes, respectively. For the direct neutrino channel, we assume an equal contribution from each flavor. The neutrino and γ-ray spectra are computed using `HDMSpectrum` [170], which includes a

state-of-the-art treatment of electroweak interactions. Note that, due to electroweak showers, a flux at energies below the dark matter mass is expected even for the direct neutrino/γ-ray channel, which makes it possible to probe dark matter with mass larger than the maximum energy reach of an experiment in this case. At the same time, due to the electroweak interactions, we also expect a neutrino (γ-ray) flux from the direct γ-ray (neutrino) annihilation channel.

3.4.1 Sensitivity of Neutrino Telescopes

We compute the sensitivity of IceCube and IceCube-Gen2 [171], the next generation of IceCube at the South Pole. Detectors in the Southern Hemisphere, like IceCube, have a superior sensitivity to the Galactic Center at energies below hundreds of TeV, as the Earth shields the atmospheric muons, while a good view of the Southern Sky is also expected at higher energies due to the absence of neutrino flux attenuation by the Earth. An event selection also imposes a higher energy threshold, which can further suppress the atmospheric muon background. On the other hand, detectors in the Northern Hemisphere can bring complementary features, so we analyze these as well. There are various water Cherenkov telescopes either under construction or proposed in the Northern Hemisphere, such as Baikal-GVD, KM3NeT, P-ONE, TRIDENT, and the newly proposed HUNT [172–176]. Thus, we also report on the detectability of our signal using KM3NeT and TRIDENT. Baikal-GVD and P-ONE are expected to reach comparable sensitivity as KM3NeT with the current information on the detector installation and performance. In-ice/water Cherenkov detectors run out of sensitivity beyond $\sim$ 10 PeV energies. For the detection of ultra-high-energy neutrinos above this threshold, we forecast the sensitivity of the proposed IceCube-Gen2 radio [171],

which is expected to have the optimal sensitivity towards the Southern Sky.

Since we are considering a point source signal, we study track events induced by charged-current interactions of muon neutrinos, which have ideal pointing power. The expected signal track events in an energy bin i can be written as

$$N_{\mu,i} = T \times \frac{1}{3} \sum_{\alpha=1}^{3} \int_{E^{\min}_{\nu_\mu,i}}^{E^{\max}_{\nu_\mu,i}} A_{\text{eff}}(E_{\nu_\mu}) \left. \frac{d\Phi_{\nu_\alpha}}{dE_{\nu_\alpha}} \right|_{\text{ch}} dE_{\nu_\mu} \ , \tag{3.38}$$

where A_{eff} is the effective area, which depends on the neutrino energy E_{ν_μ} for the signal from a specific direction, and T is the exposure time, which we set to 10 yr for our sensitivity estimation. The integration limits $E^{\min}_{\nu_\mu,i}$ and $E^{\max}_{\nu_\mu,i}$ correspond to the energy bounds of bin i. As the neutrino flux at detection is the flux after neutrino oscillation, we consider an equal contribution of each flavor in the total neutrino flux at Earth. When considering the high-energy neutrino telescopes, we use A_{eff} from the IceCube point-source data release [177]. The A_{eff} for KM3Net and IceCube-Gen2 is from the `PLE`ν`M` framework, which computes effective areas based on a detector location transfer and size scaling of the A_{eff} of IceCube [178]. The A_{eff} of TRIDENT is obtained from Figure 15 of Ref. [175]. For the ultra-high-energy regime, the diffuse neutrino flux sensitivity is computed with an expectation of 2.44 events per energy decade. Thus, we obtain the A_{eff} for IceCube-Gen2 radio from its reported energy-dependent sensitivity ϕ_{sens} in Figure 19 of Ref. [171], by taking [179]

$$A_{\text{eff}}(E_\nu) = \frac{2.44\, E_\nu}{4\pi T \ln(10)\, \phi_{\text{sens}}(E_\nu)} \ , \tag{3.39}$$

where the exposure time here has $T = 10$ yr.

We compute the sensitivity based on a likelihood ratio test

$$\mathcal{L} = e^{-N_\mu} \prod_i \frac{N_{\mu,i}^{N_{\mu,i}^{\rm obs}}}{N_{\mu,i}^{\rm obs}!} \ , \tag{3.40}$$

where $N_\mu = N_\mu^{\rm sig} + N_\mu^{\rm bkg}$ is the expected total number of μ-tracks from the signal and the background (the latter is detailed below). The superscript *obs* is used for the observed number of events and i indicates the bin. By Wilks' theorem, we have $\chi^2 = -2\log\left[\mathcal{L}\left(N_\mu^{\rm sig}=0\right)/\mathcal{L}\left(\hat{N}_\mu^{\rm sig}\right)\right]$, where $\hat{N}_\mu^{\rm sig}$ is the value that maximizes the ratio. Considering the χ^2 distribution with 1 degree of freedom, we define our 90% sensitivity as $\chi^2 = 2.7$.

For high-energy neutrino detection, the main background is composed of atmospheric neutrinos and the diffuse astrophysical neutrino flux. We fix the atmospheric neutrino flux to the conventional flux given by the `MCEq` simulation with cosmic-ray flux model H3a, hadronic model SIBYLL-2.3c, and atmosphere model NRLMSISE-00 [181–183]. For the diffuse astrophysical neutrino flux, we incorporate the best-fitted spectrum of astrophysical muon neutrinos [184]. The angular resolution plays an important role in a point-source search for the background suppression power. The angular resolution of an in-water detector is expected to be better than an in-ice experiment due to less Cherenkov light scatterings. For our work, we consider the energy-dependent angular resolutions from Ref. [185] for IceCube and IceCube-Gen2, and from Ref. [173] for other in-water experiments. In the ultra-high-energy range, the atmospheric background is negligible, but there is a diffuse cosmogenic neutrino flux expected from cosmic rays interacting with the cosmic microwave background and the extragalactic background light [186]. In this case, we construct the background taking into account the predicted cosmogenic neutrino flux from cosmic-ray

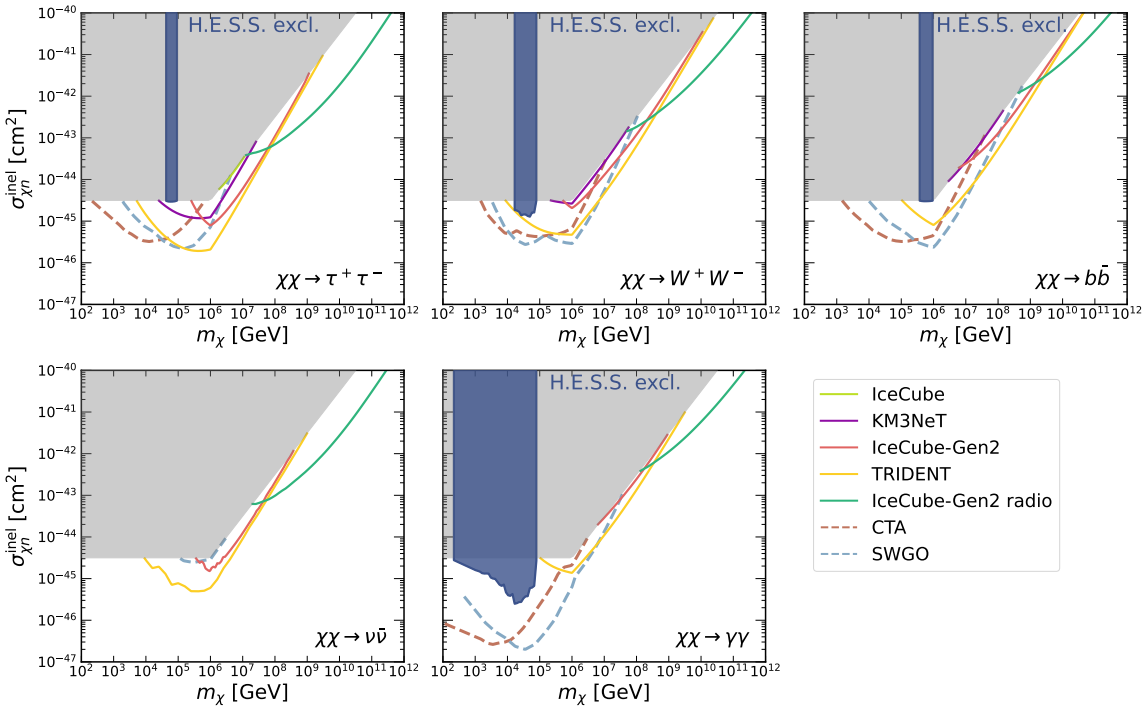

Figure 3.6: Inelastic dark matter-nucleon cross-section constraints derived from H.E.S.S. Galactic Center γ-ray observations [180] (**blue**), assuming a gNFW profile and a fraction $f_{\rm out} = 0.95$ of dark matter annihilating outside neutron stars. Also shown are 90% sensitivities for neutrino telescopes (**solid**) with a 10 yr exposure in all cases, and projected 5σ-sensitivities of future Southern Hemisphere γ-ray observatories (**dashed**) with a 50 hr exposure for CTA and 5 yr exposure for SWGO. Projections are drawn using the most optimistic neutron star density model. For reference, we indicate the inelastic cross-section for which approximately all the incoming dark matter is captured (**grey**); projections and bounds terminate on this line when their observational sensitivity threshold requires more dark matter annihilation than can be produced by all dark matter falling onto the Galactic Center neutron stars.

studies [187]. The direction of a neutrino event in a future Askaryan detector can reach within 1° [188], and so we take 1° for our work when estimating the sensitivity of IceCube-Gen2 radio. Since we consider neutron stars up to 50 pc from the Galactic Center, which corresponds to $\sim 0.3°$, we also include this angular extension when computing the background for both high-energy and ultra-high-energy detection.

3.4.2 Sensitivity of γ-Ray Observatories

There are various running or proposed ground-based γ-ray experiments with sensitivity to very-high-energy γ-rays. We will focus on those located in the Southern Hemisphere, which have exposure to the Galactic Center. Note that at energies above tens of TeV, attenuation due to the pair production mainly with the cosmic microwave background and the infrared emission by dust become non-negligible for γ-rays as they propagate through the interstellar medium [189]. We incorporate this correction by multiplying Eq. (3.37) by a survival probability given by

$$P_{\rm surv} = \exp\left(-\tau_{\gamma\gamma}(E_\gamma)\right) \ , \tag{3.41}$$

where $\tau_{\gamma\gamma}(E_\gamma)$ is the energy-dependent optical depth between the Galactic Center and an observer at the Milky Way. We use the optical depth data from Ref. [189].

We compute inelastic cross-section constraints from existing observations performed by the High Energy Stereoscopic System (H.E.S.S.), which currently has the leading sensitivity for very-high-energy γ-rays toward the Southern Sky. To draw these limits, we compare our predicted fluxes to the energy differential fluxes reported in the Galactic Plane Survey [180], which roughly cover an energy range of about $0.1 - 100$ TeV, and require that our flux must not exceed the observed flux in

any energy bin.

We also forecast the sensitivity of the Southern Array of the Cherenkov Telescope Array (CTA) and the Southern Wide-field Gamma-ray Observatory (SWGO), which will significantly improve observations of the Galactic Center in the near future. The energy differential point-source sensitivities of these telescopes have been evaluated in Refs. [190, 191], which correspond to a total observation time of 50 hours with the Southern Array of CTA and a 5 yr exposure for SWGO. The projected sensitivity for each case is then obtained following the same procedure as with H.E.S.S. observations. Note that the reported sensitivities in Refs. [190, 191] correspond to a 5σ detection while constraints on dark matter studies are usually at the 90% confidence level.

3.4.3 Results

Figure 3.6 shows our computed dark matter-nucleon inelastic cross-section limits based on H.E.S.S. γ-ray data and projected sensitivities of upcoming neutrino and γ-ray observatories, for the gNFW profile. These are shown for the annihilation channels specified at the start of Sec. 3.4. For concreteness, we have assumed all neutron stars to be given by our benchmark (see Sec. 3.1), and fixed $f_{\rm out} = 0.95$ (all projected limits scale linearly with this parameter). This corresponds to an inelastic mass splitting of about 190 MeV (239 MeV) for s-wave (p-wave) annihilation mode, *cf.* Figure 3.4. For reference, we also show the cross-section at which nearly all the incoming dark matter is captured by a neutron star. Sensitivity is lost above this line because the capture rate of neutron stars is maximized, and thus, higher cross-sections do not physically increase the annihilation signal. In all cases, we have used the most optimistic neutron star distribution. However, we note that the variation

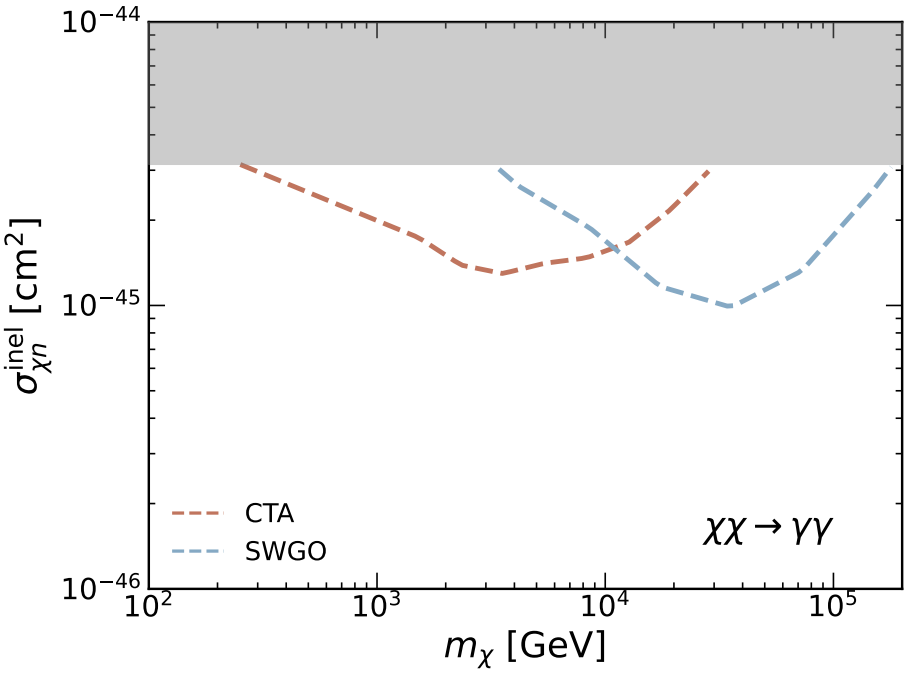

Figure 3.7: Projected sensitivities for CTA and SWGO to inelastic dark matter-nucleon cross-sections shown for the direct γ-ray annihilation channel, assuming an NFW profile. Otherwise same as Fig. 3.6.

of our results between all neutron star distributions is about a factor ~ 5. Advances in our understanding of star formation in the Milky Way's nuclear star cluster will reduce this uncertainty.

As expected, the strongest sensitivity is attained for the steeper gNFW profile, with H.E.S.S. limits reaching down to $\sim 3 \times 10^{-46}$ cm^2 while the strongest projections achieve $\sim 2 \times 10^{-47}$ cm^2 for direct annihilation to γ-rays. Note that, for both the gNFW and NFW profiles, the halo annihilation signal can be comparable to the signal sourced by neutron stars for s-wave annihilation below $\sim$ PeV masses. For velocity-dependent annihilation, such as p-wave and higher modes, the neutron star signal will be significantly stronger than its halo counterpart. Using the conservative assumptions laid out in this first exploratory analysis, we did not find robust search

prospects for an NFW profile, except for some limited sensitivity in the mass range $\sim 1-100$ TeV, using the future reach of CTA and SWGO in the direct γ-ray channel, as shown in Figure 3.7. It is possible that future analyses treating the thermalization of inelastic dark matter and capture-annihilation equilibration using less conservative assumptions could find γ-ray and neutrino flux sensitivity for an NFW profile. For the Einasto and Burkert profiles, the dark matter content in the Galactic Center is too low to achieve sensitivity in any channel.

The sharp loss in constraining power for the direct γ-ray channel above ~ 100 TeV is due to the observable signal switching from a line-emission-like signal at the dark matter mass to an electroweak shower at lower energies. This also applies to the W^+W^- channel. Neutrino experiments, on the other hand, have ample sensitivity to energies beyond the PeV scale, and thus achieve the best projections for heavy inelastic dark matter. For the direct neutrino channel, our forecasted sensitivity reaches $\sim 4 \times 10^{-46}$ cm^2. Depending on the dark matter profile, IceCube-Gen2 radio will obtain leading constraints on the inelastic cross-section for ultra-heavy dark matter. The Southern Array of CTA and SWGO will also achieve a sensitivity comparable to that of neutrino experiments up to ~ 10 PeV masses, except for the direct neutrino channel to which neutrino experiments are naturally more sensitive.

3.5 Models for Inelastic Dark Matter

Inelastic dark matter models have been widely considered in the past, for example, as a way of addressing outstanding astrophysical excesses [133, 192–194] or small-scale structure problems [195–197] while remaining consistent with null results from direct detection searches. In the most minimal realization, a small Majorana mass term is

introduced, which splits the Dirac dark matter into two neutral components with a mass difference set by the Majorana mass. Motivated by the self-interacting dark matter scenario, we illustrate the applicability of our search with a simple inelastic dark photon-mediated dark matter model [70].

Recalling from section 2.4.2, we know that in dark matter models mediated by dark photons, the inter-state mass splittings arise due to the spontaneous symmetry breaking of the $U(1)_D$ gauge symmetry by the scalar boson that couples to the dark matter. This interaction can be described by the Lagrangian given by Eq. 2.4, which we restate here for ease of reference-

$$\begin{aligned}\mathcal{L} = \mathcal{L}_{\rm SM} + |D_\mu \phi|^2 + V(\phi) - \frac{1}{4}V_{\mu\nu}^2 + \kappa V_\mu \partial_\nu F^{\mu\nu} \\ - \frac{1}{2}m_V^2 V_\mu^2 + \bar{\chi}\left(iD_\mu\gamma_\mu - m_\chi\right)\chi + \left(\lambda_D \phi \chi^T C^{-1} \chi + \text{h.c.}\right) \ ,\end{aligned} \tag{3.42}$$

where V_μ ($V_{\mu\nu}$) is the new $U(1)_D$ gauge boson (field strength tensor) which mixes with the SM photon with a kinetic mixing parameter κ, $D_\mu \equiv \partial_\mu + ie_D V_\mu$ where e_D is the charge of the dark matter under $U(1)_D$, and C is the charge conjugation matrix. The mass splitting is achieved through spontaneous symmetry breaking of the $U(1)_D$ by a scalar ϕ that also couples to the dark matter. We focus on the heavy dark photon parameter space of masses $m_V \gtrsim 1$ GeV, which is currently relatively unconstrained. The value of $\alpha_D = e_D^2/4\pi$ can be fixed by requiring, for example standard thermal freeze-out. However, to illustrate our point, we remain agnostic about the cosmological formation history.

To establish the broad applicability of our search strategy, we consider a minimal dark photon model in which the mass splitting between the two mass eigenstates is set by a scalar vacuum expectation value. For reasonable parameters, the resulting

splitting between the mass eigenstates can be of order

$$\delta \simeq \lambda_D v_\phi = 100 \text{ MeV} \left(\frac{\lambda_D}{0.1}\right) \left(\frac{v_\phi}{\text{GeV}}\right) , \tag{3.43}$$

where v_ϕ is the vacuum expectation value of the scalar. At this mass splitting, endothermic scattering in direct detection searches is kinematically forbidden for virialized halo dark matter, while in a typical neutron star, it can be captured but will only partially thermalize with it.

Once captured through the dark photon portal, dark matter scatters off charged particles in a neutron star, which comprise about a few percent of the total particle number (see *e.g.* [198]). The inelastic dark matter-proton cross-section dominates over the electron cross-section and is given by

$$\begin{aligned} \sigma_{\chi p}^{\text{inel}} &= \frac{16\pi\alpha\alpha_D\kappa^2 m_p^2}{m_V^4} \\ &\simeq 1.2 \times 10^{-43} \text{ cm}^2 \left(\frac{\kappa}{10^{-5}}\right)^2 \left(\frac{\alpha_D}{0.1}\right) \left(\frac{10 \text{ GeV}}{m_V}\right)^4 , \end{aligned} \tag{3.44}$$

which can be well above the necessary value to maximize capture, even accounting for the said reduction in the number of scattering targets for this specific SM portal. By contrast, the loop-level elastic scattering cross-section is

$$\begin{aligned} \sigma_{\chi p}^{\text{elas}} &= \frac{\alpha^2\alpha_D^2\kappa^4 m_n^4 f_q^2}{\pi m_V^6} \\ &\simeq 5.1 \times 10^{-63} \text{ cm}^2 \left(\frac{\kappa}{10^{-5}}\right)^4 \left(\frac{\alpha_D}{0.1}\right)^2 \left(\frac{10\,\text{GeV}}{m_V}\right)^6 , \end{aligned} \tag{3.45}$$

where $f_q \sim 0.1$ is a hadronic matrix element [70]. These cross-sections imply efficient inelastic capture in neutron stars, but thermalization is extremely slow if the inelastic

transition becomes kinematically suppressed. Note that for the dark photon mass range considered, the heavy state will be long-lived, as it is unable to decay by dark photon emission. Thus, in the multiscatter capture regime, it must exothermically decay back into the light state. Note that the kinetic mixing values we consider lie significantly below current limits from visible final state searches at accelerators [199–201].

The captured dark matter then annihilates predominantly into dark photons, which rapidly decay to charged particles and subsequently produce γ-rays. Dark photons with masses $m_V \gg 1$ GeV decay to Standard Model leptons in a time of order $(\alpha\kappa^2 m_V/3)^{-1} \sim 10^{-13}\ \mathrm{s}\,(10^{-5}/\kappa)^2\,(10\ \mathrm{GeV}/m_V)$, and for hadronic final states, this lifetime changes by an order one factor given by the hadron-to-muon production cross-section ratio in e^+e^- annihilation, see *e.g.* [202]. The resulting decay length will be much shorter than the neutron star size unless the boost factor is of order $m_\chi/m_V \gtrsim 10^8$, which is not achieved in a sizable region of the parameter space considered. This implies that only partially thermalized inelastic dark matter annihilating outside a neutron star will source a potentially observable signal.

This simple model realization thus illustrates the wide class of models for which our search would have ample sensitivity, while direct detection rates would be severely suppressed. Although a neutron star kinetic heating search would also be applicable to this scenario, we emphasize that it is contingent upon the existence of nearby faint neutron stars and lengthy observation times with infrared telescopes.

3.6 Conclusion

We have analyzed for the first time the annihilation of inelastic dark matter outside neutron stars. This effect arises because, after being captured, the dark matter particles are unable to fully thermalize with the neutron star due to inelastic kinematics. If elastic interactions are suppressed relative to the inelastic channel, these can remain in long-lived orbits that extend beyond the neutron star volume, allowing for a sizable fraction to annihilate outside. For interstate splittings approximately within $45 - 285$ MeV, a significant fraction of the captured dark matter annihilates outside the volume of a typical neutron star, producing a potentially observable signal for neutron stars in dark matter-dense environments. We have detailed this process in a model-independent manner, and estimated the rate of annihilation proceeding outside neutron stars as a function of the interstate mass splitting.

We have investigated the detection prospects of this annihilation signal by targeting the neutron star population in the Galactic Center, where the dark matter content is robustly expected to be high and neutron star-focused annihilation can dominate over halo annihilation. Specifically, we have computed the resulting γ-ray and neutrino signals produced from a variety of annihilation channels. Naturally, these predictions depend on the assumed dark matter and neutron star distribution profile. For a cuspy generalized NFW dark matter profile motivated by adiabatic contraction studies, and various neutron star distributions, we have placed constraints based on H.E.S.S. Galactic Center observations on the inelastic dark matter-nucleon cross-section. These constraints can reach down to $\sim 3 \times 10^{-46}$ cm^2 in the case of direct annihilation to photons, for dark matter masses ranging $10^2 - 10^5$ GeV. Our procedure for setting the H.E.S.S. bound required the γ-ray flux from dark matter

annihilation to exceed the total γ-ray flux from the Galactic Center; future analyses may improve on this method and find a stronger bound. We have also computed the sensitivity of future γ-ray and neutrino observatories to this signal. Depending on the annihilation channel, as well as the assumed dark matter and neutron star distributions, future neutrino and γ-ray telescopes will reach inelastic cross-sections as low as about $\sim 2 \times 10^{-47}$ cm^2.

This study demonstrates the use of neutron star populations in high dark matter density systems as a means of probing inelastic dark matter models across a mass range that spans $\sim$10 orders of magnitude. In this scenario, nuclear scattering in direct detection experiments is either kinematically forbidden or has a minuscule rate, potentially making these objects the only viable way of probing these models. Notably, this search can complement neutron star heating searches, which have been previously explored but crucially depend on the proximity of old neutron stars, require the allocation of significant infrared telescope observation time, and might be masked by other internal neutron star heating mechanisms.

Having established the prospects for detecting exterior annihilation of inelastic dark matter via high-energy messengers, we next shift our gaze much closer to home. In the next chapter, where we will focus on refining the local free-electron density map through pulsar parallaxes, a crucial step toward identifying the nearest neutron stars for infrared searches of dark-matter–induced heating.

3.7 Supplementary Material

3.7.1 Neutron Star Structure

For a static and spherically-symmetric neutron star, the spacetime interval is expressed as

$$ds^2 = g_{tt}(r)dt^2 + g_{rr}(r)dr^2 - r^2 d\Omega^2 \ , \tag{3.46}$$

where $d\Omega^2 = d\theta^2 + \sin^2\theta \, d\varphi^2$. To determine the neutron star density profile and the metric components in its interior, we numerically solve the TOV equation

$$\frac{dP}{dr} = -\frac{G\rho m}{r^2}\left(1+\frac{P}{\rho}\right)\left(1+\frac{4\pi P r^3}{m}\right)\left(1-\frac{2Gm}{r}\right)^{-1} \ , \tag{3.47}$$

$$\frac{dm}{dr} = 4\pi r^2 \rho \ , \tag{3.48}$$

$$\frac{d\Phi}{dr} = -\frac{1}{\rho}\frac{dP}{dr}\left(1+\frac{P}{\rho}\right)^{-1} \ . \tag{3.49}$$

Above, $P(r)$ is the pressure, $\rho(r)$ is the energy density, $m(r)$ is the enclosed gravitational mass within r, and $g_{tt}(r) = \exp(2\Phi(r))$. The remaining interior metric component is $g_{rr}(r) = -\left(1-2Gm(r)/r\right)^{-1}$. Outside the neutron star, the solution is matched to the Schwarzchild metric, *i.e.* $g_{tt}\left(r \geq R_{\rm NS}\right) = 1 - 2GM_{\rm NS}/r$ and $g_{rr}\left(r \geq R_{\rm NS}\right) = -g_{\rm tt}^{-1}(r)$. The above system is closed when an equation of state, *i.e.* a constitutive relation of the form $P = P(\rho)$, and the central energy density are specified. It can then be solved through standard numerical methods. For our chosen BsK-21 equation of state, fixing the central energy density to $\rho_c \simeq 7.85 \times 10^{15}$ g cm^{-3} yields our benchmark neutron star of mass $M_{\rm NS} \simeq 1.5 M_\odot$ and radius $R_{\rm NS} \simeq 12.55$ km.

3.7.2 Dark Matter Orbital Period and Velocity

We derive general relations used in the main text for the orbital period and the velocity of a dark matter particle. In what follows, we will assume the total energy of the particle remains fixed. We start from the Hamilton-Jacobi equation (see *e.g.* [203])

$$g^{\mu\nu}\frac{\partial S}{\partial x^{\mu}}\frac{\partial S}{\partial x^{\nu}} - m_{\chi}^{2} = 0 \ , \tag{3.50}$$

where the metric components $g^{\mu\nu} = g_{\mu\nu}^{-1}$ are determined from Eqs. (3.47)−(3.49) above, and $S(x)$ is the action evaluated along the physical trajectory (for abbreviation, $x = (t, r, \theta, \varphi)$). This equation is solved by the separation of conjugate variables associated with constants of motion. Using the fact that the orbits are contained within a plane, we fix $\theta = \pi/2$ without losing generality. The ansatz solution is expressed as

$$S(x) = \varepsilon\, t - M\, \varphi + S_{r}(r) + \text{const.} \ , \tag{3.51}$$

where ε and M are the dark matter particle's total energy and orbital angular momentum, respectively. This ansatz is introduced in Eq. (3.50). Isolating the derivative $S_r(r)$, one can integrate the action function up to an arbitrary constant fixed by the initial condition,

$$S_{r}(r) = \int \left[g_{rr}(r) \left(m_{\chi}^{2} + \frac{M^{2}}{r^{2}} - \frac{\varepsilon^{2}}{g_{tt}(r)} \right) \right]^{1/2} dr \ . \tag{3.52}$$

We numerically integrate the above using the metric components for our benchmark neutron star profile, *cf.* Sec. 3.7.1.

From Eq. (3.51), it is possible to compute the orbital period and velocity as a

function of the dark matter energy, which are required inputs to analyze how thermalization proceeds after capture. For a given ε and M, the orbital time between coordinates r and r_0 is given by [203]

$$t - t_0 = \frac{\partial S_r}{\partial \varepsilon} \ , \tag{3.53}$$

where $S_r(r)$ is integrated from r_0 to r. We compute the orbital period as a function of energy from this relation. To compute the velocity measured by a local observer, we use the relation between energy and the time component of the 4-velocity,

$$\varepsilon = m_\chi \, g_{tt}(r) \, \frac{dt}{ds} \ . \tag{3.54}$$

For a constant gravitational field, we may write $ds = \sqrt{g_{tt}(r) dt^2 - dz^2}$, where dz is the proper radial length measured by a local observer. Defining $v = dz/d\tau$, we have

$$\varepsilon = m_\chi \left(\frac{g_{tt}(r)}{1 - v^2} \right)^{1/2} \ . \tag{3.55}$$

Since we are assuming here that the energy ε is constant once the inelastic transition becomes suppressed, we have $(\varepsilon/m_\chi)^2 = \text{const.} = g_{tt}(r)/(1 - v^2)$. At a turning point $r = r_f$, the velocity vanishes, and thus we have the relation

$$g_{tt}(r_f) = \left(\frac{\varepsilon}{m_\chi} \right)^2 \tag{3.56}$$

between the turning point and the energy. Using this relation in Eq. (3.55) and solving for v, we have

$$v(r) = \left(1 - \frac{g_{tt}(r)}{g_{tt}(r_f)} \right)^{1/2} \ . \tag{3.57}$$

As a consistency check, note that in the limit $r_f \to \infty$, setting $r = R_{\rm NS}$ yields $v(R_{\rm NS}) = \sqrt{2GM_{\rm NS}/R_{\rm NS}}$, which corresponds to the usual escape velocity expression used throughout the literature.

3.7.3 Inelastic Dark Matter Profile

We now estimate the resulting inelastic dark matter profile around a neutron star using simple kinetic theory arguments. In what follows, we will assume no angular momentum for simplicity. Furthermore, we will only consider the dark matter population that has lost enough energy so that the inelastic transition becomes kinematically forbidden. These are conservative choices because particles with non-zero angular momentum will generally spend a greater time orbiting outside the object, and we are also neglecting a small but finite population of dark matter particles that are at any given time in an earlier stage of thermalization. So, our results underestimate the true dark matter density outside of the neutron star that contributes to the overall annihilation signal.

When the dark matter particles have lost enough energy, we assume elastic interactions are sufficiently suppressed that we may approximate the system as collisionless. In this regime, all the dark matter particles will be in approximately steady-state orbits, with randomly distributed phases and the same energy determined by the inelastic mass splitting. The occupation number of a phase space volume is invariant for any local Lorentz observer along the worldline of the dark matter particles [203]. Thus, a given dark matter particle in its rest frame sees a constant number density associated with the total number of particles with the same 3-momentum. Upon

boosting to the frame of a local observer in the neutron star, that number density receives a factor $\sqrt{1-v(r)^2}$, *cf.* Eq. (3.13). We then parameterize the number density as

$$n_\chi(r) = n_\chi^0 \left(1 - v(r)^2\right)^{1/2} \tag{3.58}$$

where n_χ^0 is a normalization constant which can be fixed through the condition

$$\int_0^{r_f} 4\pi r^2 n_\chi(r) dr = \begin{cases} C_\chi t_{\rm NS} \ , & t_{\rm NS} \ll t_{\rm eq} \\ \\ N_{\rm eq} \ , & t_{\rm NS} \gg t_{\rm eq} \end{cases} \tag{3.59}$$

Above, $t_{\rm NS}$ is the lifetime of the neutron star, which we assume to be $\mathcal{O} \sim$ Gyr, and $t_{\rm eq}$ is the timescale on which capture-annihilation equilibrium is reached, *cf.* Eq. (3.30).

Chapter 4

Seeking the Nearest Neutron Star For Thermal Dark Matter Studies

How close is the nearest neutron star to Earth? Answering this question accurately may have far-reaching implications for fundamental physics and astrophysics, since neutron stars (NSs) constitute some of their most sensitive laboratories [83, 204, 205]. For example, precise measurements of the masses and radii of nearby NSs would be essential to constrain the state equation of high-density matter [206], and their velocities would help pinpoint their kinematic age [207], all of which would sharpen our understanding of passive cooling of NSs [208–210]. Of particular interest to us in this regard are the late-stage reheating mechanisms of NSs, such as numerous heating mechanisms involving a hidden sector of particles [83], including dark matter and other proposed astrophysical effects [211]. For recent reviews of hidden sector and astrophysical mechanisms, see *e.g.* Ref. [83] and the Appendix of Ref. [140].

Of the $\sim 10^9$ neutron stars in the Galaxy, only $\sim 4 \times 10^3$ have been detected as radio pulsars ($\sim 0.0004\%$), which is a small fraction of the total population [212]. The closest known pulsar is estimated to be $110-130$ pc away [213, 214], whereas from

the number density of NSs in the solar vicinity, $n_\odot \simeq (1-5) \times 10^{-4}\text{pc}^{-3}$ (assuming 10^9 NSs in the Galaxy) [85, 215], we obtain a theoretical distance to the nearest NS of only $(3/4\pi n_\odot)^{1/3} \simeq 10$ pc. This calls for a careful scrutiny of the region around us. Of course, the spatial pulsar distribution in our galaxy has been a topic of interest for a few decades now. Thanks to the current generation of large-scale pulsar surveys [94, 216–222], we now have large samples of both regular ($\mathcal{O}(1)$ s period) and millisecond pulsars. Along with the ATNF pulsar catalogue [94], which is considered the standard, other databases such as the EPN database of pulsar profiles [222] and the Green Bank North Celestial Cap (GBNCC) pulsar survey [216–221], provide detailed accounts of discovered pulsars.

Pulsar distance estimates in these catalogues are often based on radio pulsar dispersion measures (DMs), which in turn rely on two prominent models that map the Galactic free-electron distribution: NE2001 [89] and YMW16 [92]. Combined with direct measurements of a pulsar's radio DMs, these can be used to estimate distances to pulsars in the Milky Way. These models have been well-calibrated to achieve remarkable precision on distance scales of kiloparsecs (kpc) and above with YMW16, a significant refinement of the earlier NE2001. Both models integrate an array of Galactic features, including spiral arms, thin and thick disks, and localized clumps of electron density, allowing for an accurate reconstruction of the interstellar medium (ISM) structure. As such, for pulsar timing arrays, studies of the interstellar medium, and efforts to probe Galactic structure, the YMW16 and NE2001 models prove indispensable for finding distances across vast galactic distances. However, both models have some drawbacks, especially when it comes to accurately predicting

distances to nearby pulsars, due to large uncertainties in estimates of the *local* free-electron density in the 1 kpc vicinity of the Sun. Upon close inspection of pulsars with distances given by radio parallaxes, these models appear not to account for severe overdensities and underdensities of electrons in this region. This is a point conceded by YMW16 in Ref. [92], where it is stated that this loss of accuracy is an unavoidable consequence of its inability to adequately model small-scale structure.

In this work, we formulate a new simplified free electron column density map as an aid to finding the closest pulsar. We calibrate this map using *parallax* measurements of pulsar distances within 1 kpc of Earth, as these measurements are generally known to be reliable. With our simplified map, we predict and list the distances of several promising pulsar candidates. Using this method, we find some candidate nearest NSs *already discovered in the sky* that may be only a few tens of parsecs away. If any of these candidate nearby NSs are confirmed by future parallax measurement, they may provide a valuable new target for testing NS properties, and especially late-stage heating. In the latter half of this chapter, we illustrate this utility by studying nearby NS sensitivity for a minimal mechanism arising from dark matter: kinetic heating of NSs [82], possibly augmented by self-annihilations in their interior. We will assume two benchmark temperatures resulting from dark kinetic heating: 2500 K and 10000 K, the latter of which is possible if dark matter is clumped in microhalos [114]. These are below the upper bound on the coldest NS observed thus far, about 30000 K [223], and may be measured by the James Webb Space Telescope (JWST), the Thirty Meter Telescope (TMT), or the Extremely Large Telescope (ELT). Using the Exposure Time Calculators available online[1] , we estimate the distances to reheated NSs that would be within the sensitivity of the future TMT and ELT, for

[1] www.tmt.org/etc/iris, www.eso.org/observing/etc

reasonable exposure times.

4.1 Existing electron density models

In pulsar astronomy, the DM is a key observable that quantifies the total column density of free electrons between the observer and a pulsar along the line of sight:

$$\mathrm{DM} = \int_0^L n_e(\ell)\, d\ell \ , \tag{4.1}$$

where L is the distance along the line of sight, and n_e is the electron number density [224]. The lower frequency waves of a radio pulse arrive later than the higher frequency waves due to dispersion by the ISM.

The delay in arrival times of waves with frequencies f_1 and f_2 is then given by

$$\Delta t \propto \mathrm{DM} \left(\frac{1}{f_1^2} - \frac{1}{f_2^2} \right) \ . \tag{4.2}$$

Using Δt measurements for various lines of sight and pulse frequencies, combined with distance estimates, the spatial distribution of free electrons in the galaxy may be modeled. This method has produced empirical electron density maps for the Milky Way, but since there may be small non-electron contributions to the DM, it has been recently advocated [90] that the directly measured quantity $\mathcal{D} \equiv \Delta t (f_1^{-2} - f_2^{-2})^{-1}$ be reported by astronomers instead of the DM inferred from Eq. (4.2).

Over the past decades, several models have been developed to create and refine these maps, the most notable of which we will now briefly describe.

4.1.1 NE2001

The NE2001 model [89], making use of measurements of pulsar DM and distances and radio-wave scattering, built upon and superseded the 1993 model of Taylor and Cordes (TC93) [91] for the Galactic distribution of free electrons.

The basic structure consists of three smooth components – thick disk, thin disk, and spiral arms –, the Galactic Center, the local ISM, clumps, and voids. The NE2001 model calculates the local electron density by blending contributions from different regions of the Galaxy, each with its own distinct properties. The model begins by considering the primary electron sources, the Galactic disk and the Galactic Center, which dominate the electron density. It then accounts for the influence of the ISM and further introduces corrections for voids—regions with low electron density—and denser clumps of electrons scattered throughout the Galaxy. By assigning weights to these components, the model ensures that the distribution reflects their varying levels of influence. This weighting allows for a more nuanced and accurate representation of the electron density, especially across diverse environments within the Milky Way.

4.1.2 YMW16

The YMW16 model [92] predicts the large-scale distribution of free electrons in the Galaxy, Large Magellanic Cloud (LMC), Small Magellanic Cloud (SMC), and the Intergalactic Medium (IGM). The Galactic part of this model follows the same basic structure as NE2001, with the addition of a four-armed spiral pattern along with a local arm, the location and form of the arms based on observations of > 1800 H-II regions across the Galaxy. This model is then fitted to 189 independent estimates of pulsar distances that make use of parallaxes, Galactic rotation kinematics of H-I

clouds with absorption features, and association with other celestial objects.

Key features in YMW16 (most of which were also part of NE2001) are: the Local Bubble, two regions of enhanced electron density on the periphery of the Local Bubble, the Gum Nebula, a region of enhanced electron density in the Carina arm, and a region of reduced electron density in the tangential periphery of Sagittarius. One major difference between NE2001 and YMW16 is the modeling of the large-scale distribution of interstellar scattering: NE2001 incorporates this effect, while YMW16 omits it. This is because numerous studies have demonstrated that interstellar scattering is often dominated by only a few regions, with significant electron density fluctuations along the path to a pulsar, making it complicated to model. Another salient difference is that YMW16 does not incorporate clumps and voids to rectify discrepant model distances to some pulsars, in order to avoid future discrepancies for pulsars that may yet be discovered close to their lines of sight.

DM pulsar distance estimates in the ATNF catalogue [94] use the YMW16 model as the default. However, other distance estimates can improve accuracy. For example, distances determined by association with another object, such as the LMC or a supernova remnant, and those based on measured annual parallax (with an uncertainty less than one-third of the parallax value) are generally more reliable than distances derived from DMs. For the Local Bubble, there is reason to believe that there is a non-linear relationship between the DMs and the distances (see Eq. (4.1)), since we expect inhomogeneities in the local ISM electron density [95].

4.1.3 Limitations of existing models

Both the leading electron density maps have some limitations. The NE2001 model has large errors in distance estimates within 1 kpc of Earth, as this model was initially designed with regard to the overall structure of the Galaxy as opposed to fine features of the local region around the Solar neighborhood. For instance, while the YMW16 model predicts a distance of 143 pc for pulsar J0536−7543 based on the DM, NE2001 places it at 826 pc. This discrepancy highlights the NE2001 model's broader focus on the large-scale Galactic structure, which can lead to substantial errors when estimating distances in the local region around Earth. Further discrepancies arise due to assumptions about local electron density variations that are ill-constrained due to the sparse pulsar DM observations available at the time of inception of this model. While the model incorporates several large-scale galactic features, it doesn't give an accurate representation for smaller-scale-scale structure, which significantly impacts DM interpretation for nearby pulsars.

The YMW16 model utilizes more recent observational data, including several parallax measurements for a more extensive pulsar database, but still falls short when it comes to accurately describing the local free electron density. This is due to the fact that while the model refines the large-scale features, this does not always translate to a higher precision for nearby pulsars, where small-scale variations are more pronounced. Both NE2001 and YMW16 contain simplifications that can introduce systematic errors for nearby pulsar distance estimates. These include assuming a smooth distribution of electrons and not accounting for small-scale clumpiness or voids in the ISM.

For more extended discussion comparing the predictions of the NE2001 and YMW16

over various distance scales, we refer the reader to [93].

4.2 A new local kiloparsec electron density map

4.2.1 The importance of parallax measurements

Pulsar distances are measured most robustly with parallax methods that use pulsar timing to localize their sky position [225,226] and/or very long baseline interferometry (VLBI) [227,228]. A significant discrepancy between the VLBI-derived distances and those estimated from DM measurements combined with the NE2001 and YMW16 models was noted for 57 pulsars [227]. As noted in Ref. [140], PSR J1057−5226 is estimated to be at 93 pc by the YMW16 model and listed as the closest pulsar in the ATNF catalogue, but is estimated to be 730 ± 150 pc away by the NE2001 model and 1530 pc away by the TC93 model [229]. Moreover, an analysis of the optical and X-ray spectrum [230] puts PSR J1057−5226 at 350±150 pc. To our knowledge, no parallax measurement of its distance has been undertaken.

Such discrepancies arise due to inherent limitations and systematics of the DM method. This is quantified in the YMW16 model [92] by the statement that it comes with a less-than-90% uncertainty on 95% of its distance estimates. Note that typical uncertainties in parallax distance estimates are 10%–20%, underscoring their importance for not only pulsar distances but also the ISM distribution. And as already noted, previous electron density models are unreliable on sub-kpc scales – and it is exactly in the local $\mathcal{O}$(kpc) region that parallax measurements work best. Accurate distances to neighboring pulsars are, we re-emphasize, crucial for various astrophysical studies such as that of dark matter interactions with NSs.

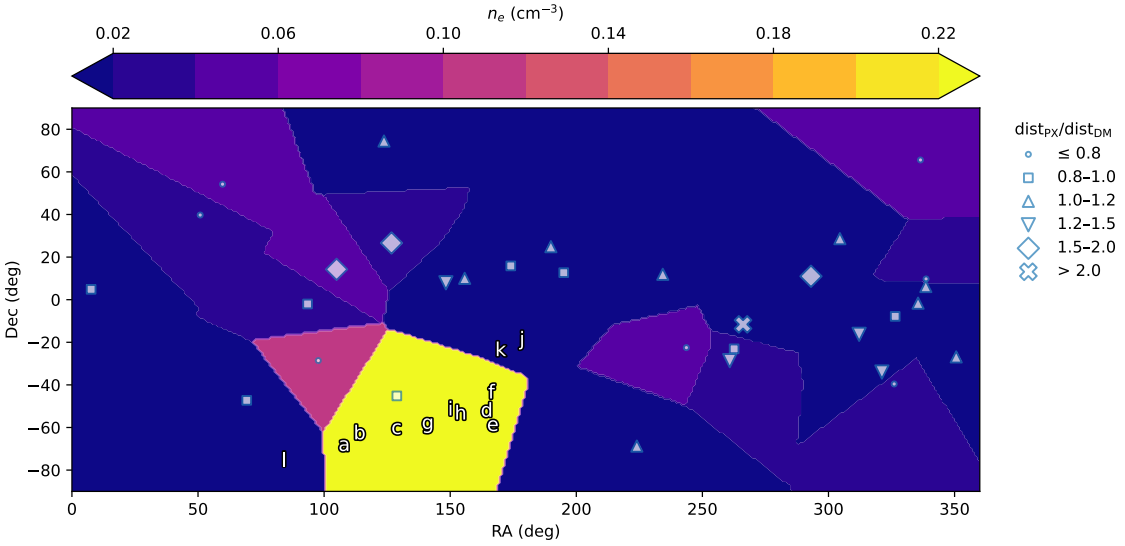

	PSR	DM (pc cm^{-3})	δDM (pc cm^{-3})	YMW dis (kpc)	Predicted dis (kpc)
a.	J0711−6830	18.4096	0.02	0.106	0.078 ± 0.004
b.	J0736−6304	19.4	-	0.104	0.082 ± 0.005
c.	J0834−60	20	6	0.095	0.084 ± 0.026
d.	J1057−5226	29.69	0.01	0.093	0.125 ± 0.007
e.	J1107−5907	40.75	0.02	0.115	0.172 ± 0.010
f.	J1105−4353	45	-	0.127	0.190 ± 0.011
g.	J0924−5814	57	-	0.107	0.242 ± 0.014
h.	J1016−5345	67	-	0.117	0.282 ± 0.018
i.	J1000−5149	72.8	0.30	0.127	0.307 ± 0.018
j.	J1154−19	10.69	0.05	0.121	0.822 ± 0.006
k.	J1120−24	9.81	0.13	0.098	0.825 ± 0.058
l.	J0536−7543	18.6	-	0.127	1.093 ± 0.007

Figure 4.1: A map of the free electron column density (blue-yellow colorbar) for the local region, created by fitting with a zeroth-order interpolation of parallax distances to all pulsars with reported parallaxes within 1 kpc. These pulsars are shown as white symbols, and have been classified by the ratio $\mathrm{dis_{PX}/dis_{YMW}}$. Possibly-nearby pulsars without published parallaxes are labeled "a"–"l" in the figure; their YMW-predicted distances and δDM (where available) are tabulated here alongside our new predicted distances from the revised n_e map. Some pulsar DM measurements reported without error bars are indicated with "-." Note that the region with the highest electron density (around the Vela pulsar J0835-4510) likely has larger systematic uncertainties, see the text and Figure 4.2 for discussion.

4.2.2 Parallax-fitted local electron distribution

To create an electron column density map for seeking the nearest pulsar, we start by compiling two datasets from the ATNF catalogue, one with pulsars for which a parallax (preferably radio parallax) is reported, and the other with all pulsars within 1 kpc of the Sun.[2] Then by using the parallax distances of and the DM along the line of sight to these sub-kpc pulsars, we reconstruct the electron number density from Eq. (4.1).

We compile pulsars with direct radio-parallax measurements within 1 kpc (Table 4.1). Our Gaussian-process reconstruction is anchored on this full set of 38 calibrators—including J0835–4510 (the Vela pulsar)—yielding the 1 kpc map shown in Fig. 4.1.

Gaussian Process Interpolation and Error Estimates

We constructed the local free–electron column density map using Gaussian process (GP) regression, trained on pulsars with both parallax distances and dispersion measures. For each calibrator pulsar, the electron density and its uncertainty are obtained from the parallax PX (in milliarcseconds) and dispersion measure DM (in pc cm^{-3}) as

$$n_e = \frac{DM \cdot PX}{1000}, \qquad \delta n_e = \frac{PX \cdot \delta DM + DM \cdot \delta PX}{1000}, \tag{4.3}$$

yielding n_e in cm^{-3}. These values form the GP training set.

[2] In principle catalogues of pulsars discovered by FAST [231–234] and CHIME [235, 236] may also contain specimens within 1 kpc, as derived from the NE2001 and YMW16 models [140]. These may also be included in our analysis but we only include ATNF catalogue pulsars as their properties have been reliably verified.

We employed a squared-exponential kernel,

$$k(\theta, \theta') = \sigma^2 \exp\left[-\frac{|\theta - \theta'|^2}{2\ell^2}\right], \tag{4.4}$$

with correlation length $\ell \sim 0.4$ rad ($\approx 23^\circ$), chosen to match the $\sim 17^\circ$ mean angular spacing of the parallax-calibrated pulsars. This setting smooths features below $\sim 20^\circ$ while retaining the larger-scale structure supported by the data. The GP posterior provides both the mean prediction $n_e(\alpha, \delta)$ and its predictive uncertainty $\delta n_e(\alpha, \delta)$ at any sky location.

For pulsars without parallax but with measured $DM \pm \delta DM$, distances are inferred as

$$d = \frac{\mathrm{DM}}{n_e(\alpha, \delta)}, \qquad \delta d = \sqrt{\left(\frac{\delta \mathrm{DM}}{n_e}\right)^2 + \left(\frac{\mathrm{DM}\, \delta n_e}{n_e^2}\right)^2}, \tag{4.5}$$

where both n_e and δn_e are taken from the GP map at the pulsar's coordinates. This approach naturally incorporates both measurement errors and modeling uncertainties into the distance estimates.

Our interpolation is carried out in projected angular coordinates (α, δ) rather than in full three-dimensional space. This avoids overfitting given the limited calibrator set but smooths over variations along the line of sight. Consequently, regions with steep gradients in n_e, such as the Vela region, carry larger predictive uncertainties. A full 3D GP reconstruction would require a denser set of parallax measurements. In addition, the uncertainties reported here do not account for the Lutz–Kelker bias [237], which arises from statistical effects in parallax measurements.

In the maps, we overlay the locations of all input pulsars (see Appendix 4.5.1). These sub-kpc pulsars overlap with the $\sim$189 used in the YMW16 model [92], though

YMW16 is primarily calibrated at multi-kpc scales. To illustrate deviations, we indicate the ratio of parallax to YMW16-based distances using different markers in the figure legend. Pulsars without parallax are labeled with white alphabetic markers, and their predicted distances are collected in the accompanying tables.

Finally, to assess the influence of J0835–4510 (Vela), which lies along a high-n_e sightline, we generated a variant of the 1 kpc map with this pulsar excluded from the calibration sample (Fig. 4.2).

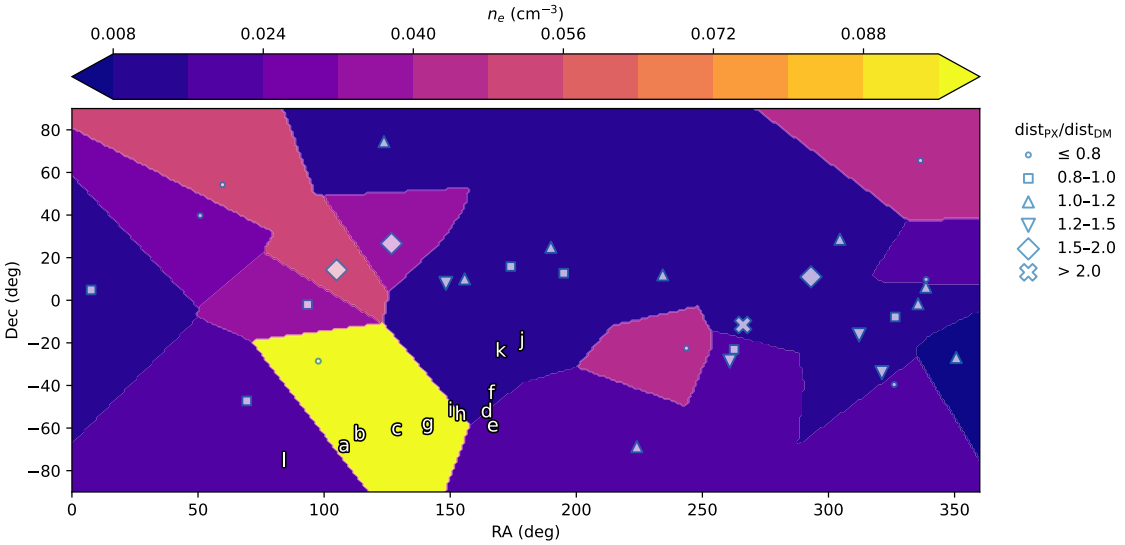

	PSR	DM (pc cm^{-3})	δDM (pc cm^{-3})	YMW dis (kpc)	Predicted dis (kpc)
a.	J0711−6830	18.4096	0.02	0.106	0.178 ± 0.024
b.	J0736−6304	19.4	-	0.104	0.187 ± 0.025
c.	J0834−60	20	6	0.095	0.193 ± 0.064
d.	J1057−5226	29.69	0.01	0.093	1.763 ± 0.202
e.	J1107−5907	40.75	0.02	0.115	2.151 ± 0.294
f.	J1105−4353	45	-	0.127	3.900 ± 0.144
g.	J0924−5814	57	-	0.107	0.554 ± 0.075
h.	J1016−5345	67	-	0.117	0.929 ± 0.123
i.	J1000−5149	72.8	0.30	0.127	0.703 ± 0.096
j.	J1154−19	10.69	0.05	0.121	0.822 ± 0.006
k.	J1120−24	9.81	0.13	0.098	0.825 ± 0.058
l.	J0536−7543	18.6	-	0.127	1.093 ± 0.007

Figure 4.2: Local electron column density map out to 1 kpc, constructed identically to Fig. 4.1, but with the Vela pulsar (J0835-4510) removed from the calibration set.

Several features are apparent in the first map i.e. Figure 4.1. First, we see that the predicted electron column density varies from $0.02 - 0.22$ cm^3. Notably, the prominent high-n_e patch in the southern hemisphere reflects the influence of the Vela pulsar (J0835–4510) sightline, which has a rather high DM. With the removal of the Vela pulsar shown in Figure 4.2, the resulting map has a predicted electron column density that varies instead from $0.02 - 0.1$ cm^3. Hence, we can conclude that in our fitted map, the Vela pulsar sightline substantially affects the DM-based distance estimates for pulsars in this region, and in particular, the pulsars without parallax labelled $a - i$. Removing the Vela pulsar (Figure 4.2) reduces the predicted electron column density in this region by a factor of $2 - 3$.

As one example, let us consider the case of PSR 0711–6830 (labelled *a.* in the map): we note that Vahdat et al. in [238] found an x-ray-based distance estimate of for this pulsar of 860 pc. However, by calibrating exclusively to 1kpc-distant parallax measurements, the Figure 4.1 map predicts $d = 78 \pm 5$ pc for PSR J0711–6830. On the other hand, we find that excluding the Vela pulsar (J0835–4510) in our 1 kpc reconstruction changes the inferred distance for PSR J0711-6830; the Figure 4.2 map predicts $d_{without\,Vela} = 178 \pm 24$ pc, highlighting the increased systematic uncertainty along the Vela pulsar sightline. As another point of reference, we note that there is a pulsar in this region, J0940-5428, with a relatively low x-ray luminosity [239], which may indicate a corresponding ∼kpc distance, which would favor the second (Vela pulsar absent). We flag these discrepancies and emphasize that future VLBI parallax observations are necessary to adjudicate between these different estimates, and better resolve the region around the Vela pulsar.

Altogether, our findings illustrated in Figure 4.1 and 4.2 discussed above, motivate

follow-on parallax measurements of low DM pulsars in the region of the Vela pulsar, to better determine the electron density in this region. These measurements would also facilitate future proposed thermal measurements for pulsars by ELT and TMT, detailed in Sec. 4.3.2.

In Appendix 4.5.2, we extend the reconstruction to 1.1 kpc and provide tables of all input pulsars (Appendix 4.5.1).

4.3 Prospects for observing dark matter-induced neutron star reheating

As mentioned in the Introduction, NSs may be heated in their late stage by a number of external and internal reheating mechanisms. These include such astrophysical effects [211, 240–253] as rotochemical heating, vortex creep heating, crust-cracking, and magnetic field decay, as well as those induced by a new particle sector [7,24,31,32, 34, 82, 83, 105, 109–111, 113, 117, 123, 131, 132, 168, 236, 254, 255, 255–269] such as dark matter capture, removal of nucleons from their Fermi seas leading to the so-called nucleon Auger effect, and baryon number-violating neutron decays.

Here we will take dark matter capture as a minimal example, giving rise to kinetic and annihilation heating, and work out the signal expectations at the forthcoming TMT and ELT. We do this to demonstrate a concrete physics case for redrawing the electron density map to the end of seeking the nearest pulsars.

4.3.1 Review of dark kinetic and annihilation heating

For a detailed description of dark matter-induced heating of NSs, see Ref. [83]. Here we review essential details. Dark matter particles may get captured in astrophysical objects(like NSs) if they scatter and fall into their gravitational potential. The total

mass rate of the dark matter going through a NS of mass M and radius R is

$$\begin{aligned} \dot{m}_\chi &= \pi b_{\rm max}^2 \rho_\chi v_\chi \ , \\ b_{\rm max} &= \left(\frac{2GMR}{v_\chi^2}\right)^{1/2} \left(1 - \frac{2GM}{R}\right)^{-1/2} = \gamma R \frac{v_{\rm esc}}{v_\chi} \ , \end{aligned} \tag{4.6}$$

where $b_{\rm max}$ is the maximum impact parameter, $v_{\rm esc} = \sqrt{2GM/R}$ is the escape speed at the NS surface, and ρ_χ and v_χ are respectively the ambient dark matter density and halo dark matter speed, which we take as 0.42 GeV cm^{-3} and 230 km s^{-1} , respectively [144].

The rate of kinetic energy deposition is then

$$\begin{aligned} \dot{E}_k &= \frac{\dot{m}_\chi}{m_\chi}(\gamma - 1) f \ , \\ f &= \min\left[1, \frac{\sigma_{\chi \rm T}}{\sigma_{\rm crit}}\right] \ , \end{aligned} \tag{4.7}$$

where f is the fraction of incident dark matter particles that capture, with $\sigma_{\chi \rm T}$ the cross section for scattering with some target (nucleon, lepton, etc.) and $\sigma_{\rm crit}$ the cross-section above which the NS becomes optically thick to the infalling dark matter. Absent Pauli-blocking and multiscatter effects, this is the NS's $\mathcal{O}(10^{-45})$ cm^{-2} geometric cross section.

NSs have internal temperatures of 10^{11} K when formed and cool down through neutrino and photon emission, the latter dominating after $\mathcal{O}(10^5)$ yr. Until about 10^7 yr, an insulating envelope keeps the internal temperature larger than the surface temperature, but beyond this timescale it becomes too thin and the two temperatures become equal, with a value $\leq \mathcal{O}(10^3)$ K. Under equilibrium between dark kinetic

heating and passive cooling,

$$\dot{E}_k = L_{\rm NS} = 4\pi\sigma_{\rm SB} R^2 T_s^4 \ , \tag{4.8}$$

where $\sigma_{\rm SB}$ is the Stefan-Boltzmann constant, and T_s is the NS surface blackbody temperature, and for a distant observer, $T_\infty = T_s/\gamma$. Potential NS reheating from astrophysical effects and ISM accretion is, in most cases, unlikely; see Ref. [83].

If the captured dark matter thermalizes with the NS rapidly enough [123, 270] and self-annihilates efficiently into particles that are trapped in the star, higher heating luminosities are attained. In all, accretion of dark matter that is homogeneously distributed in the halo would give rise to NS surface temperatures of at best around 2500 K near the solar vicinity. Capture of dark matter clumped in overdensities such as microhalos, particularly in models where the dark matter has self-interactions and could thus undergo Bondi accretion, could result in heating-induced NS temperatures of $\mathcal{O}(10^4)$ K [271]. Similar temperatures could be achieved in the presence of long-range interactions between the in-falling dark matter and the NS baryons [262]. Motivated by these considerations, we will use reheated NS temperatures of 2500 K, 6000 K, and 10000 K as benchmarks for our treatment of telescope sensitivities.

4.3.2 Measuring neutron star temperatures with TMT and ELT

The currently operational Near Infrared Camera (NIRCam) on the James Webb Space Telescope (JWST), along with the upcoming Multi-AO Imaging Camera for Deep Observations (MICADO) on the Extremely Large Telescope (ELT) and the future InfraRed Imaging Spectrograph (IRIS) on the Thirty Meter Telescope (TMT) can image in infrared to far-optical wavelengths. These correspond to peak blackbody

temperatures of $1300 - 4300$ K, making these imaging instruments suitable for detecting NS reheating. As tabulated in Ref. [140], with $10^5 - 10^6$ s of exposure, these instruments could detect $\mathcal{O}(10^3)$ K NSs that are within $\mathcal{O}(10)$ pc and $\mathcal{O}(10^4)$ K NSs within $\mathcal{O}(10^2 - 10^3)$ pc. Here, we carry out a similar calculation for the forthcoming ELT-MICADO and TMT-IRIS in order to make our study self-contained.

Assuming the NS to be a blackbody, the spectral flux density is given by

$$f_\nu = \pi \frac{2h\nu^3}{c^2} \frac{1}{\exp(h\nu/kT_\infty) - 1} \left(\frac{R\gamma}{d}\right)^2, \tag{4.9}$$

often re-expressed in terms of the AB magnitude,

$$m_{\rm AB} = -2.5 \log_{10} \left(\frac{f_\nu}{3631 \text{ Jy}}\right) , \tag{4.10}$$

where R and d are the radius and distance of the NS respectively, and the factor $R\gamma/d$ is the angle subtended by the NS at a distant observer. We have neglected extinction factors along the line of sight, which would introduce uncertainties of at worst 10%, comparable to or smaller than distance uncertainties; see Ref. [140] for a detailed discussion.

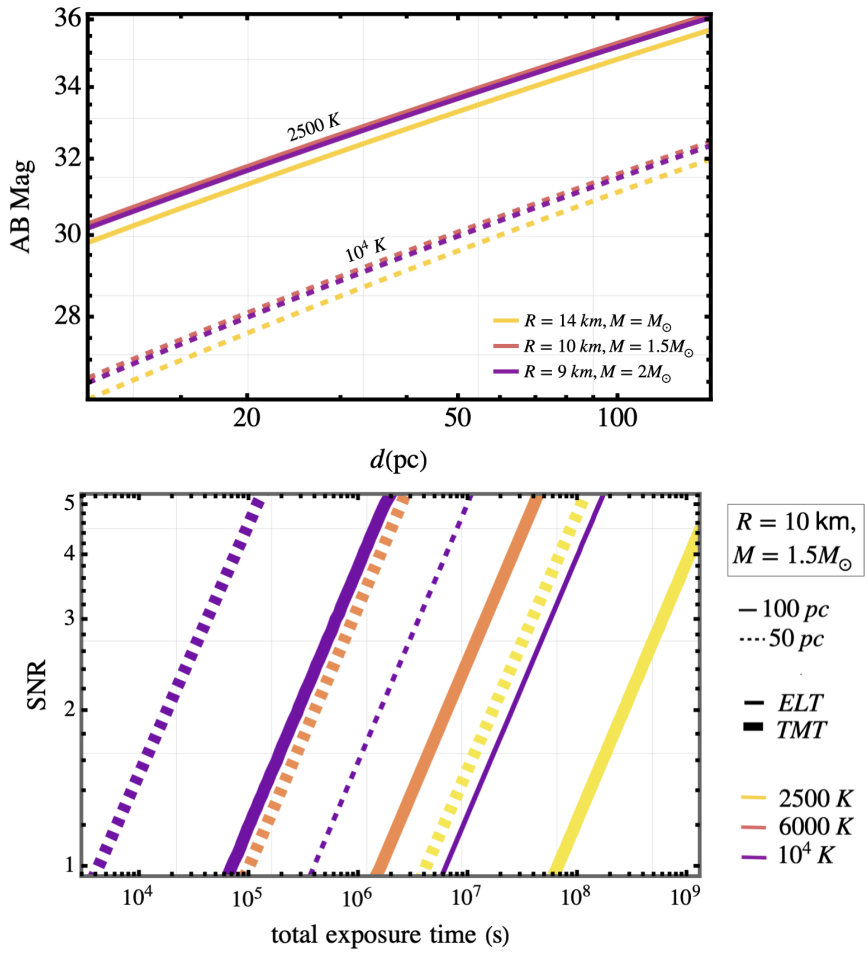

Figure 4.3: **Top:** AB magnitude derived for neutron stars heated maximally by kinetic and annihilation heating of dark matter to reach a temperature of 2500 K (solid lines) and 10^4 K (dashed lines) for different radius and mass profiles. **Bottom:** Predicted signal-to-noise ratio (SNR) from $1 \leq \mathrm{SNR} \leq 5$ versus total exposure time for neutron stars at 50 pc (dashed lines) and 100 pc (solid lines), computed with the MICADO ETC on ELT and the IRIS ETC on TMT. For ELT–MICADO we use the J band for $T_{\rm eff} = 2500\,\mathrm{K}$, B band for $T_{\rm eff} = 6000\,\mathrm{K}$, and U band for $T_{\rm eff} = 10^4\,\mathrm{K}$ to sample each blackbody peak. Note, that the J-band curve ($T_{\rm eff} = 2500\,\mathrm{K}$) lies at exposure times $\gtrsim 10^9\,\mathrm{s}$ and is therefore omitted from the plotted range. For TMT–IRIS, we use the Y-band filter—although it does not fall at the peak of the 6000 K or 10^4 K spectra, its wide bandwidth and high throughput still yield strong photon counts and competitive sensitivities. All calculations assume a canonical neutron-star radius of $R = 10\,\mathrm{km}$ and mass $M = 1.5\,M_\odot$. Note that exposures much longer than a few 10^7 s ($\sim$ yr) may be unrealistic, although this exposure time is comparable to prior ultra deep field observations [272].

Neglecting dithering and read-out pattern effects, the signal-to-noise ratio (SNR) in the background-dominated regime may be approximated as

$$\mathrm{SNR} = \frac{\Phi_{\mathrm{sig}} A_{\mathrm{SNR}} t_{\mathrm{exp}}}{\sqrt{(\Phi_{\mathrm{bg}} A_{\mathrm{SNR}} + \Gamma_{\mathrm{noise}}) t_{\mathrm{exp}}}}, \tag{4.11}$$

where Φ_{sig} and Φ_{bg} are signal and background fluxes, A_{SNR} is the SNR reference area in the detector, and Γ_{noise} is the non-sky noise rate. Thus, we expect $t_{\mathrm{exp}} \propto (\mathrm{SNR})^2$, and using this in Eq. (4.9), we have the scaling $t_{\mathrm{exp}} \propto d^4$. In the left panel of Fig. 4.3 we plot the AB magnitudes as a function of neutron-star distance for surface temperatures of 2500 K (solid lines) and 10000 K (dashed lines), over a range of mass–radius configurations. As expected from Eqs. (4.9) and (4.10), $m_{\mathrm{AB}} \propto \log d$, and more massive or larger stars appear brighter. In the right panel we plot the signal–to–noise ratio versus total exposure time for neutron stars at fiducial distances of 50 pc and 100 pc. For ELT–MICADO, we display only the $T = 6000\,\mathrm{K}$ (B-band) and $T = 10^4\,\mathrm{K}$ (U-band) curves, since at J-band the required exposure times exceed $10^9\,\mathrm{s}$—well beyond practical limits. For TMT–IRIS, we show all three temperature benchmarks ($T = 2500\,\mathrm{K}$, $6000\,\mathrm{K}$, and $10^4\,\mathrm{K}$) using the Y-band filter. Although Y-band does not coincide exactly with the spectral peaks of the higher-temperature cases, its broad passband and high throughput still yield robust SNR estimates. This choice provides a conservative, proof-of-concept sensitivity in the absence of B or U filters in the current TMT–IRIS ETC. For the ELT, we set the source geometry to be a point source with the source spectral type corresponding to the temperature profile being considered, with a S/N reference area of 1×1 pixels at the Paranal observation site at 2635 m, with a telescope diameter of 39 m, and we use the default background model. Furthermore, we use typical values for air-mass of 1.50, pixel scale

of 50 mas/pixel and seeing limited (FWHM= 0".8) adaptive optics mode. Similarly, for TMT, we set the source geometry to be a point source, at a zenith angle of 0 in good weather conditions, under the Imager mode configuration. In Fig. 4.3, we see the scaling SNR $\propto \sqrt{t_{\rm exp}} \propto d^2$. We also find the results consistent with Ref. [140].

Altogether, if the closest pulsar turns out to be no closer than 100 pc, the proposed observations laid out in Figure 4.3 will be challenging and require hundreds of hours of observation time. This proposal can be compared to the Hubble telescope campaign that placed a bound on the temperature of J2144–3933 of 4×10^4 K [223].

4.4 Conclusion

The aim of this study is to initiate a robust search for neutron stars nearest to Earth. A close enough NS would be a target for observing, among other things, novel late-time reheating mechanisms, including those from the capture of dark matter. To this end, we have attempted to refine the electron column density map in the solar vicinity, in turn improving the accuracy of dispersion measure-driven distance estimates for pulsars.

In particular, using parallax measurements of pulsar distances, we constructed a simplified electron column density map. This revised map allowed us to pinpoint promising nearby pulsar candidates that are ideal for follow-up parallax observations, as summarized in the table in Figure 4.1. We have discussed how, especially in the region of the Vela pulsar (Figure 4.2 shows the map generated without this pulsar), further pulsar distance measurements are necessary to overcome systematic uncertainties in the electron column density.

We believe our map may offer a more accurate depiction of pulsar locations within

the 1 kpc vicinity than the earlier NE2001 and YMW16 models, which had focused on large-scale galactic DMs, and included a template fit to assumed locations of electron over-densities and under-densities. In contrast, by only concentrating on the local kpc, we provide a new estimate of the free electron column density. Looking forward, more accurate estimates of distances to nearby NSs, such as those undertaken in this study, are an essential step to begin fathoming some longstanding puzzles of fundamental physics.

So far, in this thesis, we have discussed the dark matter-NS interactions and possible observables for those interactions in the solar neighborhood (in this chapter) and the galactic center (in the previous chapter). In the next chapter, we turn our sights to observables of dark matter-NS interactions at extragalactic scales.

4.5 Supplementary Material

4.5.1 Pulsar properties

In this section, we collect details of pulsars used in this work. In Table 4.1 are the pulsars used to construct our electron column density map in Fig. 4.1 and Fig. 4.4.

Table 4.1: Pulsars used to construct our local electron column density map in Fig. 4.1(and Fig. 4.4), along with their reported parallax, equatorial co-ordinate positions, dispersion measure, parallax distance, and YMW-based distance.

PSR	**PX** (mas)	**RAJD** (deg)	**DECJD** deg)	**DM** (cm^{-3} pc)	**dis**$_{PX}$ (kpc)	**dis**$_{YMW}$ (kpc)
J0030+0451	2.910 ± 0.180	7.61	4.86	4.33294 ± 0.00011	0.344	0.345

Continued on next page

Table 4.1 – continued from previous page

PSR	PX (mas)	RAJD (deg)	DECJD deg)	DM (cm^{-3} pc)	dis_{PX} (kpc)	dis_{YMW} (kpc)
J0034-0721	0.930 ± 0.080	8.54	–7.36	10.92200 ± 0.00600	1.075	0.996
J0323+3944	1.051 ± 0.040	50.86	39.75	26.18975 ± 0.00093	0.951	1.197
J0358+5413	0.910 ± 0.160	59.72	54.22	57.14200 ± 0.00030	1.099	1.594
J0437-4715	6.430 ± 0.040	69.32	–47.25	2.64476 ± 0.00007	0.156	0.156
J0613-0200	1.010 ± 0.090	93.43	–2.01	38.77500 ± 0.00050	0.990	1.024
J0630-2834	3.009 ± 0.409	97.71	–28.58	34.42500 ± 0.00100	0.332	2.069
J0659+1414	3.470 ± 0.360	1 04.95	14.24	13.94000 ± 0.09000	0.288	0.159
J0737-3039A/B	0.870 ± 0.140	114.46	-30.66	48.91600 ± 0.00200	1.149	1.105
J0814+7429	2.310 ± 0.040	123.75	74.48	5.75066 ± 0.00048	0.433	0.368
J0826+2637	2.010 ± 0.013	126.71	26.62	19.47633 ± 0.00018	0.498	0.314
J0835-4510	3.500 ± 0.200	128.84	-45.18	67.77100 ± 0.00900	0.286	0.280
J0953+0755	3.820 ± 0.070	148.29	7.93	2.96927 ± 0.00008	0.262	0.187
J1022+1001	1.160 ± 0.080	155.74	10.03	10.25500 ± 0.00080	0.862	0.834
J1024-0719	0.970 ± 0.130	156.16	–7.32	6.48640 ± 0.00020	1.031	0.382
J1136+1551	2.687 ± 0.018	174.01	15.85	4.84066 ± 0.00034	0.372	0.414
J1239+2453	1.160 ± 0.080	189.92	24.90	9.25159 ± 0.00053	0.862	0.827
J1300+1240	1.410 ± 0.080	195.01	12.68	10.16550 ± 0.00003	0.709	0.877

Continued on next page

Table 4.1 – continued from previous page

PSR	PX (mas)	RAJD (deg)	DECJD deg)	DM (cm^{-3} pc)	dis_{PX} (kpc)	dis_{YMW} (kpc)
J1321+8323	0.968 ± 0.140	200.44	83.39	13.31624 ± 0.00076	1.033	0.977
J1456-6843	2.200 ± 0.300	224.00	–68.73	8.61300 ± 0.00400	0.455	0.436
J1537+1155	1.070 ± 0.090	234.29	11.93	11.61944 ± 0.00002	0.935	0.877
J1607-0032	0.934 ± 0.047	241.80	–0.54	10.68230 ± 0.00010	1.071	0.680
J1614-2230	1.300 ± 0.200	243.65	–22.51	34.48500 ± 0.00030	0.769	1.394
J1723-2837	1.077 ± 0.054	260.85	–28.63	19.68800 ± 0.01300	0.929	0.720
J1730-2304	2.300 ± 0.200	262.59	–23.08	9.62570 ± 0.00050	0.435	0.512
J1744-1134	2.610 ± 0.090	266.12	–11.58	3.13849 ± 0.00012	0.383	0.148
J1932+1059	2.770 ± 0.070	293.06	10.99	3.18321 ± 0.00016	0.361	0.229
J2018+2839	1.030 ± 0.100	304.52	28.67	14.19770 ± 0.00060	0.971	0.959
J2048-1616	1.050 ± 0.030	312.15	–16.28	11.45600 ± 0.00500	0.952	0.775
J2124-3358	2.300 ± 0.200	321.18	–33.98	4.59540 ± 0.00030	0.435	0.360
J2144-3933	6.051 ± 0.560	326.05	–39.57	3.35000 ± 0.01000	0.165	0.289
J2145-0750	1.600 ± 0.300	326.46	–7.84	9.00080 ± 0.00130	0.625	0.693
J2222-0137	3.723 ± 0.014	335.52	–1.62	3.28260 ± 0.00020	0.269	0.267
J2225+6535	1.203 ± 0.204	336.47	65.59	36.44362 ± 0.00051	0.831	1.881
J2234+0611	1.050 ± 0.040	338.60	6.19	10.76700 ± 0.00020	0.952	0.854

Continued on next page

Table 4.1 – continued from previous page

PSR	**PX** (mas)	**RAJD** (deg)	**DECJD** deg)	**DM** (cm^{-3} pc)	**dis$_{PX}$** (kpc)	**dis$_{YMW}$** (kpc)
J2234+0944	1.300 ± 0.400	338.70	9.74	17.83230 ± 0.00020	0.769	1.587
J2241-5236	0.960 ± 0.040	340.43	–52.61	11.41126 ± 0.00003	1.042	0.963
J2313+4253	0.930 ± 0.070	348.29	42.89	17.27693 ± 0.00033	1.075	1.108
J2322-2650	1.300 ± 0.200	350.64	–26.85	6.14906 ± 0.00013	0.769	0.760

4.5.2 Modified electron density map in galactocentric representation

In this section, we re-create Fig. 4.1, with the region of interest now extended to 1.1 kpc. Here we see that extending the dataset to include pulsars with parallax out to 1.1 kpc does not substantially change the electron column density map.

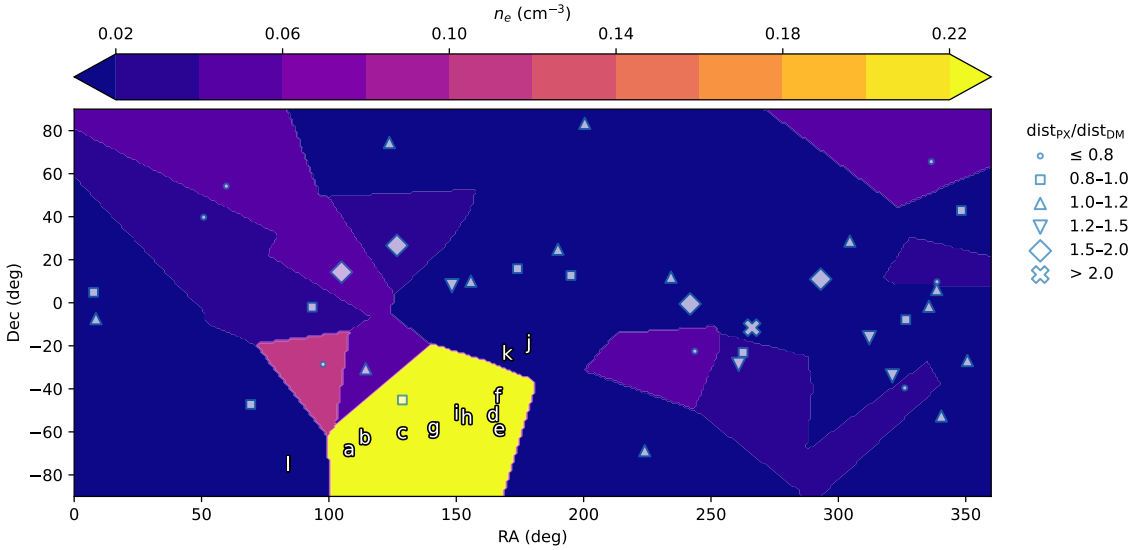

Figure 4.4: Map of the free electron column density (blue to yellow color bar) for the extended region of 1.1 kpc, created by fitting with a zeroth-order interpolation of parallax distances to all pulsars with reported parallax measurements that are within 1.1 kpc of Earth. These pulsars are displayed as white symbols, and have been classified according to the ratio of their distance estimates from parallax ($dis_{\rm PX}$) and from the YMW16 model ($dis_{\rm YMW}$). Possibly nearby pulsars that do not yet have parallax measurements made on them are labeled "a"–"l" in the figure; their YMW16 predicted distances and δDM (where available) are listed in Table 4.2.

	PSR	DM (pc cm^{-3})	δDM (pc cm^{-3})	$dis_{\rm YMW}$ (kpc)	Predicted distance (kpc)
a.	J0711−6830	18.4096	0.02	0.106	0.078 ± 0.004
b.	J0736−6304	19.4	—	0.104	0.082 ± 0.005
c.	J0834−60	20	6	0.095	0.084 ± 0.026
d.	J1057−5226	29.69	0.01	0.093	0.125 ± 0.007
e.	J1107−5907	40.75	0.02	0.115	0.172 ± 0.010
f.	J1105−4353	45	—	0.127	0.190 ± 0.011
g.	J0924−5814	57	—	0.107	0.242 ± 0.014
h.	J1016−5345	67	—	0.117	0.282 ± 0.018
i.	J1000−5149	72.8	0.30	0.127	0.307 ± 0.018

Continued on next page

Table 4.2 (continued): Distances for possibly nearby pulsars.

	PSR	DM (pc cm^{-3})	δDM (pc cm^{-3})	$dis_{\rm YMW}$ (kpc)	Predicted distance (kpc)
j.	J1154−1918	10.69	0.05	0.121	0.822 ± 0.006
k.	J1120−2410	9.81	0.13	0.098	0.825 ± 0.058
l.	J0536−7543	18.6	—	0.127	1.093 ± 0.007

Table 4.2: Distances for possibly nearby pulsars without measured parallax, labeled "a"−"l" in Fig. 4.4. YMW16 distances ($dis_{\rm YMW}$) and dispersion measures (DM) are compared to our newly predicted distances from the revised $n_e(r)$ map. The column δDM gives the difference between the measured DM and the DM implied by $dis_{\rm YMW}$.

Finally, in Fig. 4.5, we re-display pulsar positions from Figs. 4.1 & 4.4 in galactocentric right-handed rectangular coordinates. Here, the X axis is directed toward the Galactic Center, the Y axis spans longitude, and the Z axis spans latitude.

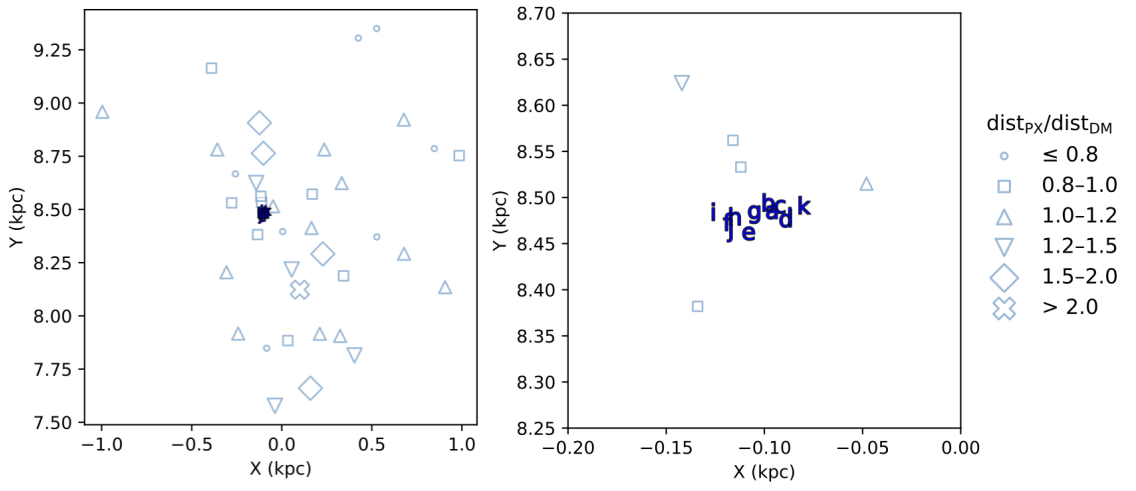

(a) Side View (X-Y)

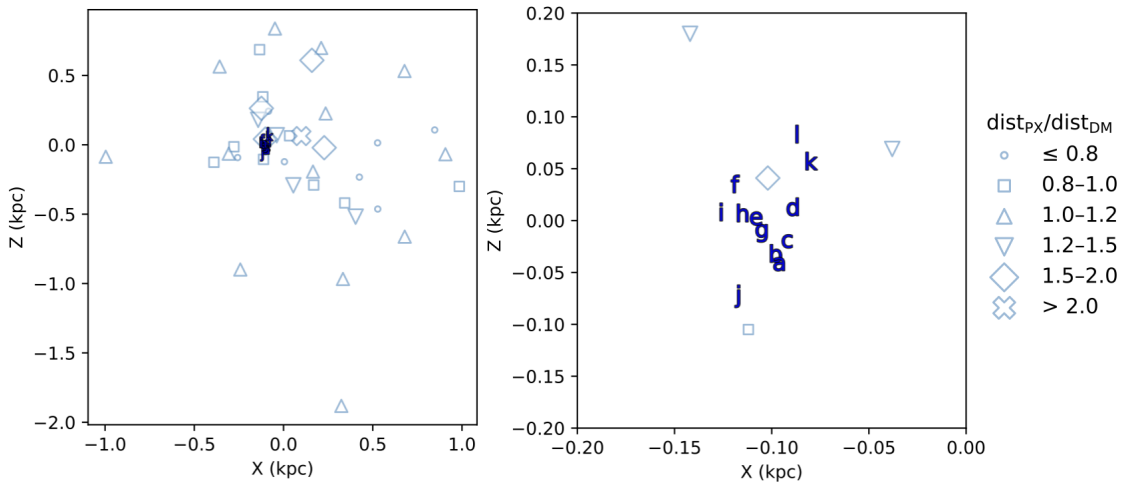

(b) Top View(X-Z)

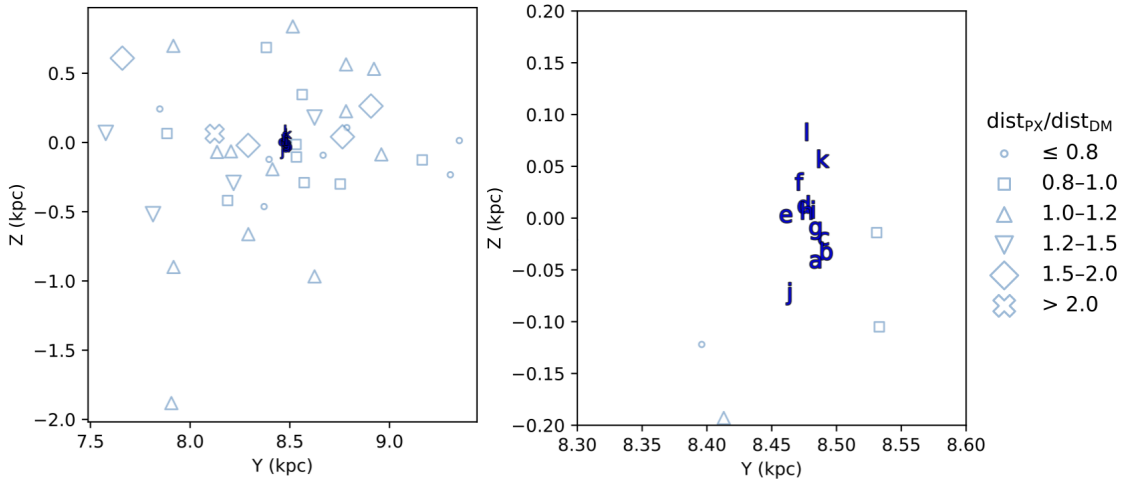

(c) Front View(Y-Z)

Figure 4.5: Projected pulsar positions in Galactocentric rectangular coordinates. The left column shows the **(a)** side–view (X–Y), **(b)** top–view (X–Z), and **(c)** front–view (Y–Z) slices. Pulsars with reported parallax distances are classified according to the ratio of their distance estimates from parallax and from the YMW16 model (shown by white symbols), $\mathrm{dist_{PX}/dist_{DM}}$, and nearby candidates without measured parallaxes are marked by red labels "a"–"l." The right-hand panels are zoomed in on the same regions to highlight those labeled sources.

Chapter 5

FRB Signatures of Dark Matter-Induced NS Implosions in Extragalactic Hosts

The potential for dark matter accumulation to trigger gravitational collapse of NSs into solar-mass black holes has been recognized since the late 1980s [80]. Subsequent research [7,34,82,83,105,129,131,132,167,168,270,273] has studied how dark-matter transiting through a NS may undergo single or multiple scattering events with stellar constituents, predominantly nucleons.

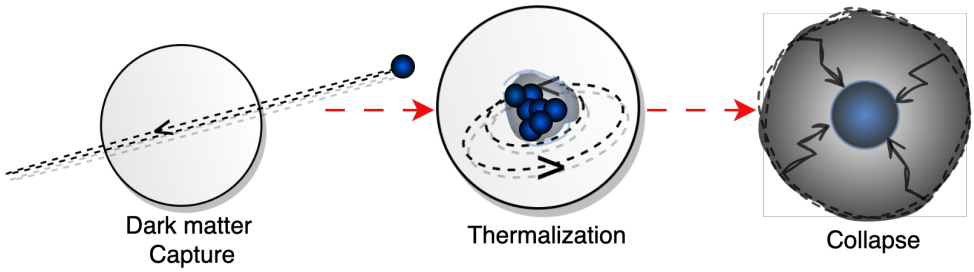

Figure 5.1: Dark-matter can scatter with and subsequently get captured by a NS. Upon capture, the dark-matter begins to accumulate as it spirals towards the center of the NS till it reaches M_{crit}, after which it can collapse into a small BH.

As shown in Fig. 5.1, upon scattering (once or multiple times for heavier dark-matter masses, see Ref. [167]), the dark-matter particles subsequently lose their kinetic energy from repeated scattering with the NS medium, and proceed to sink to the center of the NS, forming a compact core that can collapse into a small black hole. In order to become a black hole, the accumulated, collapsed dark matter in the NS must reach sufficient mass to overcome degeneracy pressure. Once the mass of this dark-matter blob exceeds this *critical mass*, it can form a small ($\lesssim 10^{-10}\mathrm{M}_{\odot}$) black hole that subsequently accumulates the host NS [11, 33, 80, 81].

Similar NS collapse events are possible through the capture of primordial black holes (PBHs) that are hypothesized to have formed via early–universe density fluctuations during the radiation domination era [21, 124]. As illustrated in Fig. 5.2, a PBH traversing a NS can lose kinetic energy via a combination of dynamical friction, accretion of nuclear matter, and gravitational wave emission, and become gravitationally bound to the NS. Once captured, the PBH spirals inward, settling at the stellar core, where it begins Bondi accretion of the surrounding stellar material. For PBHs masses spanning 10^{41}–10^{50} GeV (or around $\sim 10^{-13} - 10^{-4} M_{\odot}$), it has been hypothesized that this capture and accretion mechanism can lead to complete destruction of the host NS on timescales shorter than their typical lifespans [28].

Refs. [11] explored the possibility that these NS implosions could be the reason behind the "missing pulsar problem" [274]. In particular, Ref. [11] identified some dark-matter models that would be capable of causing such collapses and defined regions of parameter space where dark-matter accumulation can deplete the pulsar population in the galactic center. Later, it was proposed that during the neutron star implosion event, the rapid expulsion of the NS magnetosphere during such a collapse

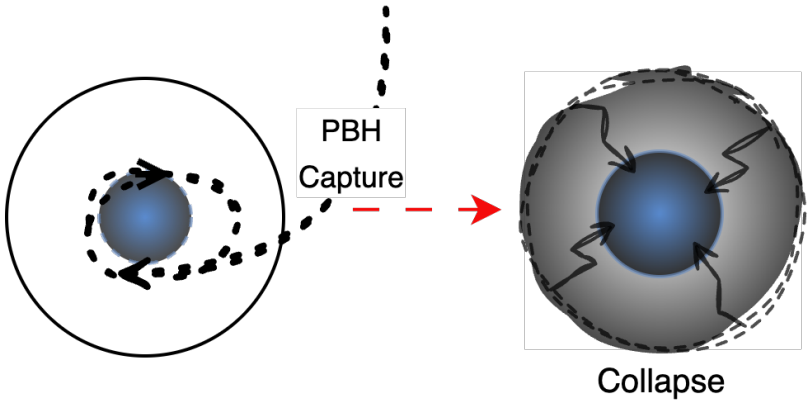

Figure 5.2: A PBH passing through a NS can lose enough energy through interactions with the dense stellar medium to become gravitationally bound to the star. Once captured, the PBH would sink to the core of the NS and completely consume it from within.

could generate a very short yet extremely bright radio flash matching what is expected for a Fast Radio Bursts (FRBs) [12]. Discovered in 2007 [97], FRBs are millisecond-long, high luminosity radio pulses of extragalactic origin, commonly associated with NSs. Ref. [12] detailed how the short burst durations, large luminosities, and high brightness temperatures associated with FRBs could be caused by an imploding NS. We visit this idea in more detail in this chapter by extending the dark-matter-induced NS collapse predictions developed in [33], which presented galactocentric NS implosion rates for a Milky Way-like galaxy. Here we extend that analysis to elliptical and dwarf galaxies, and in addition develop a framework to predict the dispersion measures (DMs)[1] expected for NS implosion FRBs in extragalactic hosts.

For clarity, Table 5.1 compiles the benchmark dark matter scenarios that are used in this work, together with their key parameters and the observational signatures

[1] **Attention**: The abbreviation **DM** is used solely for **dispersion measure** (DM does not stand for dark matter) in this chapter, and throughout this thesis.

Table 5.1: Dark matter models and scenarios used in this work, with key parameters and their associated astrophysical observables.

Scenario	Motivation	Key Parameters	Observable Signature
ADM1	Asymmetric dark matter core collapse	$t_c\rho_\chi/v_\chi = 3$ Gyr GeV cm^{-3} / (300 km/s)	NS implosions $\rightarrow$ FRB DMs
ADM2	Asymmetric dark matter with slower collapse	$t_c\rho_\chi/v_\chi = 15$ Gyr GeV cm^{-3} / (300 km/s)	NS implosions $\rightarrow$ FRB DMs
PBHmax	Maximal primordial black hole capture	$10^{-13} \lesssim m_{\rm pbh} \lesssim 10^{-10} M_\odot$	Rapid NS implosions $\rightarrow$ FRB DMs

that will be analyzed in the subsequent sections. Together, these scenarios illustrate the breadth of dark matter candidates that NSs can probe, through catastrophic implosions triggered by asymmetric dark matter or primordial black holes.

5.1 NS Implosions Induced by Dark Matter

Once a NS embedded in a local dark matter density ρ_x has captured enough transiting dark matter flux as described briefly in Sec. 2.6.1. As described before, the maximum dark matter accumulation rate is given by

$$\begin{aligned}\dot{m}_\chi &\approx \pi\,\rho_\chi\,\frac{2GM\,R}{v_\chi}\left(1-\tfrac{2GM}{R}\right)^{-1}\\ &\simeq 7\times10^{25}\,\frac{\rm GeV}{\rm s}\,\left(\frac{\rho_\chi}{\rm GeV/cm^3}\right)\left(\frac{300\,{\rm km/s}}{v_\chi}\right),\end{aligned}\tag{5.1}$$

where M and R are the NS's mass and radius, and $v_\chi(r)$ is the velocity dispersion at galactocentric radius r.

In this work, we focus on asymmetric dark matter (ADM), motivated by the observed similarity between the cosmic baryon density and the dark matter density,

$\Omega_{\rm DM} \approx 5, \Omega_b$. This coincidence suggests that the mechanisms responsible for generating the baryon asymmetry and for setting the dark matter relic abundance may share a common origin. In ADM models, a particle–antiparticle asymmetry is established in the dark sector, analogous to the baryon asymmetry, so that the symmetric component annihilates away, leaving only the asymmetric population. This framework naturally favors dark matter masses in the GeV to tens of GeV range and strongly suppresses present-day indirect detection signals. Nevertheless, ADM can accumulate efficiently in compact objects such as neutron stars, where it may eventually reach a critical density and collapse into a black hole, destroying the host star. Such implosions have been proposed as potential astrophysical signatures of ADM and as candidate progenitors of fast radio bursts.

For heavy asymmetric dark matter, the critical mass of dark matter required to form a small black hole is $M^{\rm f}_{\rm crit} \sim \frac{m^3_{\rm pl}}{m^2_\chi}$ for dark fermions with mass $m_{\rm x}$ [125], and $M^{\rm b}_{\rm crit} \sim 0.12\sqrt{\lambda}\frac{m^3_{\rm pl}}{m^2_\chi}$ for dark scalars with self-interaction potential $V(\phi) = \lambda|\phi|^4$ [125, 275]. In these models, the NS implodes shortly after accumulating a critical mass of dark matter at time $t_{\rm c} \simeq M_{\rm crit}/\dot{m}_\chi$, where this expression assumes all dark matter passing through the NS is captured [33].

A number of follow-on studies have determined how NS implosion can be affected by a number of factors [108], including the NS composition, particulars of dark matter's interactions with nucleons, and even scattering with pasta phases in the NS crust [168]. However, it is possible to study NSs imploded by dark matter without committing to a particular set of assumptions about the interior composition of NSs

and dark matter interaction models. Since the collapse time

$$t_c \simeq \frac{M_{\rm crit}}{\dot{m}_\chi} \propto \frac{v_\chi}{\rho_\chi},$$

the combination

$$t_c \frac{\rho_\chi}{v_\chi} = \text{constant} \times \left[\text{Gyr}\,\frac{\text{GeV/cm}^3}{300\,\text{km/s}}\right] \tag{5.2}$$

is independent of r. Following a convention begun in [33] we will refer to (5.2) as a normalized implosion time, which quantifies the integrated time in a fixed dark matter background for NSs to implode. Hereafter, we will normalize this to a typical dark matter density (GeV/cm^3) and velocity dispersion (300 km/s). Then the value of $t_c\rho_\chi/v_\chi$ for a specific dark matter model can be determined by calculating the time for dark matter with local density ρ_χ and relative velocity v_χ to implode a NS. In this work, we focus on two benchmark values:

$$\begin{aligned} \text{ADM 1 where } t_c\rho_\chi/v_\chi &= 3.0\ \text{Gyr}\cdot\text{GeV/cm}^3, \\ \text{ADM 2 where } t_c\rho_\chi/v_\chi &= 15.0\ \text{Gyr}\cdot\text{GeV/cm}^3 \end{aligned} \tag{5.3}$$

which we denote "ADM1" and "ADM2" respectively [33]. In the ADM1 case, a considerably smaller amount of time is needed to trigger collapse, whereas ADM2 represents a more conservative capture efficiency, requiring five times more integrated dark-matter flux before collapse. ADM1 has a normalized capture rate that is about a factor of two away from a value constrained by pulsar J1738+0333 [126]. These

two benchmarks then translate directly into different predicted neutron-star implosion (and FRB) rates as a function of galactic dark-matter properties, as shown in Figs. 5.3, 5.4 & 5.5.

5.1.1 Neutron star implosions from primordial black holes

As illustrated in Fig. 5.2, a PBH of mass $m_{\rm BH}$ passing through a NS of mass M and radius R, loses energy by dynamical friction and gravitational focusing [21, 28]. The energy lost per crossing is

$$E_{loss} \;=\; \frac{4\,G^2\,M\,m_{\rm BH}^2}{R^2}\,\left\langle\frac{\ln\,\Lambda}{2GM/R}\right\rangle\,, \tag{5.4}$$

where the Coulomb logarithm $\langle\ln\Lambda/(2GM/R)\rangle \sim 14.7$ for a typical neutron star density profile. This dimensionless factor encapsulates the degree of gravitational focusing experienced by dark matter particles as they cross the NS's potential well. A PBH with initial kinetic energy $K = \frac{1}{2}\,m_{\rm BH}\,v^2$ is captured if $E_{loss} \gtrsim K$. If the probability of getting captured in a single crossing is

$$P_{\rm cap}(v) \;=\; 1-\exp\Big[-\frac{3\,E_{loss}}{m_{\rm BH}\,v^2}\Big]\,, \tag{5.5}$$

then the capture rate of PBHs by a NS takes the form [28]

$$C_{\rm pbh} = \sqrt{6\pi}\frac{\rho_{\rm pbh}}{m_{\rm pbh}}\left(\frac{2GMR}{v_\chi}\right)\frac{1-{\rm Exp}\left[-\frac{3E_{\rm loss}}{m_{\rm pbh}v_\chi^2}\right]}{1-\frac{2GM}{R}}, \tag{5.6}$$

where, again, for a typical NS profile $\langle\ln\Lambda/(2GM/R)\rangle \sim 14.7$. Ref. [28] finds that $C_{\rm pbh}$ peaks for PBH masses spanning $\sim 10^{44}$–10^{47} GeV (or $\sim 10^{-13} - 10^{-10} M_\odot$).

If we assume $m_{\rm pbh} \simeq 10^{45}$ GeV and $\rho_{\rm pbh} = \rho_\chi$ (*i.e.* PBHs constitute *all* of the dark matter), the resulting NS implosion rate is far too small to be observable in upcoming astronomical surveys, however, we will include calculations of this rate alongside the ADM1 and ADM2 models for comparison.

5.2 NS implosion distributions in galaxies

We are now ready to set up a framework to predict the dark-matter-induced (along with PBH capture-induced) NS implosion rates in galaxies, which will subsequently be used for FRB studies, for each of the benchmark normalized implosion time models shown in Eq. 5.3 in spirals, ellipticals, and dwarfs. To do this, we follow a similar recipe to that provided by Ref. [33], adapted to new dark-matter halo profiles and NS distributions for each type of host galaxy, and also using an improved prescription for the star formation rate.

For our Milky Way-equivalent spiral galaxy, we adopt a Navarro–Frenk–White (NFW) dark matter halo density profile [76], characterized by a scale radius $h = 10.94 \pm 1.05\,\text{kpc}$ and central density $\rho^0_{\rm NFW} = 0.787 \pm 0.037\,\text{GeV}\,\text{cm}^{-3}$, resulting in a local dark matter density $\rho_\odot = 0.359 \pm 0.017\,\text{GeV}\,\text{cm}^{-3}$. The neutron star distribution in this spiral galaxy is modeled as a thin disk described by model 1E from Ref. [85], and the total number of neutron star births is normalized to approximately 10^9 over the galaxy's lifetime as per Ref. [82]. We also assume a flat velocity profile of 300 km/s for simplicity.[2]

For the early-type elliptical galaxy, we again use an NFW dark matter halo density

[2]We have chosen to use a flat velocity profile because we are aiming to match the dynamics of galaxies in the $r = 1 - 20$ kpc region. We have also checked that this flat velocity assumption does not markedly change our predictions, relative to using a more granular velocity distribution, *e.g.* [79].

profile but adopt parameters suitable for a massive elliptical system [276]: a virial mass $M_v = 3.8 \times 10^{12}\, h_{70}^{-1}\, M_\odot$, a halo concentration $c = 9.5$, and an effective radius $R_e = 5.8\, h_{70}^{-1}\,\mathrm{kpc}$. We take the stellar component in our elliptical galaxy to follow a profile with luminosity $L_B = 4.1 \times 10^{10}\, h_{70}^{-2}\, L_\odot$, stellar mass-to-light ratio $\Upsilon_{*,B} = 8$, and a Sérsic index $m = 3.7$. The NS spatial distribution for elliptical galaxies is more extended than that of spirals; thus, we choose model 1B from Ref. [85], which provides a relatively flat radial profile and slower density decline appropriate for ellipticals. The total neutron star population over the elliptical galaxy's lifetime is also normalized to approximately 10^9, and the galaxy is assigned a flat velocity profile of 300 km/s.

Finally, for the dwarf galaxy scenario, we adopt a Burkert dark matter halo profile reflecting typical dwarf galaxy structure [77]. Specifically, we use parameters drawn from observations of the Leo T dwarf galaxy, as described in Ref. [78]. For this dwarf galaxy, we adopt a stellar mass of approximately $M_* \sim 1.5 \times 10^5\, M_\odot$. Assuming a Kroupa-like IMF [277], about 1% of the stellar population is expected to be composed of potential core-collapse progenitors (with initial masses exceeding 8 $M_\odot$), and given a mean stellar mass of about 1.5 $M_\odot$, we estimate roughly 10^3 neutron stars forming in the dwarf galaxy over its lifetime. We model the neutron star surface density using a shallow distribution based on model 1E* from Ref. [85], truncating and renormalizing the profile to match the dwarf galaxy parameters. The dwarf galaxy's internal kinematics are represented by a flat velocity profile of 20 km/s. See Sec. 2.5, and Sec. 2.6.1 for a discussion of the dark-matter halo density profiles and NS distributions for these galaxies in more detail.

To describe the historic NS birth rate, we adopt the Beacom-Hopkins [278] model of star formation for the past, up to the present peak at $t \approx 5$ Gyr that transitions

to an exponential decline thereafter. For cosmic time t_z (in Gyr), the historic star formation rate $\dot{M}^*(t_z)$ is

$$\dot{M}^*(t_z) = \begin{cases} h\,\dfrac{a + b\,t_z}{1 + \big(t_z/c\big)^d}\,, & t_z \leq 5, \\ A\,e^{-k\,t_z} + \varepsilon\,, & t_z > 5, \end{cases} \tag{5.7}$$

with best-fit parameters for $t_z \leq 5$ Gyr:

$$a = 0.017, \quad b = 0.13\ Gyr^{-1}, \quad c = 3.3\ Gyr, \quad d = 5.3, \quad h = 0.7\ Gyr^{-1}$$

and best-fit parameters for $t_z \gtrsim 5$ Gyr:

$$A = 0.3823\ Gyr^{-1}, \quad k = 0.2347\ Gyr^{-1}, \quad \varepsilon = 10^{-10}\ Gyr^{-1} \quad .$$

We rescale and normalize the star formation rate so that $\int_0^{13.8} \dot{M}^*(t_z)\,dt = 1$.
Here t_z is the cosmic time at redshift z, obtained by integrating and subsequently interpolating

$$dt = [H_0\sqrt{\Omega_m(1+z)^3 + \Omega_\Lambda}]^{-1}dz \tag{5.8}$$

with Planck 2018 parameters [2].

Armed with the star formation history, along with the NS distribution and dark matter halo properties specified for each type of galaxy in Sec. 2.6.1 & 2.5 respectively, this determines the fraction of NSs at galactocentric radius r that have had sufficient

time to collapse by the present cosmic age $t_u \simeq 13.8$ Gyr (as shown in Ref. [33])

$$F_{\rm BH}(r) = \frac{\int_0^{{\rm Max}[t_{\rm u}-t_{\rm c}(r),0]} \dot{M}^*(t_z)\ dt}{\int_0^{t_{\rm u}} \dot{M}^*(t_z)\ dt}, \tag{5.9}$$

where $t_{\rm u} \sim 13.8$ Gyr is the lifetime of the universe, and $t_{\rm c}(r)$ is the collapse time at radius r. We can similarly give the rate of NS implosions per unit galactocentric radius r by

$$\Gamma_{\rm NS\,Imp}(r) = 2\pi r \Sigma(r) \dot{M}^*(t_{\rm u} - t_{\rm c}(r)). \tag{5.10}$$

We can convert Eq. 5.9 to a normalized probability density over radius

$$\begin{aligned} p_{{\rm ADM}_{1,2}}(r_i) &\propto F_{\rm BH}(r_i), \\ \sum_i p_{{\rm ADM}_{1,2}}(r_i) &= 1. \end{aligned} \tag{5.11}$$

Using these discrete weights, we generate a sample of a thousand implosion events for each model occurring at appropriately weighted radii:

$$r_k^{ADM_{1,2}} \sim p_{ADM_{1,2}}(r_k). \tag{5.12}$$

For the null hypothesis reference sample, we instead weight by the NS distribution in each host galaxy $\Sigma_{host}(r_k)$.

This procedure gives a prediction for the expected NS implosion distributions in different types of host galaxies, as shown in Figs. 5.3–5.5.

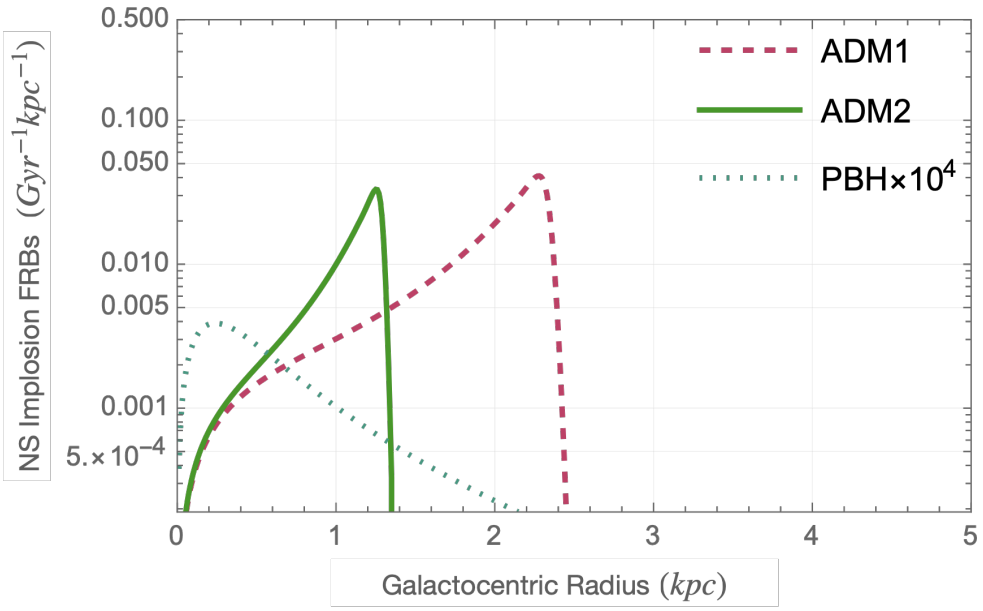

Figure 5.3: Predicted rate for NS Implosion FRBs in $\mathrm{kpc}^{-1}\mathrm{Gyr}^{-1}$ (dark-matter induced NS implosions) as a function of Galactic radius in our dwarf–galaxy model. The dashed red curve (ADM1) corresponds to $t_c\,\rho_x/v_x = 3.0\ \mathrm{Gyr\,GeV\,cm}^{-3}\,(300\,\mathrm{km\,s}^{-1})^{-1}$, while the solid green curve (ADM2) uses $t_c\,\rho_x/v_x = 15\ \mathrm{Gyr\,GeV\,cm}^{-3}\,(300\,\mathrm{km\,s}^{-1})^{-1}$. $\mathrm{PBH}_{\mathrm{max}}$ is a maximally NS-imploding model described in 5.1.1. For visibility, the PBH curve has been augmented by 4 orders of magnitude.

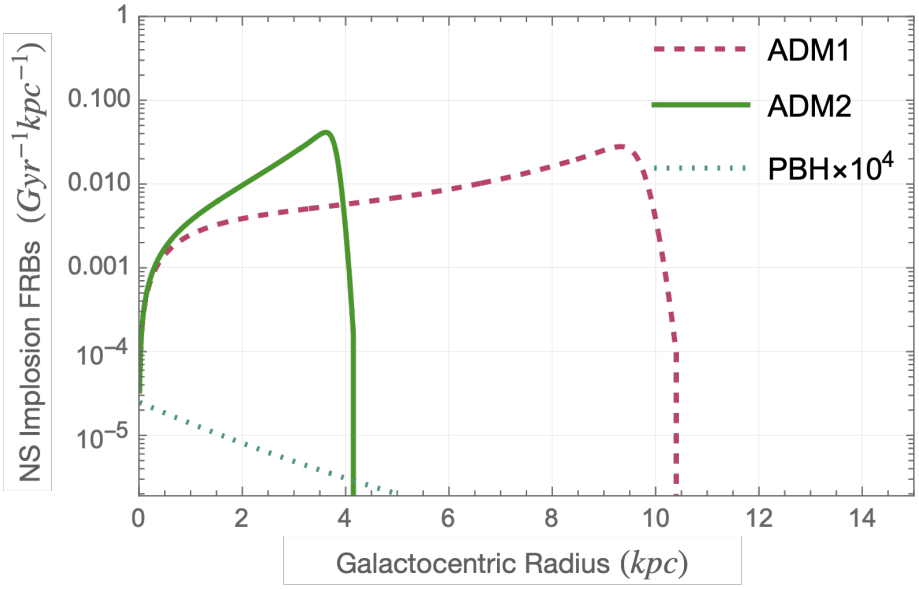

Figure 5.4: Predicted rate for NS Implosion FRBs in $\mathrm{kpc}^{-1}\mathrm{Gyr}^{-1}$ as a function of Galactic radius in our MW equivalent spiral galaxy. ADM1, ADM2 , and $\mathrm{PBH}_{\mathrm{max}}$ are defined exactly as described in Fig. 5.3

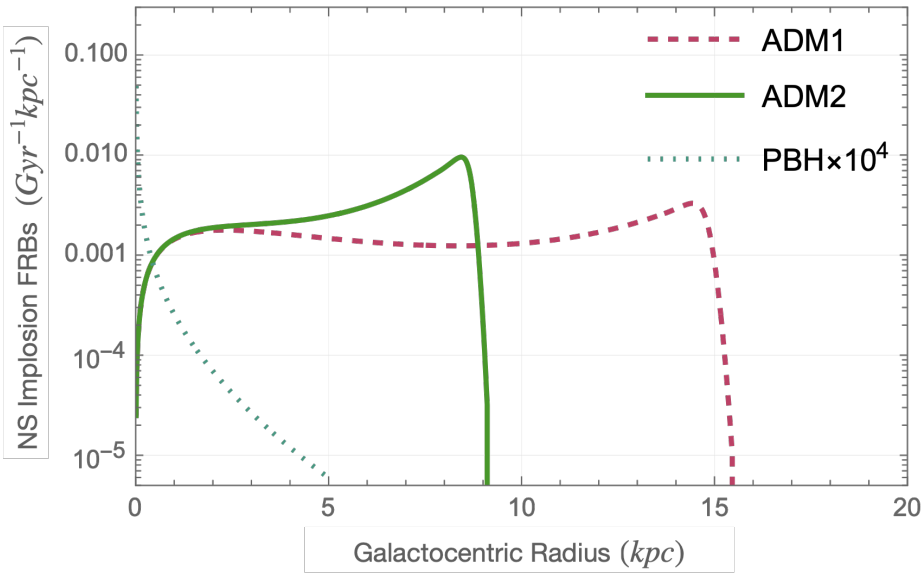

Figure 5.5: Predicted rate for NS Implosion FRBs in $\mathrm{kpc}^{-1}\mathrm{Gyr}^{-1}$ as a function of Galactic radius in our early-type elliptical model. ADM1, ADM2 , and $\mathrm{PBH}_{\mathrm{max}}$ are defined exactly as described in Fig. 5.3

Some key points immediately jump out from the results of this analysis. Fig. 5.3 shows that in low-mass dwarfs, ADM2 collapses most of the NSs within the inner kpc region, while PBH-induced implosions are negligibly rare. In MW equivalent spirals, ADM1 yields a slowly rising NS implosion rate near $r \sim 10$ kpc, while ADM2 peaks around $r \sim 4$ kpc. PBH-induced implosions remain subdominant as evident in Fig. 5.4. Owing to the steep dark-matter halo profile coupled with a flatter NS distribution, we see that in the early-type elliptical galaxies, both ADM models predict NS implosions spike sharply in the inner few kpcs as can be seen in Fig. 5.5. The more efficient collapse model ADM2 confines the NS implosions to the inner ~ 10 kpc region, while the slower ADM1 distributes them over a broader zone. Once again, the PBH-induced implosion is scant and confined to the inner kpcs.

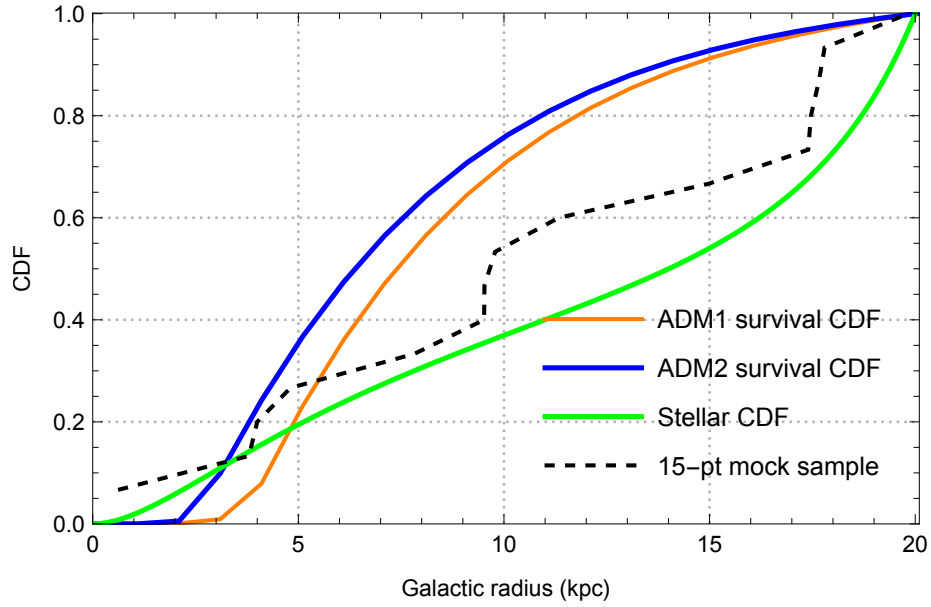

Figure 5.6: Cumulative distribution functions for surviving NS for models ADM1(orange) and ADM2(blue) in a low mass dwarf galaxy. The stellar CDF(green) gives us a baseline corresponding to the NS birth/survival using the Beacom-Hopkins SFH and NS distribution models described in the text. A 15-point mock data set (black) drawn from the baseline stellar CDF represents a realistic FRB host-localization sample for the low mass dwarf.

Fig. 5.6 shows at a glance how dark-matter induced NS implosions reshape the radial distribution of surviving NSs in a low-mass dwarf. Compared to the smooth baseline stellar CDF (green curve), the ADM1(orange) and ADM2(blue) survival curves are indicative of the fact that only the more distant NSs(away from the dwarf's galactic center) remain. The sharper drop in the ADM2 curve compared to ADM1 demonstrates how a higher collapse efficiency confines the NS implosions to a smaller radius.

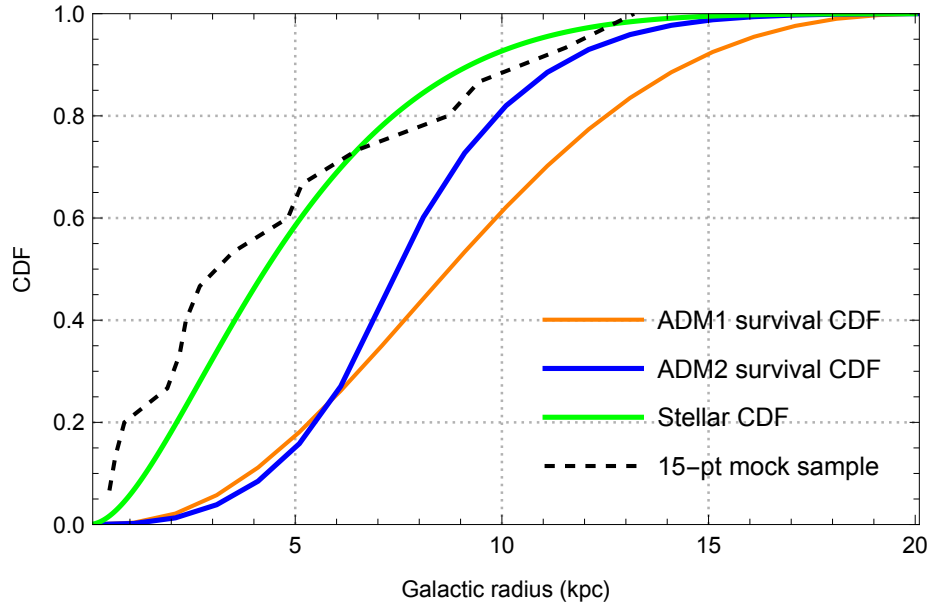

Figure 5.7: Cumulative distribution functions for surviving NS for models ADM1(orange) and ADM2(blue) in a Milky Way-like spiral galaxy. The stellar CDF(green) gives us a baseline corresponding to the NS birth/survival using the Beacom-Hopkins SFH and NS distribution models described in the text. A 15-point mock data set(black) drawn from the baseline stellar CDF represents a realistic FRB host-localization sample for the MW equivalent spiral galaxies.

For the MW equivalent spiral, Fig. 5.7 CDFs again reveal how dark-matter driven NS collapses carve out the inner galaxy. The baseline stellar CDF(green) rises steadily, reaching 50% of NSs by $r \sim 8$ kpc. Under the ADM1 scenario (orange), the survival CDF is shifted outwards, and we see that only 50% of the NSs survive within $r \sim 10$ kpc, reflecting a moderate inner-galaxy depletion as compared to the more efficient ADM2(blue) model that shifts the survival CDF further inward.

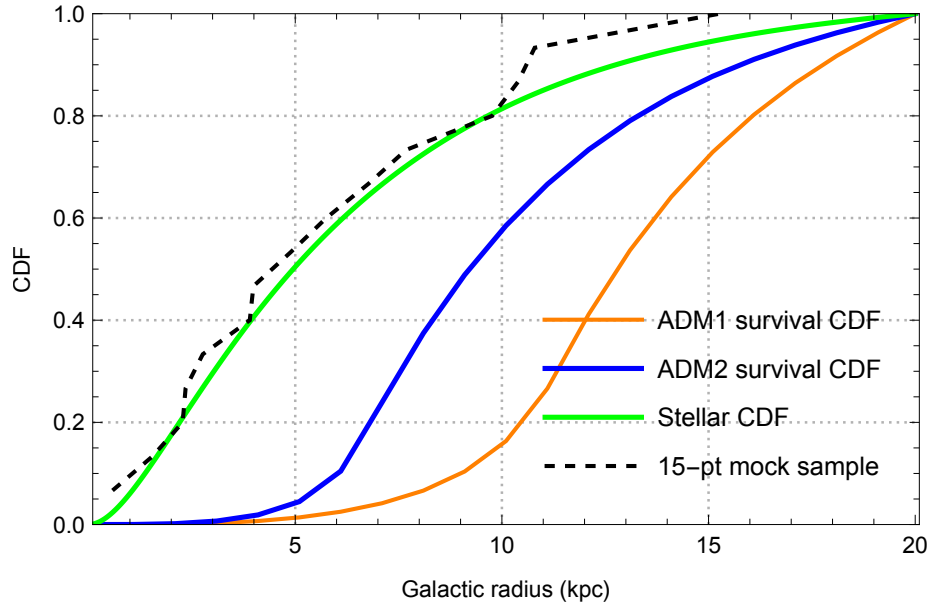

Figure 5.8: Cumulative distribution functions for surviving NS for models ADM1(orange) and ADM2(blue) in an elliptical galaxy. The stellar CDF(green) gives us a baseline corresponding to the NS birth/survival using the Beacom-Hopkins SFH and NS distribution models described in the text. A 15-point mock data set(black) drawn from the baseline stellar CDF represents a realistic FRB host-localization sample for early-type elliptical galaxies.

Fig. 5.8 shows that the baseline stellar CDF(green) reaches 50% by $r \sim 6$ kpc. Under ADM2(blue), the surviving NS CDF shifts outward, with its median at $r \sim 8$ kpc, indicating that efficient collapse removes most inner-core NSs, but still leaves a sizable central population. In the slower ADM1 case(orange), the median surviving radius moves further out to $r \sim 12$ kpc, showing that fewer NSs collapse at small r.

5.3 Fast Radio Burst Signals

Fast Radio Bursts (FRBs) are high luminosity, millisecond-duration radio pulses with large dispersive delays that imply extragalactic origin [97, 101]. While their source of origin is still unknown, a wide variety of progenitor models have been proposed for

FRBs, ranging from magnetized NS collapses, accretion of black holes, starquakes of compact stars to collision events, such as mergers of neutron stars (NS) with other NS or black holes (BH) [99].

Ref. [102] presented a Monte Carlo-based population synthesis study of FRB dispersion and scattering, focusing on the catalog of sources detected by CHIME/FRB [235]. Using this CHIME/FRB sample with redshift or localization proxies, they showed that the bulk of observed DMs are consistent with a highly ionized intergalactic medium (IGM), but with a significant scatter attributable to host galaxy environments and local circumburst medium. They model their local DM contributions as a log-normal distribution ($\mathcal{O} \sim 10^2$) based on the estimated local DM for Galactic pulses modeled by Ref. [89]. The authors argued that any large outliers can be accommodated by a dense host medium, and stressed that improved localizations would tighten constraints on baryon distributions and FRB progenitor sites. Their analysis, therefore, provides an empirical DM benchmark against which any exotic contribution (*e.g.* dark-matter-induced NS implosions) must be compared.

Having predicted the NS implosion rates for the different type of galaxies, we can now move to the next step wherein we propagate these through physically motivated free-electron density maps for each host galaxy and to test where these distributions are localized against the null "NS distribution trace" hypothesis (assuming that FRBs occur wherever NS are born/survive). This study then complements the work done by Ref. [102], who constrained host contributions without a specific dark-matter mechanism.

5.3.1 Electron-Density Distributions in Extragalactic Hosts

To predict the contribution of the dispersion measure (DM) from dark-matter-induced FRB events in external galaxies, we must adopt physically motivated models for the free-electron density in these systems. Below we summarize three cases—(i) a Milky Way-equivalent spiral, (ii) an early-type (elliptical) galaxy, and (iii) a low-mass dwarf galaxy—each evaluated at $z = 0$ and illustrated in accompanying figures 5.9 – 5.11.

Our Milky Way–equivalent spiral model follows the four-component prescription from Ref. [89]:

$$\begin{aligned} n_e^{\text{spiral}}(R,\phi,z) = n_1\, g_1(R)\ \text{sech}^2\big(z/h_1\big) \\ +n_2\, g_2(R)\ \text{sech}^2\big(z/h_2\big) \\ +n_{\text{arms}}(R,\phi,z) + n_{\text{GC}}(R,z) \end{aligned}$$

where n_1, h_1, g_1 and A_1 represent the thick disk components, n_2, h_2, g_2 and A_2 represent the thin disk components, and n_{arms} and n_{GC} represent the spiral arms and galactic center components respectively. For a detailed explanation of these components and the parameters within, we refer the reader to Ref. [89]

Figure 5.9 shows a free electron density map of such a spiral spanning from -20 kpc to 20 kpc in the disk plane. The spiral-arm ridges, inner-disk plateau, and the thin central bulge are all visible.

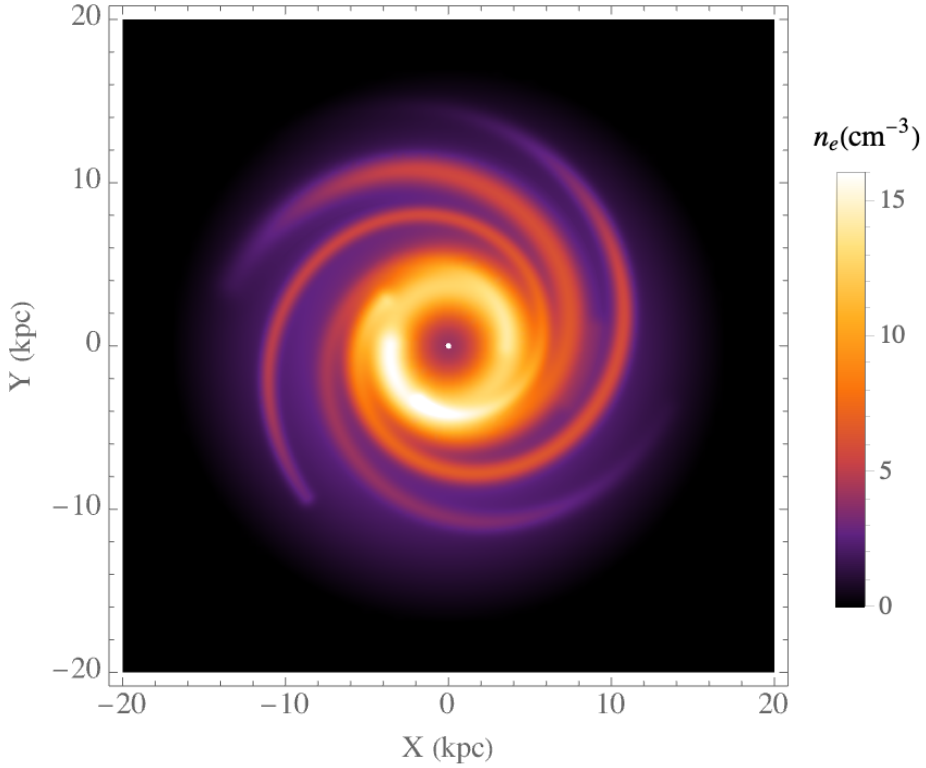

Figure 5.9: Electron density map for a MW-equivalent spiral galaxy over ±20 kpc in the disk plane. For clarity, we plot the 100-fold electron density values. The spiral-arm ridges, dense inner-disk plateau, and the thin central bulge are all visible.

We model an early-type elliptical galaxy by down-scaling the spiral's thick-disk by a factor of $\sqrt{10}$ while retaining its central bulge:

$$n_e^{\rm ellip}(x,y,z) = \frac{1}{\sqrt{10}}\, n_e^{\rm thick}(x,y,z) \;+\; n_{\rm GC}(x,y,z)\,. \tag{5.13}$$

i.e. approximating to a puffed-up version of the spiral's thick disk, giving a lower overall amplitude, plus the same central bulge. Figure 5.10 presents the resulting free electron density map of such an elliptical in the disk plane out to a radius of 20 kpc. Compared to the spiral, the elliptical's central core now dominates, while the extended disk declines more gradually with radius.

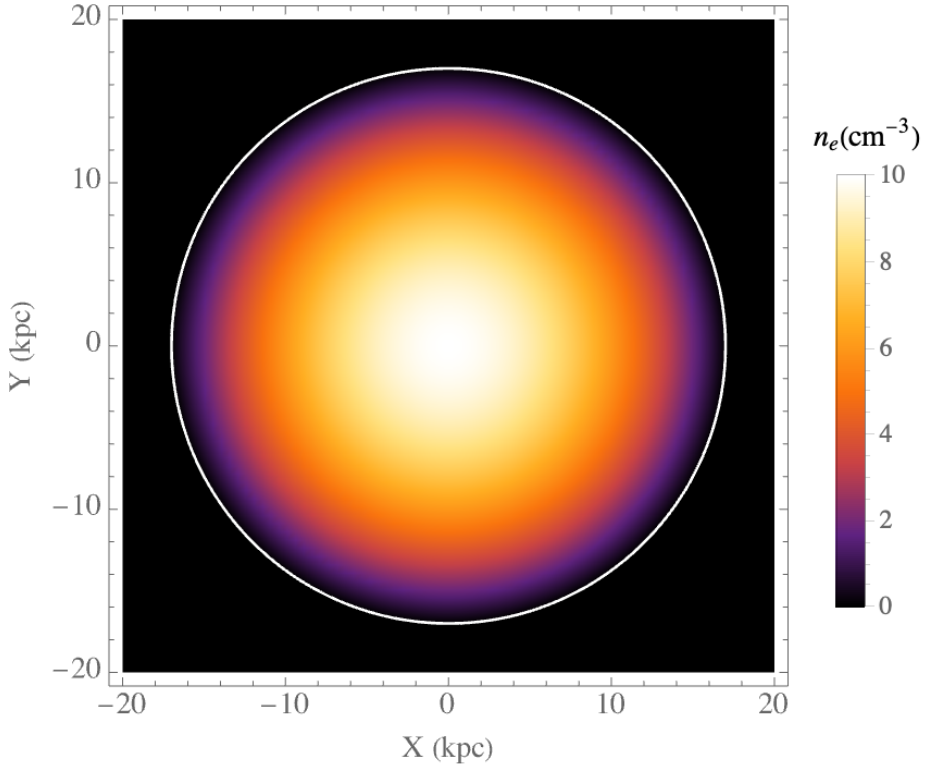

Figure 5.10: Electron density map for an early-type elliptical galaxy over ±20 kpc in the disk plane. For clarity, we plot the 100-fold electron density values. Here, the core is dominant, while the extended disk falls off more gently than in the spiral case.

Finally, we model a low-mass dwarf with a simple spherically symmetric n_e profile:

$$n_e^{\mathrm{dwarf}}(r,z) = n_0 \,\mathrm{sech}^2\big(z/0.8\,\mathrm{kpc}\big)\,\exp\big[-(R/3\,\mathrm{kpc})^2\big],$$

where $n_0 = 0.066$ and $R = \sqrt{x^2+y^2}$. Figure 5.11 covers ±5 kpc and shows the modest central peak and rapid falloff expected in such systems.

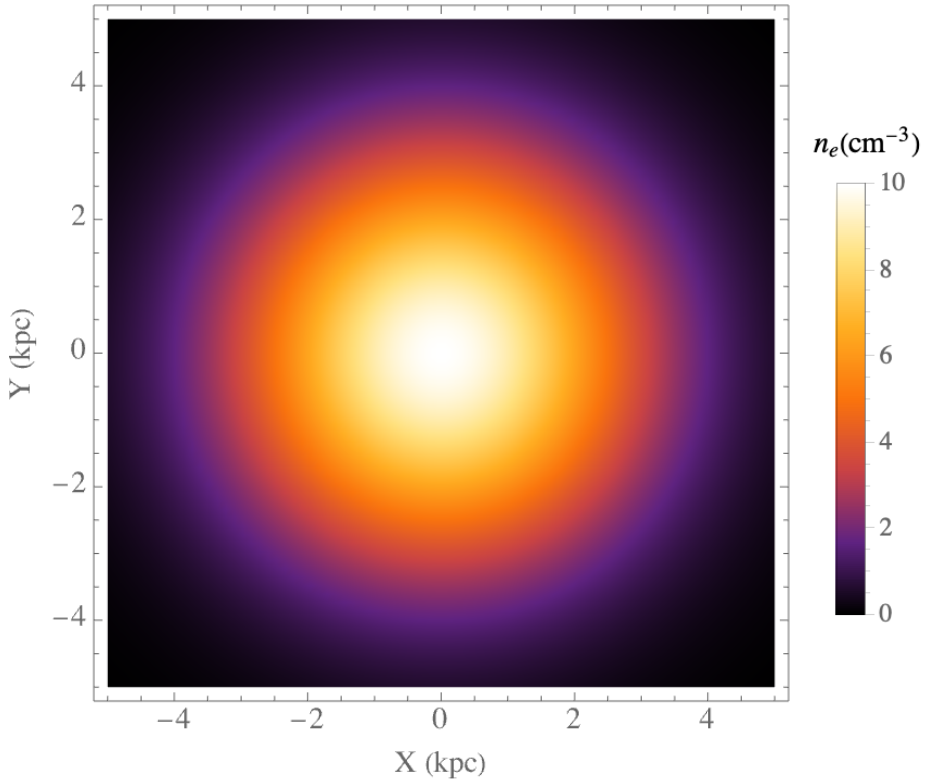

Figure 5.11: Electron density map for a low-mass dwarf galaxy with a simple spherically symmetric profile over ±5 kpc in the disk plane. For clarity, we plot the 100-fold electron density values.

Together, these three morphologies span the range of potential host-galaxy DM contributions. In MW equivalent spirals, the combination of spiral arms and the thin disk yield tens of pc cm^{-3} along typical sightlines. Early-type ellipticals, by contrast, exhibit a centrally concentrated core that dominates the DM, although a modest non-zero value persists at larger galactocentric radii Finally, low mass dwarfs contribute only a few pc cm^{-3} even along the densest lines of sight. In Section 5.3.3 , we will incorporate these n_e maps into Monte Carlo simulations of FRB DMs arising from imploding NS populations, enabling a direct comparison of the signatures expected in each type of galactic host.

5.3.2 Dispersion Measure Maps

Utilizing the free-electron density maps of Sec. 5.3.1, we create two-dimensional maps of the dispersion measure (DM) contributed by the distinct Galactic components for each galaxy type. In each case,

$$\mathrm{DM}(x,y) \;=\; \int_{z=0}^{z_{\max}} n_e(x,y,z)\,\mathrm{d}z, \tag{5.14}$$

where $n_e(x,y,z)$ is the free-electron density of the specified galactic component. All DMs are quoted in units of $\mathrm{pc\,cm^{-3}}$.

For a MW equivalent spiral:

$$\mathrm{DM_{spiral}}(x,y) \;=\; \int_{0}^{20\,\mathrm{kpc}} n_e^{\mathrm{spiral}}(x,y,z)\,\mathrm{d}z, \tag{5.15}$$

where $n_e^{\mathrm{spiral}}(x,y,z)$ follows our four-component model defined in Eq. 5.13 The highest DM (brightest region) occurs near $(x,y) \approx (0,0)$, where sightlines traverse the dense inner disk and tangent spiral arms. As we move radially outward, DM decreases smoothly, approaching zero as x and y reach the 20 kpc mark.

For the Ellipsoidal–Halo Component:

$$\mathrm{DM_{ellip}}(x,y) \;=\; \int_{0}^{20\,\mathrm{kpc}} n_e^{\mathrm{ellip}}(x,y,z)\,\mathrm{d}z, \tag{5.16}$$

where $n_e^{\mathrm{ellip}}(x,y,z)$ is given by Eq. 5.13. The map covers ± 20 kpc centered on the Galactic center. The DM values span $\sim$ 50 $\mathrm{pc\,cm^{-3}}$ (deep purple/black) up to $\sim$ 300 $\mathrm{pc\,cm^{-3}}$ (bright white). It can be seen here that the DM distribution is

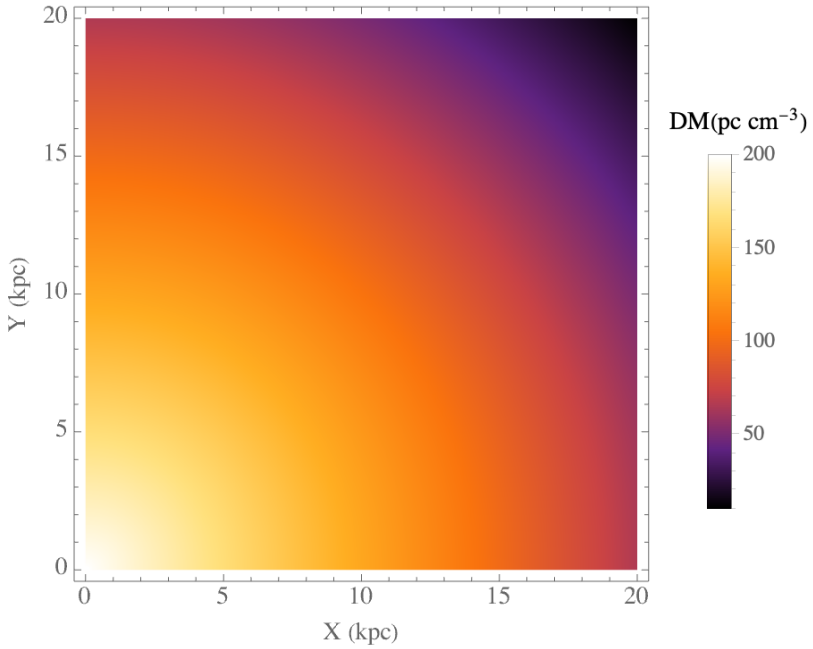

Figure 5.12: Mid-plane dispersion measure (DM) map of a MW equivalent spiral galaxy. Each point in the disk plane shows the integrated free-electron density along z, yielding DM in pc cm^{-3}.

nearly circularly symmetric, peaking at the origin and falling smoothly with increasing galactocentric radius, reaching $\lesssim 30$ pc cm^{-3} at the edges around 20 kpc.

The Dwarf-Galaxy component is modeled by:

$$\mathrm{DM}_{\mathrm{dwarf}}(x,y) \;=\; \int_0^{5\,\mathrm{kpc}} n_e^{\mathrm{dwarf}}(x,y,z)\,\mathrm{d}z, \tag{5.17}$$

where $n_e^{\mathrm{dwarf}}(x,y,z)$ is a compact, centrally concentrated dwarf-galaxy electron density as shown in Eq. 5.14. The map spans from -5 kpc to 5 kpc in the Galactic midplane, and the resultant integrated DM along z ranges from 10 pc cm^{-3} (dark purple/black) in the sparser regions, up to 50 pc cm^{-3} (bright white) in the denser core.

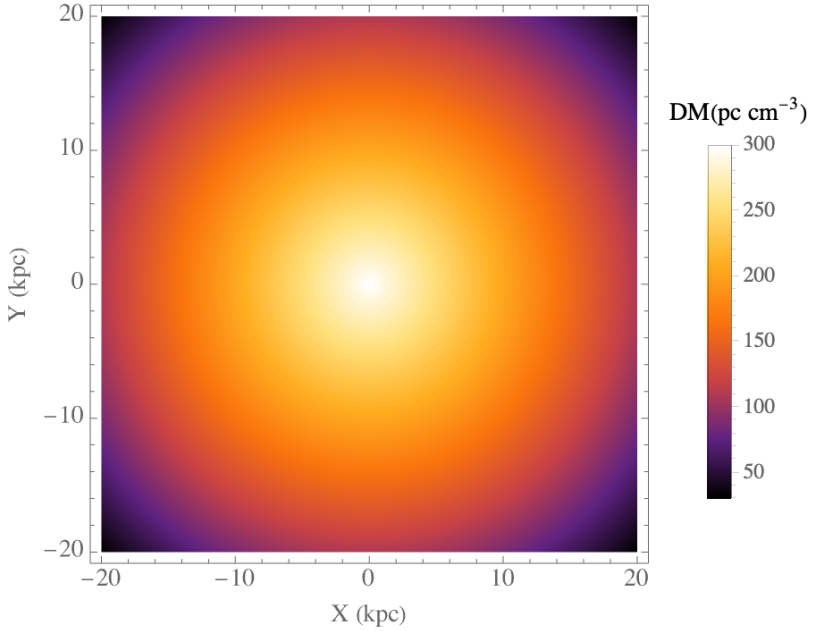

Figure 5.13: Mid-plane dispersion measure (DM) map of an early-type elliptical galaxy. Each point in the disk plane shows the integrated free-electron density along z, yielding DM in pc cm^{-3}.

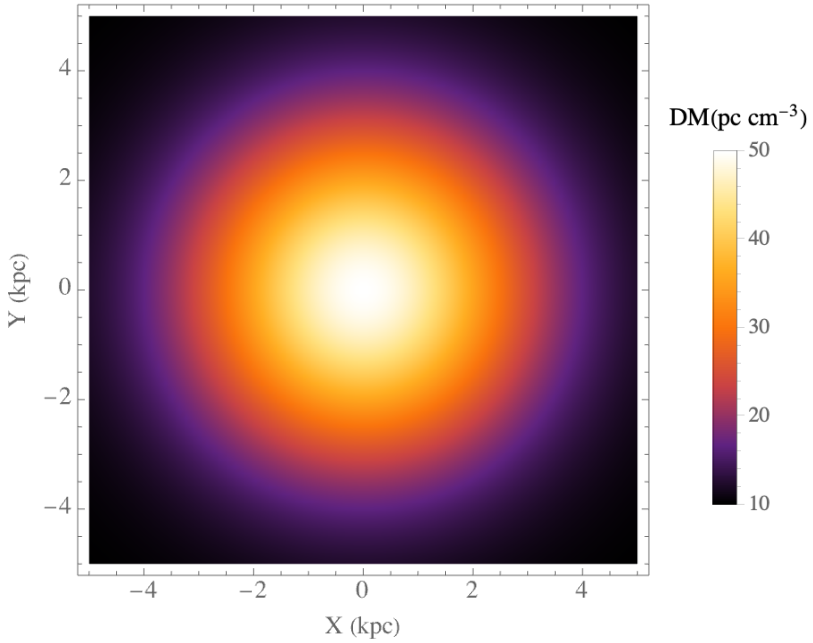

Figure 5.14: Mid-plane dispersion measure (DM) map of a low-mass dwarf galaxy. Each point in the disk plane shows the integrated free-electron density along z, yielding DM in pc cm^{-3}.

A nearly isotropic decline is observed in DM toward the outskirts of the dwarf. Compared to the spiral disk or halo, the dwarf-galaxy contribution is confined to a few kiloparsecs and is almost negligible outside its central region. Together, these maps illustrate how distinct Galactic structures shape the observed dispersion measures along different lines of sight.

5.3.3 Predicted DM Distributions for NS implosion FRBs

Having constructed the free-electron distributions for Milky Way-equivalent spirals, early-type ellipticals, and low-mass dwarfs in Sec. 5.3.1, we now incorporate those n_e maps into our Monte Carlo pipeline to predict DM distributions expected from dark matter-induced NS implosions.

For each simulated implosion event at galactocentric radius r_k along our chosen reference slice $y = 0$, we compute the host contribution

$$\mathrm{DM}_{\mathrm{host}}(r_k) = \int n_e(x = r_k, y = 0, z)\, dz \tag{5.18}$$

directly from the host maps as represented in Fig. 5.15.

To account for small-scale fluctuations due to features like H II regions or supernova remnants in the FRB's immediate environment, we add a stochastic contribution DM_{local}, drawn from a log-normal distribution truncated at 2σ , following the methodology of Cordes & Lazio's NE2001 model and its extension in recent FRB population studies [89, 102]

$$\mathrm{DM}_{\mathrm{local}} \sim \log \mathcal{N}(\mu = 0.18, \sigma = 1.09). \tag{5.19}$$

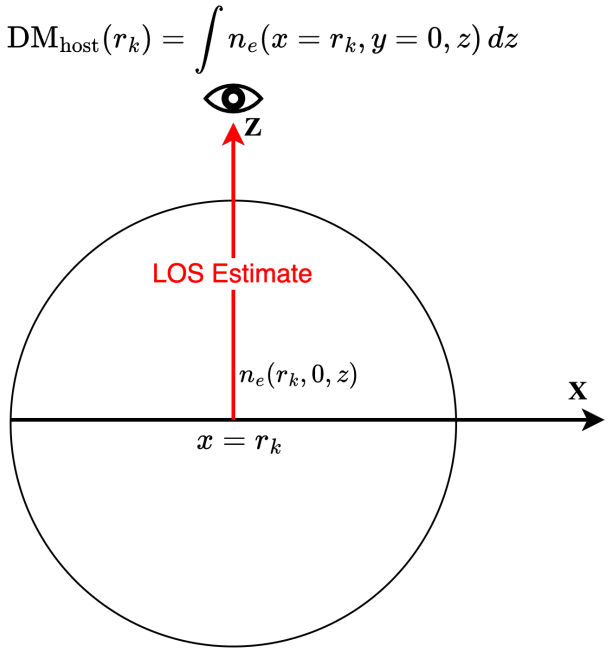

Figure 5.15: Geometry for dispersion measure (DM) integration. The host galaxy is oriented with disk plane in the XY plane, where y=0, and the observer is located in the Z direction. The line-of-sight path (red arrow) is integrated through the host electron density distribution $n_e(R, z)$, yielding Eq. 5.18.

Then the total DM becomes

$$\mathrm{DM}_{\mathrm{total}} = \mathrm{DM}_{\mathrm{host}}(r_k) + \mathrm{DM}_{\mathrm{local}} \tag{5.20}$$

Now we can generate probability density functions of $\mathrm{DM}_{\mathrm{total}}$ for each host morphology under our two benchmark asymmetric dark matter models ADM1 and ADM2, as well as a null hypothesis in which FRBs simply trace the underlying NS distribution. Figs. 5.16, 5.17 & 5.18 display the PDFs for the total DM distributions expected for a low-mass dwarf, MW equivalent spiral, and an early-type elliptical host respectively.

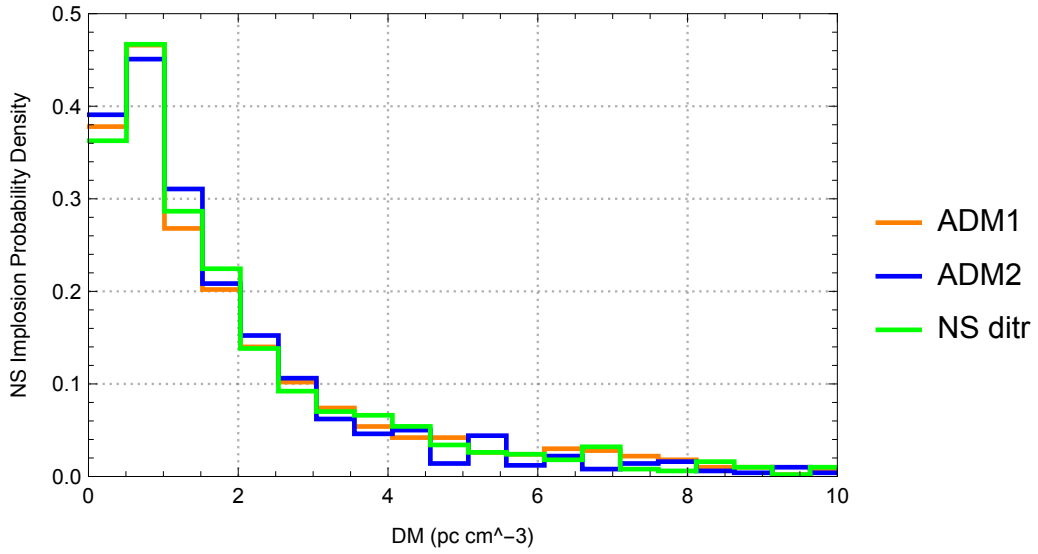

Figure 5.16: Probability density of a low-mass dwarf host-galaxy dispersion measures for NS implosions under two distinct asymmetric dark matter models namely ADM1(orange) and ADM2(blue), defined by $t_c\rho_x/v_x = 3$ & 15 Gyr GeV/cm^{-3}/(300 km/s). These are compared against the hypothesis that NS implosion FRBs simply trace the underlying NS population (green).

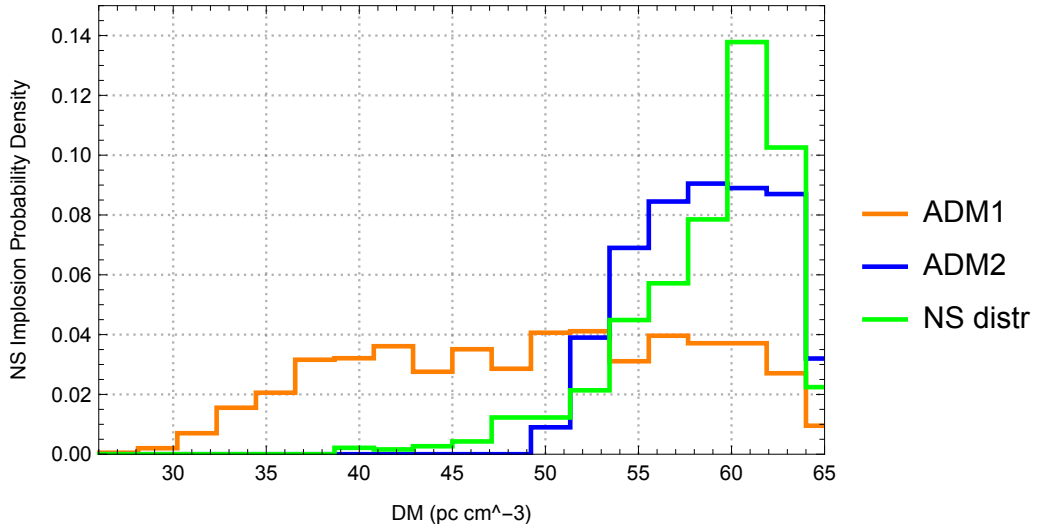

Figure 5.17: Probability density of a MW equivalent spiral host-galaxy dispersion measures for NS implosions under ADM1(orange) and ADM2(blue). These are compared against the hypothesis that NS implosion FRBs simply trace the underlying NS population (green).

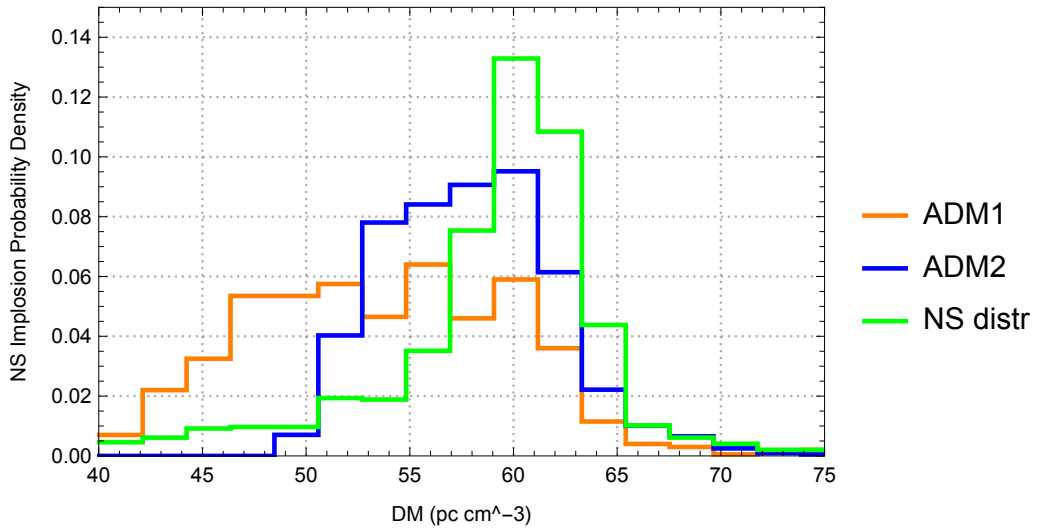

Figure 5.18: Probability density of an early-type elliptical host-galaxy dispersion measures for NS implosions under ADM1(orange) and ADM2(blue). These are compared against the hypothesis that NS implosion FRBs simply trace the underlying NS population (green).

Looking at these plots closely, it is of interest to note that ADM2 generally produces DM distributions more closely aligned with the baseline NS case. We shall return to address the importance of this find in the next section.

Our implosion rate predictions are subject to several systematic uncertainties that may affect both the normalization and shape of the predicted FRB dispersion-measure distributions. These include:

1. **Electron density models:** Variations in the assumed host-galaxy n_e distribution (e.g. scale heights, spiral-arm geometry, or clumping) can shift the predicted DM probability distributions.

2. **Neutron star population modeling:** Uncertainties in the NS birth distribution, natal kick velocities, and survival fractions affect the baseline CDFs used

in our KS tests. Different star-formation histories or compact-object migration scenarios may introduce biases.

3. **FRB detection and selection:**Instrumental thresholds, sky coverage, and localization fractions influence which bursts are included in our comparisons.

4. **Dark matter capture physics:** The scaling of implosion timescales $t_c \rho_\chi / v_\chi$ depends on halo profile assumptions (cored versus cusped), and local dark matter velocity dispersions. Primordial black hole capture rates likewise depend sensitively on halo structure and encounter dynamics.

While our benchmark ADM1, ADM2, and PBHmax models bracket plausible extremes, these systematic uncertainties highlight that our results should be interpreted as forecasts rather than definitive exclusions. Future refinements to halo modeling, electron density maps, and FRB catalog completeness will be crucial to sharpen constraints on dark matter–induced neutron star implosions.

5.4 Conclusions

In this chapter, we have demonstrated how dark matter-induced NS implosions imprint distinctive DMs on the resulting FRBs. By folding detailed host-galaxy free-electron density maps through our implosion-rate models, we find that spiral galaxies yield broad, extended DM distributions, as shown in Fig. 5.17, while ellipticals, as displayed in Fig. 5.18, produce a more centrally dominated DM distribution. Dwarfs, on the other hand, show the least variation from the null model as evident in Fig. 5.16.

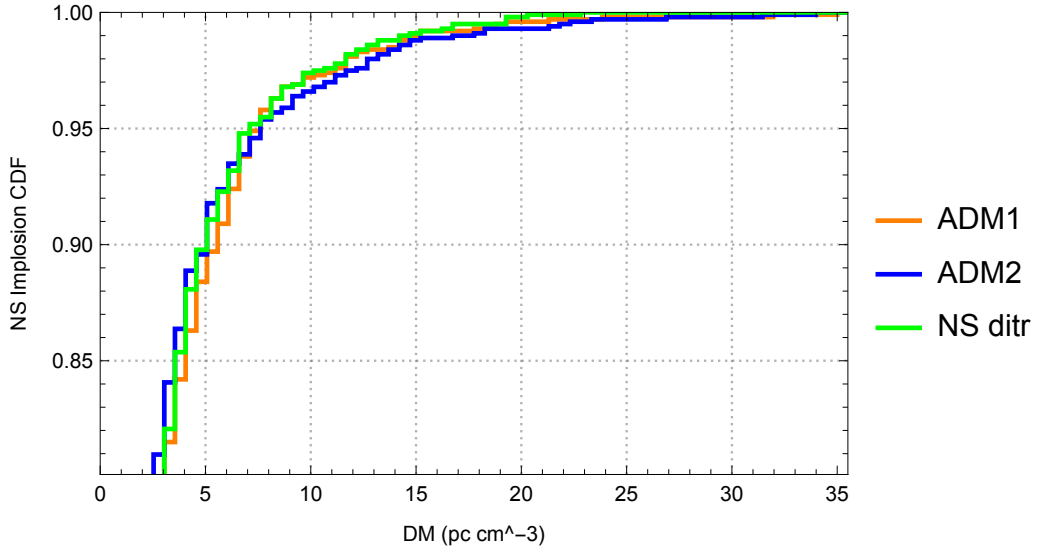

Figure 5.19: CDFs of predicted DM for NS implosion models ADM1(orange) and ADM2(blue), along with the predicted DM for NS distribution for the low mass dwarf(green). Note that ADM1 and ADM2 are defined the same way as in Fig. 5.3.

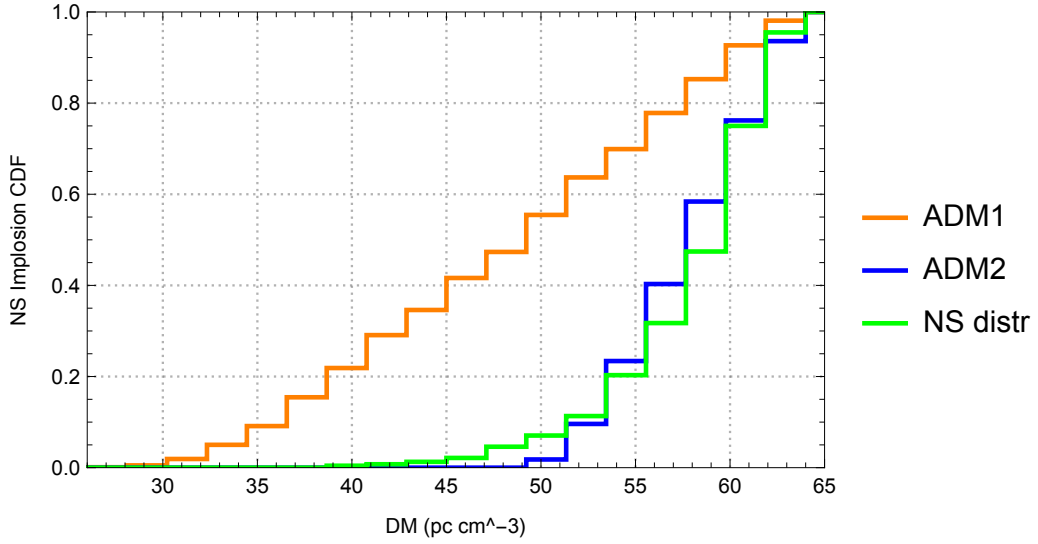

Figure 5.20: CDFs of predicted DM for NS implosion models ADM1(orange) and ADM2(blue), along with the predicted DM for NS distribution for the MW equivalent spiral(green). Note that ADM1 and ADM2 are defined the same way as in Fig. 5.3.

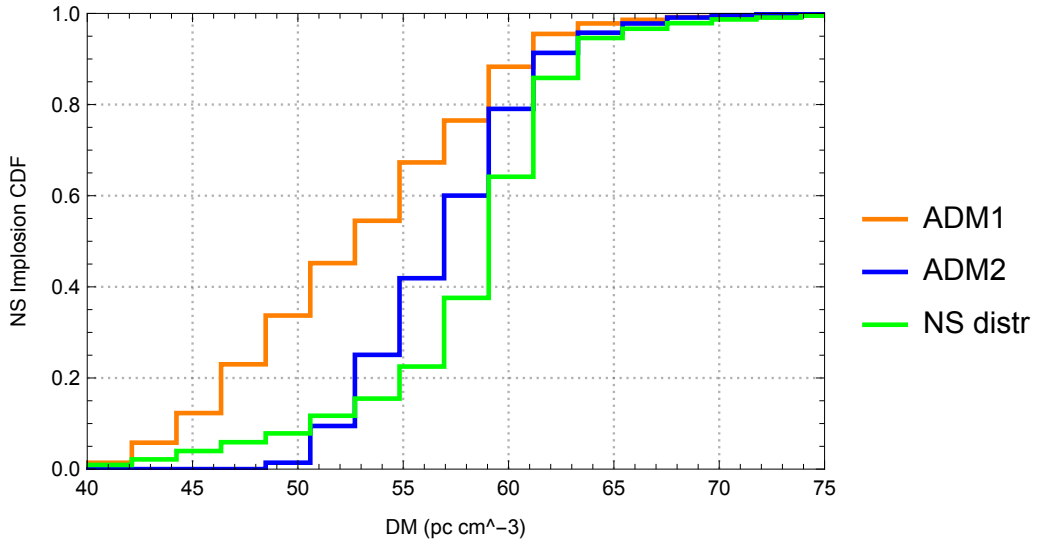

Figure 5.21: CDFs of predicted DM for NS implosion models ADM1(orange) and ADM2(blue), along with the predicted DM for NS distribution for the early-type elliptical(green). Note that ADM1 and ADM2 are defined the same way as in Fig. 5.3.

Understanding which dark matter scenarios align with or deviate from the standard NS distribution is crucial for designing FRB surveys and assessing how many localizations would be required to uncover or rule out specific implosion mechanisms.

We have already seen the PDFs for the DMs created by a standard NS distribution alongside ADM1 and ADM2 are shown in Figs. 5.16-5.18. The corresponding CDFs (Figs. 5.19-5.21) show that the ADM2 model generally coincides more closely with the NS distributions for the host galaxy. This indicates that it may be more challenging to discriminate a dark matter-induced FRB population from ordinary NS bursts purely using their DM distributions. In particular, since ADM2 produces a DM distribution that more closely tracks the underlying NS density, it would be hard to tell the FRBs apart from the host's pulsar population unless we have a larger sample of FRBs for said host. By contrast, models, like ADM1 in spirals, whose CDFs diverge markedly from the NS baseline, probably are easier to discriminate from the NS distribution

model, with fewer DM events.

Having presented the PDFs for each host morphology, we now use the cumulative distribution functions to quantify the statistical separation between implosion models and the baseline NS population, both in the case that our data provides a galactocentric radius for FRB events (Figures 5.6-5.8), and for the case that we have DM data for the FRBs (Figures 5.20-5.21).

To quantify the data required to test ADM1 and ADM2 against the standard NS distribution, we apply a Kolmogorov-Smirnov (KS) test. The KS test tells us how likely it is that we would see two sets of data samples if they were drawn from the same probability distribution [279], by quantifying a distance between the baseline (here our NS distribution) and the CDF of the reference (here our ADM model). We first calculated the distance D_{obs}, which is simply the largest vertical difference between two CDFs. To decide how many events n are needed to distinguish these distributions at the 95% confidence level, we compare this distance against $D_{0.05}(n)$, a function which is the critical K-S distance at the 95% confidence level. Note, that unless otherwise stated, KS tests are performed at a two-sample significance level $\alpha = 0.05$. Required sample sizes quoted in the figures correspond to $\gtrsim 80\%$ statistical power, estimated via 10^4 Monte Carlo mock draws under the competing hypotheses (ADM vs. stellar baseline).

For the galactocentric distribution CDFs (Figures 5.6-5.8), specifically for the MW-like CDFs, we find that ~ 12 events are required to distinguish ADM1 from the standard NS distribution, and ~ 20 events are required to distinguish ADM2 from the standard NS distribution.

For the DM distribution CDFs (Figures 5.20-5.21), specifically for DMs from MW-like CDFs, we find that at least 15 events are required to distinguish ADM1 from the standard NS distribution, and at least 20 events are required to distinguish ADM2 from the standard NS distribution.

So in general, we have found that around 12 localized FRBs per galaxy type are required to begin distinguishing between ADM1 and the null hypothesis (standard NS distribution) at a 95% confidence level. In contrast, the number of DM events required to distinguish the null hypothesis from ADM1 in a MW-like galaxy is ~ 15. However, we note that the DM mock data as utilized above would require appropriately subtracting off the IGM component of the DM to extract only the DM from the host galaxy and the Milky Way. Such a procedure could be pursued and quantified in follow-on work.

Chapter 6

Summary and Future Work

6.1 Summary

In this thesis, we have investigated the detection of dark matter using neutron stars through multiple mechanisms. For certain models of dark matter, we can expect capture and accumulation of the dark matter particles inside neutron stars, leading to several observable effects.

It is useful to summarize the benchmark dark matter scenarios explored in this thesis. Throughout Chapters 2–5 we examined asymmetric dark matter models with differing implosion timescales (ADM1 and ADM2), a maximal primordial black hole capture scenario (PBHmax), inelastic dark matter with exterior annihilations, and generic dark matter–nucleon scattering producing neutron star heating. Table 6.1 recaps these scenarios and highlights their primary observational probes. Future work should extend these studies by combining larger fast radio burst samples with improved localization, targeted searches for infrared emission from nearby neutron stars, and continued development of theoretical models for dark matter capture and implosion. In particular, resolving the systematics of electron density maps and the

Table 6.1: Dark matter scenarios explored in this thesis and their main observational probes.

Scenario	**Primary Observable**
ADM1 / ADM2	NS implosions traced in FRB dispersion measures
PBHmax	Rapid NS implosions and associated FRBs
Inelastic dark matter	γ-ray and neutrino signals from exterior annihilation
Dark matter-nucleon scattering	Infrared emission from nearby old NSs

potential role of dark-matter–admixed neutron stars will be essential for sharpening these constraints.

After briefly introducing the pertinent physics in Chapter 2, we present the first study of inelastic dark matter annihilating *outside* NSs in Chapter 3, which discusses an effect that arises when upon being captured, the dark matter particles are unable to fully thermalize with the NS due to inelastic kinematics. In fact, if elastic interactions are sufficiently suppressed relative to the inelastic channel, a fraction of the dark matter remains in long-lived orbits extending beyond the stellar volume. This effect is most pronounced for inelastic mass splittings in the range $\delta m \sim 45 - 285$ MeV, for which a sizable portion of the captured dark-matter population can annihilate outside the neutron star. We derived a model-independent expression for the exterior annihilation rate as a function of the interstate mass splitting δm, and focused on the NS population in the galactic center, where the dark-matter halo density is maximized and NS-focused annihilation can dominate over halo annihilation. From this, we computed the expected γ-ray and neutrino fluxes for various annihilation channels.

To obtain current constraints, our procedure for setting the H.E.S.S. bound conservatively required the γ-ray flux from dark matter annihilation to exceed the total γ-ray flux from the Galactic Center, with the hope that future analyses may improve on

this method and find a stronger bound. We also computed the sensitivity of next-generation observatories to this signal. Depending on the annihilation channel, as well as the assumed dark matter and NS distributions, future neutrino and γ-ray telescopes could reach inelastic cross-sections as low as $\sim 2 \times 10^{-47}$ cm^2. For a cuspy generalized NFW dark-matter profile motivated by adiabatic contraction studies, and various NS distributions, we have placed constraints based on H.E.S.S. Galactic Center observations on the inelastic dark matter-nucleon cross-section that can reach down to $\sim 3 \times 10^{-46}$ cm^2 in the case of direct annihilation to photons, for dark matter masses ranging $10^2 - 10^5$ GeV. This chapter, therefore, demonstrated that NSs in dense dark-matter environments can probe inelastic dark-matter models across a mass range that spans $\sim$10 orders of magnitude. For these models, nuclear scattering in direct detection experiments is either kinematically forbidden or has a minuscule rate, potentially making NSs the only viable probe.

While Chapter 3 focused on the NS distribution as a whole, Chapter 4 shows that even individual NSs are indeed excellent targets for observing dark-matter annihilation effects. Indeed, a nearby NS serves as an ideal target for late-time reheating searches, such as those induced by dark-matter capture, albeit precise distances are required. To this end, we have refined the local ($r \lesssim 1$ kpc) free–electron density map using pulsar parallax measurements, yielding improved dispersion-measure (DM)–based distance estimates in Chapter 4.

This work was motivated by the fact that the current electron column density models, like YMW16 and NE2001, are trained to match the electron column density over kpc scales in the Milky Way, but lack accuracy in regions closer to Earth. So, in our quest to find the nearest NS, we introduced a new, local kiloparsec electron density

map shown in Fig. 4.1. This revised map allowed us to pinpoint promising nearby pulsar candidates that are ideal for follow-up parallax observations, as summarized in the table in Figure 4.1. We further motivated better pulsar distance estimates by showing that the upcoming telescopes like the ELT and TMT, with the capability to image in infrared to far-optical wavelengths, could detect a dark matter-kinetic or annihilation heated NS with exposure times of order $\sim 10^3 - 10^6$ seconds.

In Chapter 5, we turned to extragalactic phenomena possibly associated with NSs. We explore the idea that some fast radio bursts could originate as the NS explosively sheds its magnetosphere upon implosion triggered by dark matter accumulation. We examined this scenario in three representative host galaxy environments—Milky Way–like spirals, early-type ellipticals, and low-mass dwarfs. Starting from physically motivated dark matter halo profiles, NS spatial distributions, and star-formation history, we derived both, the cumulative implosion fraction $F_{\rm BH}(r)$ and the present-epoch implosion rate $\Gamma_{\rm NS\,Imp}(r)$ as functions of galactocentric radius. By folding these weightings through detailed free-electron density models ($n_e^{\rm spiral}$, $n_e^{\rm ellip}$, and $n_e^{\rm dwarf}$) (plus a log-normal local dark-matter component), we generated Monte Carlo realizations of the total host-galaxy DM distribution under two benchmark asymmetric dark-matter (ADM) scenarios. In spirals, the resulting DM distributions are broad, peaking around $50 - 60$ pc cm^{-3} and extending into high DM tails, as evident from Figs. 5.17 & 5.20. Ellipticals produce a more core-dominated distribution of DMs that cluster near 60 pc cm^{-3}, reflecting the centrally concentrated collapse of NS in these older systems as shown in Figs. 5.18 & 5.21. Dwarf galaxies, which host far fewer NS and lower dark matter densities, yield minimal DMs of a few pc cm^{-3} along most lines of sight. This particular study, as a whole, thus shines a light on

the possibility of dark-matter-induced NS implosions being the origin story behind FRBs.

6.2 Future Work

Building on this thesis, there are several extensions that would be interesting to explore. While we focused on a dark-photon-mediated inelastic model in Chapter 3, it would be equally valuable to embed other concrete inelastic dark-matter models (*e.g.* supersymmetric neutralinos, magnetic inelastic dark matter), complete with their specific mediator masses and coupling strengths, into the exterior annihilation framework. Doing so would translate our model-independent flux estimates into detailed model-dependent γ-ray and neutrino spectra, thereby enabling tighter constraints on each candidate's parameter space.

The future work for nearby pulsars is straightforward: the candidates we have identified should have their parallaxes measured, so that the nearest neutron star to Earth can be firmly established.

In Chapter 5 we developed the FRB dispersion measure analysis for spiral, elliptical, and dwarf hosts. A valuable refinement would be to sample a broader range of halo masses and galaxy morphologies to quantify how dark-matter-induced NS implosion FRB signatures vary with host mass, concentration, and shape. Another compelling direction would be to augment the FRB dispersion measure analysis with a parallel search for gravitational wave (GW) counterparts to dark-matter-induced NS implosions. For instance, if we consider a collapse scenario where a self-gravitating dark-matter core inside the star exceeds its own Chandrasekhar limit and collapses nearly spherically, we might expect a resultant short, high-frequency gravitational

wave burst.

By correlating the predicted dispersion measure of a simulated burst with its corresponding gravitational wave signature, we might collect a catalogue of paired radio and gravitational predictions for dark-matter-induced implosions. This dual catalog would lend itself to a coincident search strategy: one could scan wide-field FRB surveys (*e.g.* CHIME/FRB, SKA) for high dispersion events and, in parallel, examine the gravitational wave detector data (*e.g.* Advanced LIGO-Virgo-KAGRA) for temporally and spatially aligned signals within the appropriate frequency bands, and test this complete dataset against dark matter models.

Bibliography

[1] Vera C. Rubin and Jr. Ford, W. Kent. Rotation of the Andromeda Nebula from a Spectroscopic Survey of Emission Regions. *The Astrophysical Journal*, 159:379, February 1970.

[2] N. Aghanim et al. Planck 2018 results. VI. Cosmological parameters. *Astron. Astrophys.*, 641:A6, 2020. [Erratum: Astron.Astrophys. 652, C4 (2021)].

[3] Gianfranco Bertone, Dan Hooper, and Joseph Silk. Particle dark matter: Evidence, candidates and constraints. *Phys. Rept.*, 405:279–390, 2005.

[4] Mark W. Goodman and Edward Witten. Detectability of Certain Dark Matter Candidates. *Phys. Rev. D*, 31:3059, 1985.

[5] Christopher Cappiello and John F. Beacom. Strong New Limits on Light Dark Matter from Neutrino Experiments. *Phys. Rev. D*, 100(10):103011, 2019.

[6] Javier F. Acevedo, Joseph Bramante, Qinrui Liu, and Narayani Tyagi. Neutrino and gamma-ray signatures of inelastic dark matter annihilating outside neutron stars. *Journal of Cosmology and Astroparticle Physics*, 03:028, 2025.

[7] Arnaud de Lavallaz and Malcolm Fairbairn. Neutron Stars as Dark Matter Probes. *Phys. Rev.*, D81:123521, 2010.

[8] John Ellis, Andi Hektor, Gert Hütsi, Kristjan Kannike, Luca Marzola, Martti Raidal, and Ville Vaskonen. Search for dark matter effects on gravitational signals from neutron star mergers. *Physics Letters B*, 781:607–610, Jun 2018.

[9] Javier F. Acevedo, Joseph Bramante, Qinrui Liu, and Narayani Tyagi. Neutrino and gamma-ray signatures of inelastic dark matter annihilating outside neutron stars. *Journal of Cosmology and Astroparticle Physics*, 03:028, 2025.

[10] Joseph Bramante, Katherine Mack, Nirmal Raj, Lijing Shao, and Narayani Tyagi. Seeking the nearest neutron stars using a new local electron density map. 11 2024.

[11] Joseph Bramante and Tim Linden. Detecting Dark Matter with Imploding Pulsars in the Galactic Center. *Phys. Rev. Lett.*, 113(19):191301, 2014.

[12] Jim Fuller and Christian Ott. Dark Matter-induced Collapse of Neutron Stars: A Possible Link Between Fast Radio Bursts and the Missing Pulsar Problem. *Mon. Not. Roy. Astron. Soc.*, 450(1):L71–L75, 2015.

[13] Joseph Bramante and Tim Linden. On the r-Process Enrichment of Dwarf Spheroidal Galaxies. *Astrophys. J.*, 826(1):57, 2016.

[14] F. Zwicky. Die Rotverschiebung von extragalaktischen Nebeln. *Helvetica Physica Acta*, 6:110–127, January 1933.

[15] Andrew Robertson, Richard Massey, and Vincent Eke. What does the Bullet Cluster tell us about self-interacting dark matter? *Mon. Not. Roy. Astron. Soc.*, 465(1):569–587, 2017.

[16] A. J. Deason, V. Belokurov, N. W. Evans, and J. An. Broken degeneracies: the rotation curve and velocity anisotropy of the Milky Way halo. *MNRAS*, 424(1):L44–L48, July 2012.

[17] Richard H. Cyburt, Brian D. Fields, Vasiliki Pavlidou, and Benjamin D. Wandelt. Constraining strong baryon dark matter interactions with primordial nucleosynthesis and cosmic rays. *Phys. Rev. D*, 65:123503, 2002.

[18] Kimmo Tuominen. Cold Particle Dark Matter. *Symmetry*, 13(10):1945, October 2021.

[19] Kim Griest and Marc Kamionkowski. Unitarity Limits on the Mass and Radius of Dark Matter Particles. *Phys. Rev. Lett.*, 64:615, 1990.

[20] Juri Smirnov and John F. Beacom. Tev-scale thermal WIMPs: Unitarity and its consequences. *Physical Review D*, 100(4):043029, August 2019.

[21] Bernard Carr, Kazunori Kohri, Yuuiti Sendouda, and Jun'ichi Yokoyama. Constraints on primordial black holes. *Reports on Progress in Physics*, 84(11):116902, November 2021.

[22] Edward W. Kolb and Michael S. Turner. *The Early Universe*, volume 69. Taylor and Francis, 5 2019.

[23] E. Aprile et al. First Dark Matter Search Results from the XENON1T Experiment. *Phys. Rev. Lett.*, 119(18):181301, 2017.

[24] Yu-Pan Zeng, Xiang Xiao, and Wei Wang. Constraints on pseudo-nambu-goldstone dark matter from direct detection experiment and neutron star reheating temperature. 2021.

[25] A. Bharucha, F. Brümmer, N. Desai, and S. Mutzel. Axion-like particles as mediators for dark matter: beyond freeze-out. *Journal of High Energy Physics*, 2023(2):141, March 2023.

[26] S. J. Asztalos, G. Carosi, C. Hagmann, D. Kinion, K. van Bibber, M. Hotz, L. J. Rosenberg, G. Rybka, J. Hoskins, J. Hwang, P. Sikivie, D. B. Tanner, R. Bradley, J. Clarke, and ADMX Collaboration. SQUID-Based Microwave Cavity Search for Dark-Matter Axions. *Physical Review Letters*, 104(4):041301, January 2010.

[27] K. Zioutas, S. Andriamonje, V. Arsov, S. Aune, D. Autiero, F. T. Avignone, K. Barth, A. Belov, B. Beltrán, H. Bräuninger, J. M. Carmona, S. Cebrián, E. Chesi, J. I. Collar, R. Creswick, T. Dafni, M. Davenport, L. di Lella, C. Eleftheriadis, J. Englhauser, G. Fanourakis, H. Farach, E. Ferrer, H. Fischer, J. Franz, P. Friedrich, T. Geralis, I. Giomataris, S. Gninenko, N. Goloubev, M. D. Hasinoff, F. H. Heinsius, D. H. Hoffmann, I. G. Irastorza, J. Jacoby, D. Kang, K. Königsmann, R. Kotthaus, M. Krčmar, K. Kousouris, M. Kuster, B. Lakić, C. Lasseur, A. Liolios, A. Ljubičić, G. Lutz, G. Luzón, D. W. Miller, A. Morales, J. Morales, M. Mutterer, A. Nikolaidis, A. Ortiz, T. Papaevangelou, A. Placci, G. Raffelt, J. Ruz, H. Riege, M. L. Sarsa, I. Savvidis, W. Serber, P. Serpico, Y. Semertzidis, L. Stewart, J. D. Vieira, J. Villar, L. Walckiers, and K. Zachariadou. First Results from the CERN Axion Solar Telescope. *Physical Review Letters*, 94(12):121301, April 2005.

[28] Fabio Capela, Maxim Pshirkov, and Peter Tinyakov. Constraints on primordial black holes as dark matter candidates from capture by neutron stars. *Phys.*

Rev. D, 87(12):123524, 2013.

[29] Djuna Croon, David McKeen, and Nirmal Raj. Gravitational microlensing by dark matter in extended structures. *Phys. Rev. D*, 101(8):083013, 2020.

[30] J. Aschersleben, G. Bertone, D. Horns, E. Moulin, R. F. Peletier, and M. Vecchi. Gamma rays from dark matter spikes in EAGLE simulations. *Journal of Cosmology and Astroparticle Physics*, 2024(9):005, September 2024.

[31] Hooman Davoudiasl, David E. Morrissey, Kris Sigurdson, and Sean Tulin. Hylogenesis: A Unified Origin for Baryonic Visible Matter and Antibaryonic Dark Matter. *Phys. Rev. Lett.*, 105:211304, 2010.

[32] Hooman Davoudiasl, David E. Morrissey, Kris Sigurdson, and Sean Tulin. Baryon Destruction by Asymmetric Dark Matter. *Phys. Rev. D*, 84:096008, 2011.

[33] Joseph Bramante, Tim Linden, and Yu-Dai Tsai. Searching for dark matter with neutron star mergers and quiet kilonovae. *Phys. Rev.*, D97(5):055016, 2018.

[34] Nicole F. Bell, Giorgio Busoni, Sandra Robles, and Michael Virgato. Thermalization and annihilation of dark matter in neutron stars. *JCAP*, 04:006, 2024.

[35] Jim Fuller and Christian Ott. Dark Matter-induced Collapse of Neutron Stars: A Possible Link Between Fast Radio Bursts and the Missing Pulsar Problem. *Mon. Not. Roy. Astron. Soc.*, 450(1):L71–L75, June 2015.

[36] Sean Tulin and Hai-Bo Yu. Dark Matter Self-interactions and Small Scale Structure. *Phys. Rept.*, 730:1–57, 2018.

[37] Tolga Güver, Arif Emre Erkoca, Mary Hall Reno, and Ina Sarcevic. On the capture of dark matter by neutron stars. *Journal of Cosmology and Astroparticle Physics*, 05:013, 2014.

[38] Scott W. Randall, Maxim Markevitch, Douglas Clowe, Anthony H. Gonzalez, and Marusa Bradac. Constraints on the Self-Interaction Cross-Section of Dark Matter from Numerical Simulations of the Merging Galaxy Cluster 1E 0657-56. *Astrophys. J.*, 679:1173–1180, 2008.

[39] Felix Kahlhoefer, Kai Schmidt-Hoberg, Mads T. Frandsen, and Subir Sarkar. Colliding clusters and dark matter self-interactions. *Mon. Not. Roy. Astron. Soc.*, 437(3):2865–2881, 2014.

[40] Edward Witten. Cosmic separation of phases. *Physical Review D*, 30(2):272–285, July 1984.

[41] Edward Farhi and R. L. Jaffe. Strange matter. *Physical Review D*, 30(11):2379–2390, December 1984.

[42] A. de Rujula and S. L. Glashow. Nuclearites-a novel form of cosmic radiation. *Nature*, 312(5996):734–737, December 1984.

[43] A. K. Drukier, Katherine Freese, and D. N. Spergel. Detecting Cold Dark Matter Candidates. *Phys. Rev. D*, 33:3495–3508, 1986.

[44] John Bagnasco, Michael Dine, and Scott Thomas. Detecting technibaryon dark matter. *Physics Letters B*, 320(1-2):99–104, January 1994.

[45] Daniele S. M. Alves, Siavosh R. Behbahani, Philip Schuster, and Jay G. Wacker. Composite inelastic dark matter. *Physics Letters B*, 692(5):323–326, September 2010.

[46] Hyun Min Lee, Myeonghun Park, and Verónica Sanz. Gravity-mediated (or composite) Dark Matter confronts astrophysical data. *Journal of High Energy Physics*, 2014:63, May 2014.

[47] Moira I. Gresham, Hou Keong Lou, and Kathryn M. Zurek. Astrophysical signatures of asymmetric dark matter bound states. *Physical Review D*, 98(9):096001, November 2018.

[48] Joseph Bramante, Benjamin Broerman, Rafael F. Lang, and Nirmal Raj. Saturated Overburden Scattering and the Multiscatter Frontier: Discovering Dark Matter at the Planck Mass and Beyond. *Phys. Rev. D*, 98(8):083516, 2018.

[49] Joseph Bramante, Benjamin Broerman, Jason Kumar, Rafael F. Lang, Maxim Pospelov, and Nirmal Raj. Foraging for dark matter in large volume liquid scintillator neutrino detectors with multiscatter events. *Phys. Rev. D*, 99(8):083010, 2019.

[50] Joseph Bramante, Jason Kumar, and Nirmal Raj. Dark matter astrometry at underground detectors with multiscatter events. *Phys. Rev. D*, 100(12):123016, 2019.

[51] Amit Bhoonah, Joseph Bramante, Sarah Schon, and Ningqiang Song. Detecting composite dark matter with long-range and contact interactions in gas clouds. *Physical Review D*, 103(12):123026, June 2021.

[52] Michael Clark, Amanda Depoian, Bahaa Elshimy, Abigail Kopec, Rafael F. Lang, and Juehang Qin. Direct detection limits on heavy dark matter. *Physical Review D*, 102(12):123026, December 2020.

[53] Javier F. Acevedo, Joseph Bramante, and Alan Goodman. Nuclear fusion inside dark matter. *Phys. Rev. D*, 103(12):123022, 2021.

[54] Javier F. Acevedo, Joseph Bramante, and Alan Goodman. Accelerating composite dark matter discovery with nuclear recoils and the Migdal effect. *Phys. Rev. D*, 105(2):023012, 2022.

[55] Mark B. Wise and Yue Zhang. Yukawa bound states of a large number of fermions. *Journal of High Energy Physics*, 2015:23, February 2015.

[56] Javier F. Acevedo, Yilda Boukhtouchen, Joseph Bramante, Christopher Cappiello, Gopolang Mohlabeng, and Narayani Tyagi. Loosely bound composite dark matter. *Journal of Cosmology and Astroparticle Physics*, 03:013, 2025.

[57] Z. Z. Liu et al. Constraints on Spin-Independent Nucleus Scattering with sub-GeV Weakly Interacting Massive Particle Dark Matter from the CDEX-1B Experiment at the China Jinping Underground Laboratory. *Phys. Rev. Lett.*, 123(16):161301, 2019.

[58] Yue Meng et al. Dark Matter Search Results from the PandaX-4T Commissioning Run. 7 2021.

[59] J. Aalbers et al. First Dark Matter Search Results from the LUX-ZEPLIN (LZ) Experiment. 7 2022.

[60] Joseph Bramante, Nishita Desai, Patrick Fox, Adam Martin, Bryan Ostdiek, and Tilman Plehn. Towards the Final Word on Neutralino Dark Matter. *Phys. Rev. D*, 93(6):063525, 2016.

[61] Jodi Cooley et al. Report of the Topical Group on Particle Dark Matter for Snowmass 2021. 9 2022.

[62] Orr Abramoff et al. SENSEI: Direct-Detection Constraints on Sub-GeV Dark Matter from a Shallow Underground Run Using a Prototype Skipper-CCD. *Phys. Rev. Lett.*, 122(16):161801, 2019.

[63] M. F. Albakry, I. Alkhatib, D. Alonso-González, D. W. P. Amaral, T. Aralis, T. Aramaki, I. J. Arnquist, I. Ataee Langroudy, E. Azadbakht, S. Banik, C. Bathurst, R. Bhattacharyya, P. L. Brink, R. Bunker, B. Cabrera, R. Calkins, R. A. Cameron, C. Cartaro, D. G. Cerdeño, Y. Y. Chang, M. Chaudhuri, R. Chen, N. Chott, J. Cooley, H. Coombes, J. Corbett, P. Cushman, S. Das, F. De Brienne, M. Rios, S. Dharani, M. L. di Vacri, M. D. Diamond, M. Elwan, E. Fascione, E. Figueroa-Feliciano, C. W. Fink, K. Fouts, M. Fritts, G. Gerbier, R. Germond, M. Ghaith, S. R. Golwala, J. Hall, N. Hassan, B. A. Hines, Z. Hong, E. W. Hoppe, L. Hsu, M. E. Huber, V. Iyer, D. Jardin, V. K. S. Kashyap, M. H. Kelsey, A. Kubik, N. A. Kurinsky, M. Lee, A. Li, M. Litke, J. Liu, Y. Liu, B. Loer, E. Lopez Asamar, P. Lukens, D. B. MacFarlane, R. Mahapatra, J. S. Mammo, N. Mast, A. J. Mayer, H. Meyer zu Theenhausen, É. Michaud, E. Michielin, N. Mirabolfathi, B. Mohanty, J. Nelson, H. Neog, V. Novati, J. L. Orrell, M. D. Osborne, S. M. Oser, W. A. Page,

L. Pandey, S. Pandey, R. Partridge, D. S. Pedreros, L. Perna, R. Podviianiuk, F. Ponce, S. Poudel, A. Pradeep, M. Pyle, W. Rau, E. Reid, R. Ren, T. Reynolds, A. Roberts, A. E. Robinson, T. Saab, D. Sadek, B. Sadoulet, I. Saikia, J. Sander, A. Sattari, B. Schmidt, R. W. Schnee, S. Scorza, B. Serfass, S. S. Poudel, D. J. Sincavage, P. Sinervo, J. Street, H. Sun, G. D. Terry, F. K. Thasrawala, D. Toback, R. Underwood, S. Verma, A. N. Villano, B. von Krosigk, S. L. Watkins, O. Wen, Z. Williams, M. J. Wilson, J. Winchell, C. P. Wu, K. Wykoff, S. Yellin, B. A. Young, T. C. Yu, B. Zatschler, S. Zatschler, A. Zaytsev, E. Zhang, L. Zheng, A. Zuniga, and SuperCDMS Collaboration. Search for low-mass dark matter via bremsstrahlung radiation and the Migdal effect in SuperCDMS. *Physical Review D*, 107(11):112013, June 2023.

[64] K. Abe, K. Hieda, K. Hiraide, S. Hirano, Y. Kishimoto, K. Kobayashi, S. Moriyama, K. Nakagawa, M. Nakahata, H. Ogawa, N. Oka, H. Sekiya, A. Shinozaki, Y. Suzuki, A. Takeda, O. Takachio, K. Ueshima, D. Umemoto, M. Yamashita, B. S. Yang, S. Tasaka, J. Liu, K. Martens, K. Hosokawa, K. Miuchi, A. Murata, Y. Onishi, K. Otsuka, Y. Takeuchi, Y. H. Kim, K. B. Lee, M. K. Lee, J. S. Lee, Y. Fukuda, Y. Itow, K. Masuda, Y. Nishitani, H. Takiya, H. Uchida, N. Y. Kim, Y. D. Kim, F. Kusaba, D. Motoki, K. Nishijima, K. Fujii, I. Murayama, and S. Nakamura. Search for solar axions in XMASS, a large liquid-xenon detector. *Physics Letters B*, 724(1-3):46–50, July 2013.

[65] Simeon Bird et al. Snowmass2021 Cosmic Frontier White Paper: Primordial black hole dark matter. *Phys. Dark Univ.*, 41:101231, 2023.

[66] Yang Bai, Andrew J. Long, and Sida Lu. Tests of Dark MACHOs: Lensing,

Accretion, and Glow. *Journal of Cosmology and Astroparticle Physics*, 09:044, 2020.

[67] Jeff A. Dror, Harikrishnan Ramani, Tanner Trickle, and Kathryn M. Zurek. Pulsar Timing Probes of Primordial Black Holes and Subhalos. *Phys. Rev. D*, 100(2):023003, 2019.

[68] David Tucker-Smith and Neal Weiner. Inelastic dark matter. *Phys. Rev. D*, 64:043502, 2001.

[69] G. Barello, Spencer Chang, and Christopher A. Newby. A Model Independent Approach to Inelastic Dark Matter Scattering. *Phys. Rev.*, D90(9):094027, 2014.

[70] Joseph Bramante, Patrick J. Fox, Graham D. Kribs, and Adam Martin. Inelastic frontier: Discovering dark matter at high recoil energy. *Phys. Rev. D*, 94(11):115026, December 2016.

[71] Ningqiang Song, Serge Nagorny, and Aaron C. Vincent. Pushing the frontier of WIMPy inelastic dark matter: Journey to the end of the periodic table. *Phys. Rev. D*, 104(10):103032, 2021.

[72] David Smith and Neal Weiner. Inelastic dark matter. *Physical Review D*, 64(4):043502, August 2001.

[73] Frank J. Petriello and Kathryn M. Zurek. DAMA and WIMP dark matter. *Journal of High Energy Physics*, 2008(9):047, September 2008.

[74] Yanou Cui, David E. Morrissey, David Poland, and Lisa Randall. Candidates for Inelastic Dark Matter. *JHEP*, 05:076, 2009.

[75] Spencer Chang, Rafael F. Lang, and Neal Weiner. Effect of Thallium Impurities in the DAMA Experiment on the Allowed Parameter Space for Inelastic Dark Matter. *Physical Review Letters*, 106(1):011301, January 2011.

[76] Julio F. Navarro, Carlos S. Frenk, and Simon D. M. White. The Structure of cold dark matter halos. *Astrophys. J.*, 462:563–575, 1996.

[77] A. Burkert. The Structure of dark matter halos in dwarf galaxies. *Astrophys. J. Lett.*, 447:L25, 1995.

[78] Matías Blaña, Andreas Burkert, Michael Fellhauer, Diego Calderón, Manuel Behrendt, and Marc Schartmann. The Milky Way satellite galaxy Leo T: A perturbed cored dwarf. *Advances in Applied Physics*, 692:A183, December 2024.

[79] Yoshiaki sofue. Rotation Curve of the Milky Way and the Dark Matter Density. *Galaxies*, 8(2):37, 2020.

[80] I. Goldman and S. Nussinov. Weakly Interacting Massive Particles and Neutron Stars. *Phys. Rev.*, D40:3221–3230, 1989.

[81] Chris Kouvaris and Peter Tinyakov. Constraining Asymmetric Dark Matter through observations of compact stars. *Phys. Rev.*, D83:083512, 2011.

[82] Masha Baryakhtar, Joseph Bramante, Shirley Weishi Li, Tim Linden, and Nirmal Raj. Dark Kinetic Heating of Neutron Stars and An Infrared Window On WIMPs, SIMPs, and Pure Higgsinos. *Phys. Rev. Lett.*, 119(13):131801, September 2017.

[83] Joseph Bramante and Nirmal Raj. Dark matter in compact stars. *Phys. Rept.*, 1052:1–48, 7 2024.

[84] Roland Diehl, Hubert Halloin, Karsten Kretschmer, Giselher G. Lichti, Volker Schönfelder, Andrew W. Strong, Andreas von Kienlin, Wei Wang, Pierre Jean, Jürgen Knödlseder, Jean-Pierre Roques, Georg Weidenspointner, Stephane Schanne, Dieter H. Hartmann, Christoph Winkler, and Cornelia Wunderer. Radioactive ^{26}Al from massive stars in the Galaxy. *Nature*, 439(7072):45–47, January 2006.

[85] N. Sartore, E. Ripamonti, A. Treves, and R. Turolla. Galactic neutron stars I. Space and velocity distributions in the disk and in the halo. *Astron. Astrophys.*, 510:A23, Feb 2010.

[86] Matthew McCullough and Malcolm Fairbairn. Capture of Inelastic Dark Matter in White Dwarves. *Phys. Rev.*, D81(8):083520, April 2010.

[87] Peter W. Graham, Surjeet Rajendran, and Jaime Varela. Dark Matter Triggers of Supernovae. *Phys. Rev.*, D92(6):063007, 2015.

[88] M. Ackermann, W. B. Atwood, L. Baldini, J. Ballet, G. Barbiellini, D. Bastieri, R. Bellazzini, B. Berenji, E. Bissaldi, R. D. Blandford, E. D. Bloom, R. Bonino, E. Bottacini, J. Bregeon, P. Bruel, R. Buehler, R. A. Cameron, R. Caputo, P. A. Caraveo, E. Cavazzuti, E. Charles, A. Chekhtman, C. C. Cheung, G. Chiaro, S. Ciprini, J. Cohen-Tanugi, J. Conrad, D. Costantin, F. D'Ammando, F. de Palma, S. W. Digel, N. Di Lalla, M. Di Mauro, L. Di Venere, C. Favuzzi, S. J. Fegan, W. B. Focke, A. Franckowiak, Y. Fukazawa, S. Funk, P. Fusco, F. Gargano, D. Gasparrini, N. Giglietto, F. Giordano, M. Giroletti, D. Green, I. A. Grenier, L. Guillemot, S. Guiriec, D. Horan, G. Jóhannesson, C. Johnson, S. Kensei, D. Kocevski, M. Kuss, S. Larsson, L. Latronico, J. Li, F. Longo,

F. Loparco, M. N. Lovellette, P. Lubrano, J. D. Magill, S. Maldera, D. Malyshev, A. Manfreda, M. N. Mazziotta, J. E. McEnery, M. Meyer, P. F. Michelson, W. Mitthumsiri, T. Mizuno, M. E. Monzani, E. Moretti, A. Morselli, I. V. Moskalenko, M. Negro, E. Nuss, R. Ojha, N. Omodei, M. Orienti, E. Orlando, J. F. Ormes, M. Palatiello, V. S. Paliya, D. Paneque, M. Persic, M. Pesce-Rollins, F. Piron, G. Principe, S. Rainò, R. Rando, M. Razzano, S. Razzaque, A. Reimer, O. Reimer, S. Ritz, M. Sánchez-Conde, C. Sgrò, E. J. Siskind, F. Spada, G. Spandre, P. Spinelli, D. J. Suson, H. Tajima, J. G. Thayer, J. B. Thayer, D. F. Torres, G. Tosti, E. Troja, J. Valverde, G. Vianello, K. Wood, M. Wood, and G. Zaharijas. Search for Gamma-Ray Emission from Local Primordial Black Holes with the Fermi Large Area Telescope. *The Astrophysical Journal*, 857(1):49, April 2018.

[89] James M. Cordes and T. J. W. Lazio. NE2001. 1. A New model for the galactic distribution of free electrons and its fluctuations. 7 2002.

[90] S. R. Kulkarni. Dispersion measure: Confusion, Constants & Clarity. 7 2020.

[91] J. H. Taylor and J. M. Cordes. Pulsar Distances and the Galactic Distribution of Free Electrons. *APJ*, 411:674, July 1993.

[92] J. M. Yao, R. N. Manchester, and N. Wang. A NEW ELECTRON-DENSITY MODEL FOR ESTIMATION OF PULSAR AND FRB DISTANCES. *The Astrophysical Journal*, 835(1):29, jan 2017.

[93] Danny C. Price, Chris Flynn, and Adam Deller. A comparison of Galactic electron density models using PyGEDM. *Publ. Astron. Soc. Austral.*, 38:e038, 2021.

[94] R. N. Manchester, G. B. Hobbs, A. Teoh, and M. Hobbs. The australia telescope national facility pulsar catalogue. *The Astronomical Journal*, 129(4):1993–2006, apr 2005.

[95] N. D. Ramesh Bhat, Yashwant Gupta, and A. Pramesh Rao. Pulsar Scintillation and the Local Bubble. *APJ*, 500(1):262–279, June 1998.

[96] N. D. Ramesh Bhat and Yashwant Gupta. Pulsar Scintillation in the Local Interstellar Medium: Loop I and Beyond. *The Astrophysical Journal*, 567(1):342–353, March 2002.

[97] D. R. Lorimer, M. Bailes, M. A. McLaughlin, D. J. Narkevic, and F. Crawford. A Bright Millisecond Radio Burst of Extragalactic Origin. *Science*, 318(5851):777, November 2007.

[98] Chime/Frb Collaboration, Bridget C. Andersen, Kevin Bandura, Mohit Bhardwaj, P. J. Boyle, Charanjot Brar, Tomas Cassanelli, S. Chatterjee, Pragya Chawla, Amanda M. Cook, Alice P. Curtin, Matt Dobbs, Fengqiu Adam Dong, Jakob T. Faber, Mateus Fandino, Emmanuel Fonseca, B. M. Gaensler, Utkarsh Giri, Antonio Herrera-Martin, Alex S. Hill, Adaeze Ibik, Alexander Josephy, Jane F. Kaczmarek, Zarif Kader, Victoria Kaspi, T. L. Landecker, Adam E. Lanman, Mattias Lazda, Calvin Leung, Hsiu-Hsien Lin, Kiyoshi W. Masui, Ryan McKinven, Juan Mena-Parra, Bradley W. Meyers, D. Michilli, Cherry Ng, Ayush Pandhi, Aaron B. Pearlman, Ue-Li Pen, Emily Petroff, Ziggy Pleunis, Masoud Rafiei-Ravandi, Mubdi Rahman, Scott M. Ransom, Andre Renard, Ketan R. Sand, Pranav Sanghavi, Paul Scholz, Vishwangi Shah, Kaitlyn

Shin, Seth Siegel, Kendrick Smith, Ingrid Stairs, Jianing Su, Shriharsh P. Tendulkar, Keith Vanderlinde, Haochen Wang, Dallas Wulf, and Andrew Zwaniga. CHIME/FRB Discovery of 25 Repeating Fast Radio Burst Sources. *The Astrophysical Journal*, 947(2):83, April 2023.

[99] E. Petroff, J. W. T. Hessels, and D. R. Lorimer. Fast radio bursts. *Astronomy and Astrophysics Reviews*, 27(1):4, December 2019.

[100] Bing Zhang. The physics of fast radio bursts. *Reviews of Modern Physics*, 95(3):035005, July 2023.

[101] D. Thornton, B. Stappers, M. Bailes, B. Barsdell, S. Bates, N. D. R. Bhat, M. Burgay, S. Burke-Spolaor, D. J. Champion, P. Coster, N. D'Amico, A. Jameson, S. Johnston, M. Keith, M. Kramer, L. Levin, S. Milia, C. Ng, A. Possenti, and W. van Straten. A Population of Fast Radio Bursts at Cosmological Distances. *Science*, 341(6141):53–56, July 2013.

[102] P. Chawla et al. Modeling Fast Radio Burst Dispersion and Scattering Properties in the First CHIME/FRB Catalog. *Astrophys. J.*, 927(1):35, 2022.

[103] J. P. Macquart, J. X. Prochaska, M. McQuinn, K. W. Bannister, S. Bhandari, C. K. Day, A. T. Deller, R. D. Ekers, C. W. James, L. Marnoch, S. Osłowski, C. Phillips, S. D. Ryder, D. R. Scott, R. M. Shannon, and N. Tejos. A census of baryons in the Universe from localized fast radio bursts. *Nature*, 581(7809):391–395, May 2020.

[104] J. M. Cordes, Stella Koch Ocker, and Shami Chatterjee. Redshift Estimation and Constraints on Intergalactic and Interstellar Media from Dispersion and

Scattering of Fast Radio Bursts. *The Astrophysical Journal*, 931(2):88, June 2022.

[105] Filippo Anzuini, Nicole F. Bell, Giorgio Busoni, Theo F. Motta, Sandra Robles, Anthony W. Thomas, and Michael Virgato. Improved Treatment of Dark Matter Capture in Neutron Stars III: Nucleon and Exotic Targets. 8 2021.

[106] Nicole F. Bell, Giorgio Busoni, Theo F. Motta, Sandra Robles, Anthony W. Thomas, and Michael Virgato. Nucleon Structure and Strong Interactions in Dark Matter Capture in Neutron Stars. 12 2020.

[107] Basudeb Dasgupta, Aritra Gupta, and Anupam Ray. Dark matter capture in celestial objects: light mediators, self-interactions, and complementarity with direct detection. *Journal of Cosmology and Astroparticle Physics*, 10:023, 6 2020.

[108] Raghuveer Garani, Yoann Genolini, and Thomas Hambye. New Analysis of Neutron Star Constraints on Asymmetric Dark Matter. *Journal of Cosmology and Astroparticle Physics*, 1905(05):035, 2019.

[109] Aniket Joglekar, Nirmal Raj, Philip Tanedo, and Hai-Bo Yu. Dark kinetic heating of neutron stars from contact interactions with relativistic targets. *Phys. Rev. D*, 102(12):123002, 2020.

[110] Aniket Joglekar, Nirmal Raj, Philip Tanedo, and Hai-Bo Yu. Relativistic capture of dark matter by electrons in neutron stars. *Phys. Lett.*, B:135767, 2020.

[111] Koichi Hamaguchi, Natsumi Nagata, and Keisuke Yanagi. Dark Matter Heating vs. Rotochemical Heating in Old Neutron Stars. *Phys. Lett.*, B795:484–489, 2019.

[112] Tarak Nath Maity and Farinaldo S Queiroz. Detecting bosonic dark matter with neutron stars. 2021.

[113] Nicole F. Bell, Giorgio Busoni, Sandra Robles, and Michael Virgato. Improved Treatment of Dark Matter Capture in Neutron Stars II: Leptonic Targets. *Journal of Cosmology and Astroparticle Physics*, 03:086, 2021.

[114] Joseph Bramante, Bradley J. Kavanagh, and Nirmal Raj. Scattering Searches for Dark Matter in Subhalos: Neutron Stars, Cosmic Rays, and Old Rocks. *Phys. Rev. Lett.*, 128(23):231801, 2022.

[115] Emanuele Berti et al. Dark Matter In Extreme Astrophysical Environments. In *2022 Snowmass Summer Study*, 3 2022.

[116] Gianfranco Bertone and Malcolm Fairbairn. Compact Stars as Dark Matter Probes. *Phys. Rev.*, D77:043515, 2008.

[117] Chris Kouvaris. WIMP Annihilation and Cooling of Neutron Stars. *Phys. Rev.*, D77(2):023006, January 2008.

[118] Chris Kouvaris and Peter Tinyakov. Excluding Light Asymmetric Bosonic Dark Matter. *Phys. Rev. Lett.*, 107:091301, 2011.

[119] Samuel D. McDermott, Hai-Bo Yu, and Kathryn M. Zurek. Constraints on Scalar Asymmetric Dark Matter from Black Hole Formation in Neutron Stars. *Phys. Rev.*, D85:023519, 2012.

[120] Joseph Bramante, Keita Fukushima, and Jason Kumar. Constraints on bosonic dark matter from observation of old neutron stars. *Phys. Rev.*, D87(5):055012, 2013.

[121] Kalliopi Petraki and Raymond R. Volkas. Review of asymmetric dark matter. *Int. J. Mod. Phys. A*, 28:1330028, 2013.

[122] Joseph Bramante, Keita Fukushima, Jason Kumar, and Elan Stopnitzky. Bounds on self-interacting fermion dark matter from observations of old neutron stars. *Phys. Rev.*, D89(1):015010, 2014.

[123] Bridget Bertoni, Ann E. Nelson, and Sanjay Reddy. Dark Matter Thermalization in Neutron Stars. *Phys. Rev.*, D88:123505, 2013.

[124] Martin Autzen and Chris Kouvaris. Blocking the Hawking Radiation. *Phys. Rev. D*, 89(12):123519, 2014.

[125] Joseph Bramante. Dark matter ignition of type Ia supernovae. *Phys. Rev. Lett.*, 115(14):141301, 2015.

[126] Joseph Bramante and Fatemeh Elahi. Higgs portals to pulsar collapse. *Phys. Rev.*, D91(11):115001, 2015.

[127] Javier F. Acevedo and Joseph Bramante. Supernovae Sparked By Dark Matter in White Dwarfs. *Phys. Rev. D*, 100(4):043020, 2019.

[128] Basudeb Dasgupta, Ranjan Laha, and Anupam Ray. Low Mass Black Holes from Dark Core Collapse. *Phys. Rev. Lett.*, 126(14):141105, 9 2021.

[129] Javier F. Acevedo, Joseph Bramante, Alan Goodman, Joachim Kopp, and Toby Opferkuch. Dark Matter, Destroyer of Worlds: Neutrino, Thermal, and Existential Signatures from Black Holes in the Sun and Earth. *Journal of Cosmology and Astroparticle Physics*, 04:026, 2021.

[130] Raghuveer Garani, Dmitry Levkov, and Peter Tinyakov. Solar mass black holes from neutron stars and bosonic dark matter. *Phys. Rev. D*, 105(6):063019, 2022.

[131] Nicole F. Bell, Giorgio Busoni, and Sandra Robles. Heating up Neutron Stars with Inelastic Dark Matter. *Journal of Cosmology and Astroparticle Physics*, 1809(09):018, 2018.

[132] Gerardo Alvarez, Aniket Joglekar, Mehrdad Phoroutan-Mehr, and Hai-Bo Yu. Heating Neutron Stars with Inelastic Dark Matter and Relativistic Targets. *Phys. Rev. D*, 107(10):103024, 1 2023.

[133] Brian Batell, Maxim Pospelov, and Adam Ritz. Direct Detection of Multi-component Secluded WIMPs. *Phys. Rev. D*, 79:115019, 2009.

[134] Rebecca K. Leane, Tim Linden, Payel Mukhopadhyay, and Natalia Toro. Celestial-Body Focused Dark Matter Annihilation Throughout the Galaxy. *Phys. Rev. D*, 103(7):075030, April 2021.

[135] Javier F. Acevedo, Rebecca K. Leane, and Lillian Santos-Olmsted. Milky Way White Dwarfs as Sub-GeV to Multi-TeV Dark Matter Detectors. 9 2023.

[136] Debajit Bose, Tarak Nath Maity, and Tirtha Sankar Ray. Neutrinos from captured dark matter annihilation in a galactic population of neutron stars. *Journal of Cosmology and Astroparticle Physics*, 05(05):001, May 2022.

[137] Thong T. Q. Nguyen and Tim M. P. Tait. Bounds on long-lived dark matter mediators from neutron stars. *Phys. Rev. D*, 107(11):115016, 12 2023.

[138] Tim Linden, Thong T. Q. Nguyen, and Tim M. P. Tait. Indirect Searches for Dark Photon-Photon Tridents in Celestial Objects. 2 2024.

[139] Motoko Fujiwara, Koichi Hamaguchi, Natsumi Nagata, and Maura E. Ramirez-Quezada. Vortex Creep Heating in Neutron Stars. 8 2023.

[140] Nirmal Raj, Prajwal Shivanna, and Gaurav Niraj Rachh. Exploring reheated sub-40000 Kelvin neutron stars with JWST, ELT, and TMT. *Phys. Rev. D*, 109(12):123040, 2024.

[141] Julio F. Navarro, Carlos S. Frenk, and Simon D. M. White. A Universal density profile from hierarchical clustering. *Astrophys. J.*, 490:493–508, 1997.

[142] Alister W. Graham, David Merritt, Ben Moore, Juerg Diemand, and Balsa Terzic. Empirical models for Dark Matter Halos. I. Nonparametric Construction of Density Profiles and Comparison with Parametric Models. *Astron. J.*, 132:2685–2700, 2006.

[143] Xiaowei Ou, Anna-Christina Eilers, Lina Necib, and Anna Frebel. The dark matter profile of the Milky Way inferred from its circular velocity curve. *MNRAS*, 528(1):693–710, February 2024.

[144] Miguel Pato, Fabio Iocco, and Gianfranco Bertone. Dynamical constraints on the dark matter distribution in the Milky Way. *Journal of Cosmology and Astroparticle Physics*, 12:001, 2015.

[145] Lidia Pieri, Julien Lavalle, Gianfranco Bertone, and Enzo Branchini. Implications of high-resolution simulations on indirect dark matter searches. *Physical Review D*, 83(2):023518, January 2011.

[146] A. J. Deason, V. Belokurov, N. W. Evans, and J. An. Broken degeneracies: the rotation curve and velocity anisotropy of the Milky Way halo. *Monthly Notices of the Royal Astronomical Society*, 424(1):L44–L48, July 2012.

[147] Xiaowei Ou, Anna-Christina Eilers, Lina Necib, and Anna Frebel. The dark matter profile of the Milky Way inferred from its circular velocity curve. *Monthly Notices of the Royal Astronomical Society*, 528(1):693–710, February 2024.

[148] Anna-Christina Eilers, David W. Hogg, Hans-Walter Rix, and Melissa K. Ness. The Circular Velocity Curve of the Milky Way from 5 to 25 kpc. *The Astrophysical Journal*, 871(1):120, January 2019.

[149] Clovis Hopman and Tal Alexander. The effect of mass-segregation on gravitational wave sources near massive black holes. *Astrophys. J. Lett.*, 645:L133–L136, 2006.

[150] A. Generozov, N. C. Stone, B. D. Metzger, and J. P. Ostriker. An overabundance of black hole X-ray binaries in the Galactic Centre from tidal captures. *Mon. Not. Roy. Astron. Soc.*, 478(3):4030–4051, 2018.

[151] Nicolas Chamel. Effective contact pairing forces from realistic calculations in infinite homogeneous nuclear matter. *Phys. Rev. C*, 82:014313, 2010.

[152] S. Goriely, N. Chamel, and J. M. Pearson. Further explorations of Skyrme-Hartree-Fock-Bogoliubov mass formulas. XII: Stiffness and stability of neutron-star matter. *Phys. Rev.*, C82:035804, 2010.

[153] A. Y. Potekhin, A. F. Fantina, N. Chamel, J. M. Pearson, and S. Goriely. Analytical representations of unified equations of state for neutron-star matter. *Astron. Astrophys.*, 560:A48, 2013.

[154] B. P. Abbott et al. GW170817: Measurements of neutron star radii and equation of state. *Phys. Rev. Lett.*, 121(16):161101, 2018.

[155] Elias R. Most, Lukas R. Weih, Luciano Rezzolla, and Jürgen Schaffner-Bielich. New constraints on radii and tidal deformabilities of neutron stars from GW170817. *Phys. Rev. Lett.*, 120(26):261103, 2018.

[156] Carolyn Raithel, Feryal Özel, and Dimitrios Psaltis. Tidal deformability from GW170817 as a direct probe of the neutron star radius. *Astrophys. J. Lett.*, 857(2):L23, 2018.

[157] M. C. Miller et al. PSR J0030+0451 Mass and Radius from $NICER$ Data and Implications for the Properties of Neutron Star Matter. *Astrophys. J. Lett.*, 887(1):L24, 2019.

[158] M. C. Miller et al. The Radius of PSR J0740+6620 from NICER and XMM-Newton Data. *Astrophys. J. Lett.*, 918(2):L28, 2021.

[159] Zhuo Chen, Tuan Do, Andrea M. Ghez, Matthew W. Hosek, Anja Feldmeier-Krause, Devin S. Chu, Rory O. Bentley, Jessica R. Lu, and Mark R. Morris.

The Star Formation History of the Milky Way's Nuclear Star Cluster. *The Astrophysical Journal*, 944(1):79, February 2023.

[160] Tal Alexander and Clovis Hopman. Strong mass segregation around a massive black hole. *Astrophys. J.*, 697:1861–1869, 2009.

[161] Fupeng Zhang and Pau Amaro Seoane. Monte-Carlo Stellar Dynamics near Massive Black Holes: Two-dimensional Fokker-Planck solutions of multiple mass components. 6 2023.

[162] R. Schödel, F. Nogueras-Lara, E. Gallego-Cano, B. Shahzamanian, A. T. Gallego-Calvente, and A. Gardini. The Milky Way's nuclear star cluster: Old, metal-rich, and cuspy. Structure and star formation history from deep imaging. *Astronomy & Astrophysics*, 641:A102, September 2020.

[163] Joshua P. Ridley and Duncan R. Lorimer. Isolated pulsar spin evolution on the P-Pdot Diagram. *Mon. Not. Roy. Astron. Soc.*, 404:1081, 2010.

[164] Sam Bates, Duncan Lorimer, Akshaya Rane, and Joe Swiggum. PsrPopPy: An open-source package for pulsar population simulations. *Mon. Not. Roy. Astron. Soc.*, 439(3):2893–2902, 2014.

[165] Duncan R. Lorimer. Binary and Millisecond Pulsars. *Living Reviews in Relativity*, 11(1):8, December 2008.

[166] Daryl Haggard, Craig Heinke, Dan Hooper, and Tim Linden. Low mass X-ray binaries in the Inner Galaxy: implications for millisecond pulsars and the GeV excess. *Journal of Cosmology and Astroparticle Physics*, 2017(5):056, May 2017.

[167] Joseph Bramante, Antonio Delgado, and Adam Martin. Multiscatter stellar capture of dark matter. *Phys. Rev.*, D96(6):063002, 2017.

[168] Javier F. Acevedo, Joseph Bramante, Rebecca K. Leane, and Nirmal Raj. Warming Nuclear Pasta with Dark Matter: Kinetic and Annihilation Heating of Neutron Star Crusts. *Journal of Cosmology and Astroparticle Physics*, 03:038, 2020.

[169] Rebecca K. Leane and Juri Smirnov. Dark Matter Capture in Celestial Objects: Treatment Across Kinematic and Interaction Regimes. 9 2023.

[170] Christian W. Bauer, Nicholas L. Rodd, and Bryan R. Webber. Dark matter spectra from the electroweak to the Planck scale. *JHEP*, 06:121, 2021.

[171] M. G. Aartsen et al. IceCube-Gen2: the window to the extreme Universe. *J. Phys. G*, 48(6):060501, 2021.

[172] A. D. Avrorin et al. Baikal-GVD: status and prospects. *EPJ Web Conf.*, 191:01006, 2018.

[173] S. Adrian-Martinez et al. Letter of intent for KM3NeT 2.0. *J. Phys. G*, 43(8):084001, 2016.

[174] Matteo Agostini et al. The Pacific Ocean Neutrino Experiment. *Nature Astron.*, 4(10):913–915, 2020.

[175] Z. P. Ye et al. Proposal for a neutrino telescope in South China Sea. 7 2022.

[176] Tian-Qi Huang, Zhen Cao, Mingjun Chen, Jiali Liu, Zike Wang, Xiaohao You, and Ying Qi. Proposal for the High Energy Neutrino Telescope. *PoS*, ICRC2023:1080, 2023.

[177] R. Abbasi et al. IceCube Data for Neutrino Point-Source Searches Years 2008-2018. 1 2021.

[178] Lisa Johanna Schumacher, Matthias Huber, Matteo Agostini, Mauricio Bustamante, Foteini Oikonomou, and Elisa Resconi. PLEνM: A global and distributed monitoring system of high-energy astrophysical neutrinos. *PoS*, ICRC2021:1185, 2021.

[179] Marco Chianese, Damiano F. G. Fiorillo, Rasmi Hajjar, Gennaro Miele, Stefano Morisi, and Ninetta Saviano. Heavy decaying dark matter at future neutrino radio telescopes. *Journal of Cosmology and Astroparticle Physics*, 05:074, 2021.

[180] H. Abdalla et al. The H.E.S.S. Galactic plane survey. *Astron. Astrophys.*, 612:A1, 2018.

[181] Mceq. `https://github.com/mceq-project/MCEq`.

[182] Felix Riehn, Hans P. Dembinski, Ralph Engel, Anatoli Fedynitch, Thomas K. Gaisser, and Todor Stanev. The hadronic interaction model SIBYLL 2.3c and Feynman scaling. *PoS*, ICRC2017:301, 2018.

[183] JM Picone, AE Hedin, D Pj Drob, and AC Aikin. Nrlmsise-00 empirical model of the atmosphere: Statistical comparisons and scientific issues. *Journal of Geophysical Research: Space Physics*, 107(A12):SIA–15, 2002.

[184] R. Abbasi et al. Improved Characterization of the Astrophysical Muon–neutrino Flux with 9.5 Years of IceCube Data. *Astrophys. J.*, 928(1):50, 2022.

[185] M. G. Aartsen et al. Time-Integrated Neutrino Source Searches with 10 Years of IceCube Data. *Phys. Rev. Lett.*, 124(5):051103, 2020.

[186] V. S. Berezinsky and G. T. Zatsepin. Cosmic rays at ultrahigh-energies (neutrino?). *Phys. Lett. B*, 28:423–424, 1969.

[187] Jonas Heinze, Anatoli Fedynitch, Denise Boncioli, and Walter Winter. A new view on Auger data and cosmogenic neutrinos in light of different nuclear disintegration and air-shower models. *Astrophys. J.*, 873(1):88, 2019.

[188] P. Allison et al. Measurement of the real dielectric permittivity ϵ_r of glacial ice. *Astropart. Phys.*, 108:63–73, 2019.

[189] Ke Fang and Kohta Murase. Multimessenger Implications of Sub-PeV Diffuse Galactic Gamma-Ray Emission. *Astrophys. J.*, 919(2):93, 2021.

[190] G. Maier, L. Arrabito, K. Bernlöhr, J. Bregeon, P. Cumani, T. Hassan, J. Hinton, and A. Moralejo. Performance of the Cherenkov Telescope Array. *PoS*, ICRC2019:733, 2020.

[191] A. Albert et al. Science Case for a Wide Field-of-View Very-High-Energy Gamma-Ray Observatory in the Southern Hemisphere. 2 2019.

[192] Douglas P. Finkbeiner and Neal Weiner. Exciting dark matter and the INTEGRAL/SPI 511keV signal. *Physical Review D*, 76(8):083519, October 2007.

[193] Douglas P. Finkbeiner, Tracy R. Slatyer, Neal Weiner, and Itay Yavin. PAMELA, DAMA, INTEGRAL and signatures of metastable excited WIMPs. *Journal of Cosmology and Astroparticle Physics*, 2009(9):037, September 2009.

[194] Maxim Pospelov and Adam Ritz. The galactic 511 keV line from electroweak scale WIMPs. *Physics Letters B*, 651(2-3):208–215, July 2007.

[195] Yue Zhang. Self-interacting dark matter without direct detection constraints. *Physics of the Dark Universe*, 15:82–89, March 2017.

[196] Mattias Blennow, Stefan Clementz, and Juan Herrero-Garcia. Self-interacting inelastic dark matter: a viable solution to the small scale structure problems. *Journal of Cosmology and Astroparticle Physics*, 2017(3):048, March 2017.

[197] Gerardo Alvarez and Hai-Bo Yu. Astrophysical probes of inelastic dark matter with a light mediator. 2019.

[198] J. M. Lattimer and M. Prakash. The Physics of Neutron Stars. *Science*, 304(5670):536–542, April 2004.

[199] J. P. Lees et al. Search for a Dark Photon in e^+e^- Collisions at BaBar. *Phys. Rev. Lett.*, 113(20):201801, 2014.

[200] Roel Aaij et al. Search for $A' \to \mu^+\mu^-$ Decays. *Phys. Rev. Lett.*, 124(4):041801, 2020.

[201] Albert M Sirunyan et al. Search for a Narrow Resonance Lighter than 200 GeV Decaying to a Pair of Muons in Proton-Proton Collisions at $\sqrt{s} =$ TeV. *Phys. Rev. Lett.*, 124(13):131802, 2020.

[202] Marco Fabbrichesi, Emidio Gabrielli, and Gaia Lanfranchi. The Dark Photon. 5 2020.

[203] L.D. Landau. *The Classical Theory of Fields*. Course of theoretical physics. Elsevier Science, 2013.

[204] Joonas Nättilä and Jari J. E. Kajava. Fundamental physics with neutron stars. 11 2022.

[205] Lijing Shao and Kent Yagi. Neutron stars as extreme laboratories for gravity tests. *Sci. Bull.*, 67:1946–1949, 2022.

[206] J. M. Lattimer and M. Prakash. Neutron star structure and the equation of state. *Astrophys. J.*, 550:426, 2001.

[207] N. Tetzlaff, R. Neuhäuser, M. M. Hohle, and G. Maciejewski. Identifying birth places of young isolated neutron stars. *MNRAS*, 402(4):2369–2387, March 2010.

[208] Dima G. Yakovlev and C. J. Pethick. Neutron star cooling. *Ann. Rev. Astron. Astrophys.*, 42:169–210, 2004.

[209] Dany Page, James M. Lattimer, Madappa Prakash, and Andrew W. Steiner. Minimal cooling of neutron stars: A New paradigm. *Astrophys. J. Suppl.*, 155:623–650, 2004.

[210] A. Y. Potekhin, D. A. Zyuzin, D. G. Yakovlev, M. V. Beznogov, and Yu. A. Shibanov. Thermal luminosities of cooling neutron stars. *Mon. Not. Roy. Astron. Soc.*, 496(4):5052–5071, 2020.

[211] D. Gonzalez and A. Reisenegger. Internal heating of old neutron stars: contrasting different mechanisms. *AAP*, 522:A16, November 2010.

[212] D. R. Lorimer. Radio pulsar populations. *Astrophys. Space Sci. Proc.*, pages 21–36, 2011.

[213] F. M. Walter, T. Eisenbeiss, J. M. Lattimer, B. Kim, V. Hambaryan, and R. Neuhaeuser. Revisiting the Parallax of the Isolated Neutron Star RX J185635-3754 Using HST/ACS Imaging. *Astrophys. J.*, 724:669–677, 2010.

[214] Ling-Lin Zheng, Mouyuan Sun, Wei-Min Gu, Tuan Yi, Zhi-Xiang Zhang, Pei Wang, Junfeng Wang, Jianfeng Wu, Song Wang, Jia Zhang, Chun-Qian Li, Jian-Rong Shi, Yong Shao, Xiang-Dong Li, Jin-Bo Fu, Fan Yang, Zhongrui Bai, Yu Bai, Haotong Zhang, and Jifeng Liu. The Nearest Neutron Star Candidate in a Binary Revealed by Optical Time-domain Surveys. *arXiv e-prints*, page arXiv:2210.04685, October 2022.

[215] Omer Blaes and Piero Madau. Can We Observe Accreting, Isolated Neutron Stars? *The Astrophysical Journal*, 403:690, February 1993.

[216] Ryan S. Lynch, Joseph K. Swiggum, Vlad I. Kondratiev, David L. Kaplan, Kevin Stovall, Emmanuel Fonseca, Mallory S. E. Roberts, Lina Levin, Megan E. DeCesar, Bingyi Cui, S. Bradley Cenko, Pradip Gatkine, Anne M. Archibald, Shawn Banaszak, Christopher M. Biwer, Jason Boyles, Pragya Chawla, Louis P. Dartez, David Day, Anthony J. Ford, Joseph Flanigan, Jason W. T. Hessels, Jesus Hinojosa, Fredrick A. Jenet, Chen Karako-Argaman, Victoria M. Kaspi, Sean Leake, Grady Lunsford, José G. Martinez, Alberto Mata, Maura A. McLaughlin, Hind Al Noori, Scott M. Ransom, Matthew D. Rohr, Xavier

Siemens, Renée Spiewak, Ingrid H. Stairs, Joeri van Leeuwen, Arielle N. Walker, and Bradley L. Wells. The Green Bank North Celestial Cap Pulsar Survey. III. 45 New Pulsar Timing Solutions. *The Astrophysical Journal*, 859(2):93, June 2018.

[217] K. Stovall, R. S. Lynch, S. M. Ransom, A. M. Archibald, S. Banaszak, C. M. Biwer, J. Boyles, L. P. Dartez, D. Day, A. J. Ford, J. Flanigan, A. Garcia, J. W. T. Hessels, J. Hinojosa, F. A. Jenet, D. L. Kaplan, C. Karako-Argaman, V. M. Kaspi, V. I. Kondratiev, S. Leake, D. R. Lorimer, G. Lunsford, J. G. Martinez, A. Mata, M. A. McLaughlin, M. S. E. Roberts, M. D. Rohr, X. Siemens, I. H. Stairs, J. van Leeuwen, A. N. Walker, and B. L. Wells. The Green Bank Northern Celestial Cap Pulsar Survey. I. Survey Description, Data Analysis, and Initial Results. *APJ*, 791(1):67, August 2014.

[218] G. Y. Agazie, M. G. Mingyar, M. A. McLaughlin, J. K. Swiggum, D. L. Kaplan, H. Blumer, P. Chawla, M. DeCesar, P. B. Demorest, W. Fiore, E. Fonseca, J. D. Gelfand, V. M. Kaspi, V. I. Kondratiev, M. LaRose, J. van Leeuwen, L. Levin, E. F. Lewis, R. S. Lynch, A. E. McEwen, H. Al Noori, E. Parent, S. M. Ransom, M. S. E. Roberts, A. Schmiedekamp, C. Schmiedekamp, X. Siemens, R. Spiewak, I. H. Stairs, and M. Surnis. The Green Bank Northern Celestial Cap Pulsar Survey. VI. Discovery and Timing of PSR J1759+5036: A Double Neutron Star Binary Pulsar. *The Astrophysical Journal*, 922(1):35, November 2021.

[219] A. E. McEwen, R. Spiewak, J. K. Swiggum, D. L. Kaplan, W. Fiore, G. Y. Agazie, H. Blumer, P. Chawla, M. DeCesar, V. M. Kaspi, V. I. Kondratiev,

M. LaRose, L. Levin, R. S. Lynch, M. McLaughlin, M. Mingyar, H. Al Noori, S. M. Ransom, M. S. E. Roberts, A. Schmiedekamp, C. Schmiedekamp, X. Siemens, I. Stairs, K. Stovall, M. Surnis, and J. van Leeuwen. The Green Bank North Celestial Cap Pulsar Survey. V. Pulsar Census and Survey Sensitivity. *The Astrophysical Journal*, 892(2):76, April 2020.

[220] R. J. Aloisi, A. Cruz, L. Daniels, N. Meyers, R. Roekle, A. Schuett, J. K. Swiggum, M. E. DeCesar, D. L. Kaplan, R. S. Lynch, K. Stovall, Lina Levin, A. M. Archibald, S. Banaszak, C. M. Biwer, J. Boyles, P. Chawla, L. P. Dartez, B. Cui, D. F. Day, A. J. Ford, J. Flanigan, E. Fonseca, J. W. T. Hessels, J. Hinojosa, C. Karako-Argaman, V. M. Kaspi, V. I. Kondratiev, S. Leake, G. Lunsford, J. G. Martinez, A. Mata, M. A. McLaughlin, H. Al Noori, S. M. Ransom, M. S. E. Roberts, M. D. Rohr, X. Siemens, R. Spiewak, I. H. Stairs, J. van Leeuwen, A. N. Walker, and B. L. Wells. The Green Bank North Celestial Cap Pulsar Survey. IV. Four New Timing Solutions. *The Astrophysical Journal*, 875(1):19, April 2019.

[221] A. M. Kawash, M. A. McLaughlin, D. L. Kaplan, M. E. DeCesar, L. Levin, D. R. Lorimer, R. S. Lynch, K. Stovall, J. K. Swiggum, E. Fonseca, A. M. Archibald, S. Banaszak, C. M. Biwer, J. Boyles, B. Cui, L. P. Dartez, D. Day, S. Ernst, A. J. Ford, J. Flanigan, S. A. Heatherly, J. W. T. Hessels, J. Hinojosa, F. A. Jenet, C. Karako-Argaman, V. M. Kaspi, V. I. Kondratiev, S. Leake, G. Lunsford, J. G. Martinez, A. Mata, T. D. Matheny, A. E. Mcewen, M. G. Mingyar, A. L. Orsini, S. M. Ransom, M. S. E. Roberts, M. D. Rohr, X. Siemens, R. Spiewak, I. H. Stairs, J. van Leeuwen, A. N. Walker, and B. L. Wells. The Green Bank

Northern Celestial Cap Pulsar Survey. II. The Discovery and Timing of 10 Pulsars. *The Astrophysical Journal*, 857(2):131, April 2018.

[222] D. R. Lorimer, N. D'Amico, A. G. Lyne, J. H. Seiradakis, A. Athanasopoulos, F. Camilo, A. Jessner, M. Kramer, R. Wielebinski, and K. M. Xilouris. The European Pulsar Network Pulse Profile Database. In John D. Hadjidemetrioy and John H. Seiradakis, editors, *Joint European and National Astronomical Meeting*, page 236, January 1997.

[223] Sebastien Guillot, G. G. Pavlov, C. Reyes, A. Reisenegger, L. Rodriguez, B. Rangelov, and O. Kargaltsev. Hubble Space Telescope Nondetection of PSR J2144–3933: The Coldest Known Neutron Star. *Astrophys. J.*, 874(2):175, 2019.

[224] Miguel A. de Avillez, Gervásio J. Anela, Ashish Asgekar, Dieter Breitschwerdt, and Dominic H. F. M. Schnitzeler. Electrons in the supernova-driven interstellar medium. Results from self-consistent time-dependent ionic and hydrodynamic evolution of the interstellar plasma. *AAP*, 644:A156, December 2020.

[225] Allison M. Matthews et al. The NANOGrav Nine-year Data Set: Astrometric Measurements of 37 Millisecond Pulsars. *Astrophys. J.*, 818(1):92, 2016.

[226] D. J. Reardon et al. Timing analysis for 20 millisecond pulsars in the Parkes Pulsar Timing Array. *Mon. Not. Roy. Astron. Soc.*, 455(2):1751–1769, 2016.

[227] A. T. Deller et al. Microarcsecond VLBI Pulsar Astrometry with PSRπ II. Parallax Distances for 57 Pulsars. *Astrophys. J.*, 875(2):100, 2019.

[228] Adam Deller. Pulsar distance measurements with VLBI. In *40th COSPAR Scientific Assembly*, volume 40, pages E1.15–5–14, January 2014.

[229] B. Posselt, G. Spence, and G. G. Pavlov. A Chandra Search for the Pulsar Wind Nebula Around psr B1055–52. *Astrophys. J.*, 811(2):96, 2015.

[230] R. P. Mignani, G. G. Pavlov, and O. Kargaltsev. Optical-Ultraviolet Spectrum and Proper Motion of the Middle-aged Pulsar B1055-52. *The Astrophysical Journal*, 720(2):1635–1643, September 2010.

[231] FAST-GPPS pulsar catalogue. `http://zmtt.bao.ac.cn/GPPS/GPPSnewPSR.html`.

[232] W. Q. Su et al. The FAST Galactic Plane Pulsar Snapshot Survey – III. Timing results of 30 newly discovered pulsars. *Mon. Not. Roy. Astron. Soc.*, 526(2):2645–2656, 2023.

[233] J. L. Han et al. The FAST Galactic Plane Pulsar Snapshot survey: I. Project design and pulsar discoveries. *Res. Astron. Astrophys.*, 21:107, 2021.

[234] Rendong Nan, Di Li, Chengjin Jin, Qiming Wang, Lichun Zhu, Wenbai Zhu, Haiyan Zhang, Youling Yue, and Lei Qian. The Five-Hundred-Meter Aperture Spherical Radio Telescope (FAST) Project. *Int. J. Mod. Phys.*, D20:989–1024, 2011.

[235] CHIME pulsar catalogue. `https://www.chime-frb.ca/galactic`.

[236] Motoko Fujiwara, Koichi Hamaguchi, Natsumi Nagata, and Jiaming Zheng. Capture of Electroweak Multiplet Dark Matter in Neutron Stars. 4 2022.

[237] Thomas E. Lutz and Douglas H. Kelker. On the Use of Trigonometric Parallaxes for the Calibration of Luminosity Systems: Theory. *Publications of the Astronomical Society of the Pacific*, 85(507):573, October 1973.

[238] A. Vahdat, B. Posselt, A. Santangelo, and G. G. Pavlov. Toward an X-ray inventory of nearby neutron stars. *AAP*, 658:A95, February 2022.

[239] Oleg Kargaltsev, Martin Durant, George G. Pavlov, and Gordon Garmire. Chandra Pulsar Survey (ChaPS). *The Astrophysical Journal Supplement*, 201(2):37, August 2012.

[240] Rodrigo Fernandez and Andreas Reisenegger. Rotochemical heating in millisecond pulsars. Formalism and non-superfluid case. *Astrophys. J.*, 625:291–306, 2005.

[241] Andreas Reisenegger, Paula Jofre, Rodrigo Fernandez, and Elena Kantor. Rotochemical Heating of Neutron Stars: Rigorous Formalism with Electrostatic Potential Perturbations. *Astrophys. J.*, 653:568–572, 2006.

[242] Cristobal Petrovich and Andreas Reisenegger. Rotochemical heating in millisecond pulsars: modified Urca reactions with uniform Cooper pairing gaps. *Astron. Astrophys.*, 521:A77, 2010.

[243] Nicolás González-Jiménez, Cristobal Petrovich, and Andreas Reisenegger. Rotochemical heating of millisecond and classical pulsars with anisotropic and density-dependent superfluid gap models. *Mon. Not. Roy. Astron. Soc.*, 447:2073, 2015.

[244] E. M. Kantor and M. E. Gusakov. Long-lasting accretion-powered chemical heating of millisecond pulsars. *MNRAS*, 508(4):6118–6127, December 2021.

[245] M. E. Gusakov, E. M. Kantor, and A. Reisenegger. Rotation-induced deep crustal heating of millisecond pulsars. *MNRAS*, 453(1):L36–L40, October 2015.

[246] P. W. Anderson and N. Itoh. Pulsar glitches and restlessness as a hard superfluidity phenomenon. *Nature*, 256:25–27, 1975.

[247] M. A. Alpar, D. Pines, P. W. Anderson, and J. Shaham. Vortex creep and the internal temperature of neutron stars. I - General theory. *APJ*, 276:325–334, January 1984.

[248] Noriaki Shibazaki and Frederick K. Lamb. Neutron Star Evolution with Internal Heating. *APJ*, 346:808, November 1989.

[249] Hideyuki Umeda, Noriaki Shibazaki, Ken'ichi Nomoto, and Sachiko Tsuruta. Thermal Evolution of Neutron Stars with Internal Frictional Heating. *APJ*, 408:186, May 1993.

[250] K. Van Riper, B. Link, and R. Epstein. Frictional heating and neutron star thermal evolution. *Astrophys. J.*, 448:294, 1995.

[251] Michelle B. Larson and Bennett Link. Superfluid friction and late-time thermal evolution of neutron stars. *Astrophys. J.*, 521:271, 1999.

[252] Peter Goldreich and Andreas Reisenegger. Magnetic Field Decay in Isolated Neutron Stars. *apj*, 395:250, August 1992.

[253] G. Baym and D. Pines. Neutron starquakes and pulsar speedup. *Annals of Physics*, 66:816–835, January 1971.

[254] Daniel Carney et al. Snowmass2021 cosmic frontier white paper: Ultraheavy particle dark matter. *SciPost Phys. Core*, 6:075, 2023.

[255] Wai-Yee Keung, Danny Marfatia, and Po-Yan Tseng. Heating neutron stars with GeV dark matter. *JHEP*, 07:181, 2020.

[256] Koichi Hamaguchi, Natsumi Nagata, and Maura E. Ramirez-Quezada. Neutron Star Heating in Dark Matter Models for the Muon $g-2$ Discrepancy. 4 2022.

[257] John Coffey, David McKeen, David E. Morrissey, and Nirmal Raj. Neutron star observations of pseudoscalar-mediated dark matter. *Phys. Rev. D*, 106(11):115019, 2022.

[258] Motoko Fujiwara, Koichi Hamaguchi, Natsumi Nagata, and Maura E. Ramirez-Quezada. Vortex Creep Heating vs. Dark Matter Heating in Neutron Stars. *Phys. Lett.*, 848:138341, 2024.

[259] Mingjie Jin and Yu Gao. Nucleon - Light Dark Matter Annihilation through Baryon Number Violation. *Phys. Rev. D*, 98(7):075026, 2018.

[260] A. Herrero, M. A. Pérez-García, J. Silk, and C. Albertus. Dark matter and bubble nucleation in old neutron stars. *Phys. Rev. D*, 100(10):103019, 2019.

[261] Yang Bai, Joshua Berger, Mrunal Korwar, and Nicholas Orlofsky. Phenomenology of magnetic black holes with electroweak-symmetric coronas. *JHEP*, 10:210, 2020.

[262] Moira I. Gresham, Vincent S. H. Lee, and Kathryn M. Zurek. Astrophysical observations of a dark matter-Baryon fifth force. *Journal of Cosmology and Astroparticle Physics*, 02:048, 2023.

[263] David McKeen, Maxim Pospelov, and Nirmal Raj. Cosmological and astrophysical probes of dark baryons. *Phys. Rev. D*, 103(11):115002, 2021.

[264] David McKeen, Maxim Pospelov, and Nirmal Raj. Neutron Star Internal Heating Constraints on Mirror Matter. *Phys. Rev. Lett.*, 127(6):061805, 2021.

[265] Itzhak Goldman, Rabindra N. Mohapatra, Shmuel Nussinov, and Yongchao Zhang. Constraints on neutron–mirror-neutron oscillation from neutron star cooling. *Eur. Phys. J. C*, 82(10):945, 2022.

[266] Itzhak Goldman, Rabindra N. Mohapatra, Shmuel Nussinov, and Yongchao Zhang. Neutron-Mirror-Neutron Oscillation and Neutron Star Cooling. *Phys. Rev. Lett.*, 129(6):061103, 2022.

[267] Zurab Berezhiani, Riccardo Biondi, Massimo Mannarelli, and Francesco Tonelli. Neutron-mirror neutron mixing and neutron stars. *Eur. Phys. J. C*, 81(11):1036, 2021.

[268] Hooman Davoudiasl. Stellar signals of a baryon-number-violating long-range force. *Phys. Rev. D*, 108(1):015023, 2023.

[269] Yohei Ema, Robert McGehee, Maxim Pospelov, and Anupam Ray. Dark Matter Catalyzed Baryon Destruction. 5 2024.

[270] Raghuveer Garani, Aritra Gupta, and Nirmal Raj. Observing the thermalization of dark matter in neutron stars. *Phys. Rev. D*, 103(4):043019, 2021.

[271] Veniamin Berezinsky, Vyacheslav Dokuchaev, and Yury Eroshenko. Remnants of dark matter clumps. *Phys. Rev. D*, 77:083519, 2008.

[272] G. D. Illingworth et al. The *HST* eXtreme Deep Field (XDF): Combining All ACS and WFC3/IR Data on the HUDF Region into the Deepest Field Ever. *Astrophys. J. Suppl.*, 209:6, 2013.

[273] M. Ángeles Pérez-García and Joseph Silk. Constraining decaying dark matter with neutron stars. *Phys. Lett.*, B744:13–17, 2015.

[274] Jason Dexter and Ryan M. O'Leary. The Peculiar Pulsar Population of the Central Parsec. *Astrophys. J. Lett.*, 783:L7, 2014.

[275] Monica Colpi, Stuart L. Shapiro, and Ira Wasserman. Boson stars: Gravitational equilibria of self-interacting scalar fields. *Physical Review Letters*, 57(20):2485–2488, November 1986.

[276] Gary A. Mamon and Ewa L. Lokas. Dark matter in elliptical galaxies. 1. Is the total mass density profile of the NFW form or even steeper? *Mon. Not. Roy. Astron. Soc.*, 362:95–109, 2005. [Erratum: Mon.Not.Roy.Astron.Soc. 370, 1581–1584 (2006)].

[277] Pavel Kroupa. On the variation of the initial mass function. *Monthly Notices of the Royal Astronomical Society*, 322(2):231–246, April 2001.

[278] Andrew M. Hopkins and John F. Beacom. On the Normalization of the Cosmic Star Formation History. *The Astrophysical Journal*, 651(1):142–154, November 2006.

[279] Myles Hollander and Douglas A. Wolfe. *Nonparametric Statistical Methods*. Wiley, second edition, 1999.